Design and Performance of a Compact High-Energy Computed Tomography System for the Study of Metal Solidification

by

Imad Maurice Jureidini

B.S., Applied Physics, Columbia University, 1994
S.M., Nuclear Engineering, Massachusetts Institute of Technology, 1997

SUBMITTED TO THE DEPARTMENT OF NUCLEAR ENGINEERING IN PARTIAL FULFILLMENT OF THE REQUIREMENTS FOR THE DEGREE OF

DOCTOR OF PHILOSOPHY IN NUCLEAR ENGINEERING

AT THE

MASSACHUSETTS INSTITUTE OF TECHNOLOGY

September 1998

Signature of Author: _____
Department of Nuclear Engineering
August 27, 1998

Certified by: _____
Richard Lanza
Senior Research Scientist, Nuclear Engineering Department
Thesis Supervisor

Certified by: _____
Lawrence Lidsky
Professor of Nuclear Engineering
Thesis Reader

Accepted by: _____
Lawrence Lidsky
Professor of Nuclear Engineering
Chairman, Department Committee on Graduate Students

Design and Performance of a Compact High-Energy Computed Tomography System for the Study of Metal Solidification

by

Imad Maurice Jureidini

Submitted to the Department of Nuclear Engineering
on August 27, 1998 in Partial Fulfillment of the Requirements for the Degree of
Doctor of Philosophy in Nuclear Engineering

ABSTRACT

The aim of this work is to study the feasibility of a computed tomography (CT) sensor useful to the metal casting industry to improve product quality and productivity. X-ray CT allows the non-destructive measurement of the two-dimensional density distribution in a given plane through an object. The solid and liquid phases of aluminum differ in density by approximately 10%, allowing CT to discriminate the solidification front. A compact high-energy x-ray CT system was designed and built to observe the solidification front in an aluminum sample 15-cm in diameter.

X-rays photons were produced by a compact 6 MeV linear accelerator (linac) with an average energy of 1.3 MeV. The linac was pulsed at a rate of 180 Hz, with a 4 μs pulse duration. The photons were emitted from a 2-mm spot in a 32° fan-beam configuration. A 128-channel detector system, placed on an arc 84.5 cm away from the source, performed x-ray attenuation measurements. Channels consisted of 1.8 mm wide cadmium tungstate scintillation crystals coupled to photodiodes. Tungsten anti-scatter plates were used to reduce the influence of scattered photons on the signal. The imaged object was placed on a motion system in order to perform the 360° rotation necessary for tomographic reconstruction.

The system achieved a resolution of 1.6 mm with a slice thickness of 5 mm and a sensitivity of 1.5 %. Data acquisition time was 2 minutes, but was limited by the maximum speed of the rotary stage. The solidification front in a pure aluminum sample was successfully imaged.

A study of the feasibility of identifying the solidification front in a metal cast using measurements obtained by translation alone is presented. A model-based reconstruction algorithm was implemented assuming a rectangular liquid zone surrounded by a rectangular solid zone. A sample object's geometry was correctly reconstructed from experimental data, demonstrating promise for this technique. An analysis of its theoretical performance is presented in terms of the experimental parameters.

Thesis Advisor: Richard Lanza
Title: Senior Research Scientist

Acknowledgments

My gratitude goes toward my advisor, Dr. Richard Lanza, for his endless support, advice, and friendliness. I also extend my thanks to Prof. Jung-Hoon Chun and Dr. Nannaji Saka. It has been a pleasure and a privilege to work with them.

Of course, most of the real work was done by the graduate students, Mark Hytros and DongSik Kim. I will always keep fond memories of the many hours spent planning, building and using the CastScan facility with them.

The laboratory was built at the MIT Bates Linear Accelerator Center, where countless people worked hard to help us build and operate our facility. In particular, I would like to thank Ken Hatch, John Quattrochi, Dennis Boiden, Frank Masse and Chris Tschalaer. In addition, the folks at the Bates Physical Plant and at the machine shop were always available and helpful.

We received tremendous support from our hardware suppliers. I would like to thank the people at Schonberg Corporation for their prompt help when difficulties were encountered with the linac. Analogic Corporation was an equally valuable aide to our work. I would particularly like to thank Dr. John Dobbs who saved me months of agony by helping me understand how computed tomography works in the real world.

The success of this project has depended upon the support of many people, but few have contributed as much time, effort and enthusiasm as Rich Appel, without whom our data acquisition system would never have seen the light of day.

During the lifetime of this project, we enjoyed a friendly collaboration with Dr. Tim Roney, Dr. Dennis Kunerth and Dr. Tim White of the Idaho National Engineering and Environmental Laboratory.

Finally, I would like express my gratitude to Prof. Larry Lidsky for his advice and patience while reviewing my work and this thesis.

This work was in part funded by the National Science Foundation (Grant No. DMI-9522973), the Idaho National Engineering and Environmental Laboratory - University Research Consortium (Contract No. C95-175002-LKK-267-95), and the CastScan Consortium, which consisted of the Aluminum Company of America (ALCOA), Inland Steel Industries and the Reynolds Metals Company.

Table of Contents

List of Tables

List of Figures

1. INTRODUCTION

1.1. Motivation

This project's primary focus is the non-destructive monitoring of solidification in metals using the concepts of x-ray computed tomography (CT). The term *CastScan* was invented in reference to the process of scanning cast metals.

The aluminum and steel casting industries rely heavily on the process of continuous casting to produce raw metal. Figure 1.1 shows a typical industrial continuous caster.

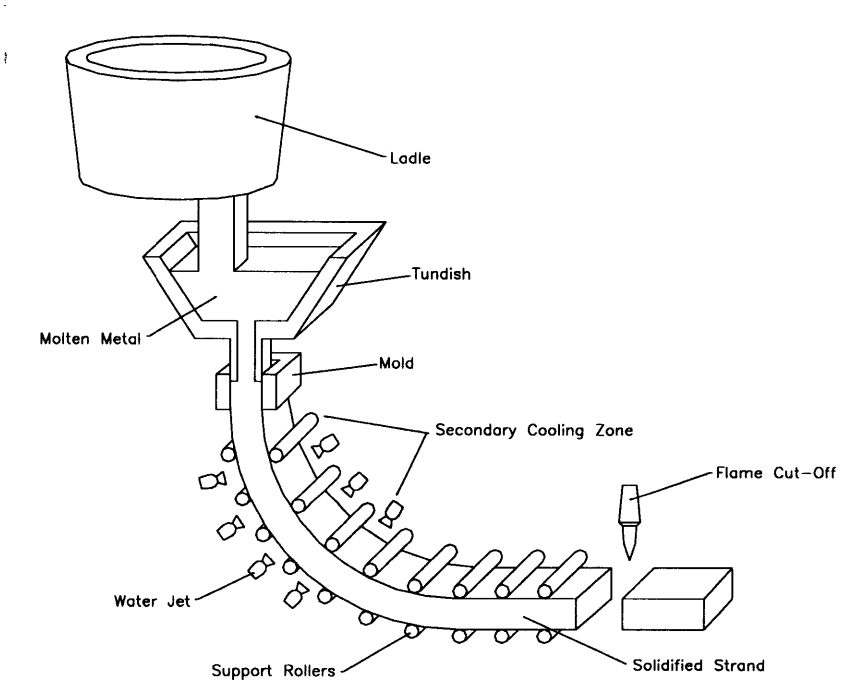

Figure 1.1. Schematic of a continuous casting facility.

Molten metal is poured from a tundish into a chilled mold. The outer surface of the metal freezes and contains the molten metal as it exits the mold. The metal is further cooled by water sprays until its entire cross-section is solidified, at which point it is cut. Monitoring

the solidification process is important for this industry because it could yield improved productivity and product quality. In addition, breakout accidents, during which the solidified "skin" ruptures and the contents of the tundish pour out, could be avoided.

A number of factors make computed tomography (CT) a potentially valuable tool to monitor this process. CT is a technique that yields cross-sectional density maps across an object. Because the density of the liquid and solid phases of a metal is usually different, CT can differentiate them. Table 1.1 shows the typical density contrast between two metals of interest, aluminum and steel.

	Solid Density [kg/m^3]	Liquid Density [kg/m^3]	Difference
Steel	~7800	~7400	4%-7%
Aluminum	~2700	~2400	9%-12%

Table 1.1. Solid and liquid densities of steel and aluminum.

As we will show, imaging large samples of aluminum or steel requires x-rays of energies greater than 1 MeV. Recent progress in linear accelerator technology has brought to market fairly inexpensive, simple to use and maintain, and compact x-ray sources with sufficient intensity to allow imaging of large metallic objects via CT. In addition, the rapidly rising computing power available today has freed CT from the realm of expensive supercomputers. Today's PC Compatible desktop computer is well suited for this application in the laboratory environment. The combination of these advances is opening new fields to an imaging modality until recently reserved to medical applications and large budgets.

In this section, we will review the concepts of computed tomography. We will also examine how high energy CT has been used in the past. Finally, we will present the goals of this experiment as well as the contributions it brings to this field of study.

1.2. Review of High Energy CT

Computed tomography allows one to obtain cross–sectional density images of objects by non-destructive means. We will first examine the fundamentals of CT in section 1.2.1. Because of the particularities of x-ray physics, we will show that CT is only feasible in a high-energy regime for this application. Finally, a review of the state of the art of high energy CT will be presented.

1.2.1. Basics of CT

For over a century, x-rays have played a crucial role in the field of medical imaging. Soon after their discovery by Roentgen, people used x-rays to examine the skeleton. Until the 70s, x-rays were used mainly for radiography, where a "shadow" of a person or object is projected onto photographic film. The layout of a radiography experiment is shown in Figure 1.2.

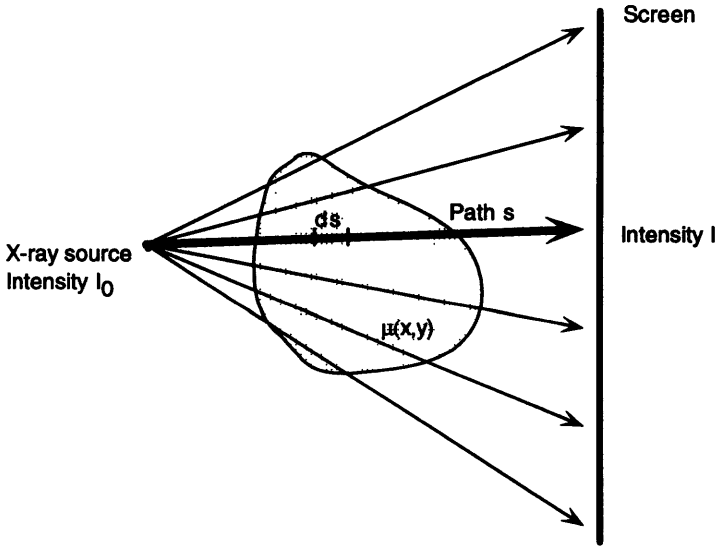

Figure 1.2. Schematic of a radiography experiment.

X-rays are photons of high energy, typically between 1 keV and up to several MeV. Unlike visible light, x-rays are very penetrating. The ability of a photon beam to penetrate an object

is described by a number called the linear attenuation coefficient μ. Photon attenuation obeys Beer's law, given in Eq. 1. I_0 is the source intensity; I is the intensity at the penetration depth x.

$$I(x) = I_0 e^{-\mu x} \qquad \text{Eq. 1}$$

The lower the value of μ is, the more penetrating the beam is. The linear attenuation coefficient is a function of the object's electron density, which in turn depends on the material's elemental composition and density. The coefficient is also a function of the photon energy. For a given material and for a given energy, μ is only proportional to density.

In a radiography experiment, one measures the integral of the linear attenuation coefficient between the source and the detector, which results in a loss of the depth information along the integration path. This is illustrated in Eq. 2.

$$I = I_0 e^{-\int_0^x \mu(s')ds'} \qquad \text{Eq. 2}$$

The principles of computed tomography were first laid out by Cormack [1] in 1963. The first practical implementation of x-ray CT is due to Hounsfield [2] in the early 1970s. Unlike radiography, CT provides depth information. A typical CT experiment setup is shown in Figure 1.3. CT gathers projection data in a similar way to radiography. However, it involves the additional step of acquiring the projections all around the object being studied. The experiment is described in the framework of the angle θ, representing the angle at which x-rays travel through the object, and z, representing the distance between the ray being considered and the center of rotation of the system. This situation is illustrated in Figure 1.4.

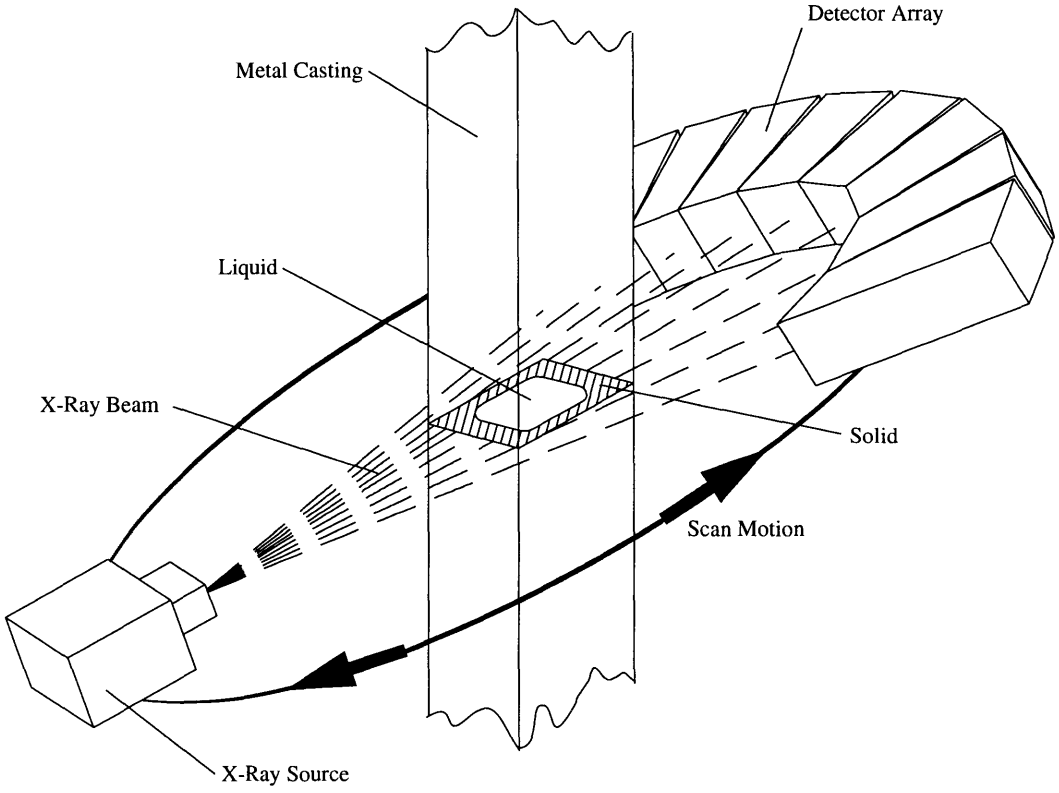

Figure 1.3. Schematic of a CT experiment.

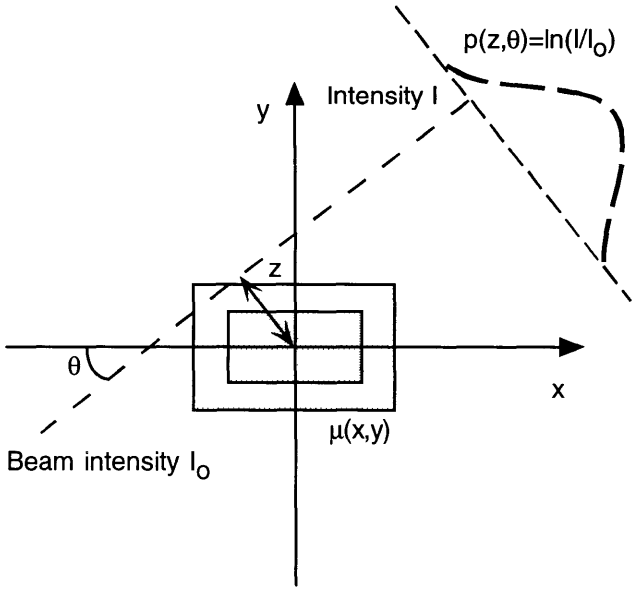

Figure 1.4. CT experiment geometry.

In this representation, a beam of intensity I_0 is emitted from the source, and an attenuated intensity I is measured. From Eq. 2 one can derive an expression for the measurement $p(z,\theta)$:

$$p(z,\theta) = \ln\left(\frac{I_0}{I}\right) = \int\int \mu(x,y)\delta(x\sin\theta - y\cos\theta - z)dxdy \qquad \text{Eq. 3}$$

The transformation from $[x,y]$ space to $[z,\theta]$ space is referred to as the Radon transformation, first described by Radon in 1917 [3]. The p function is called the *sinogram*. An example of a simple $\mu(x,y)$ distribution and its mathematically derived sinogram is shown in Figure 1.5.

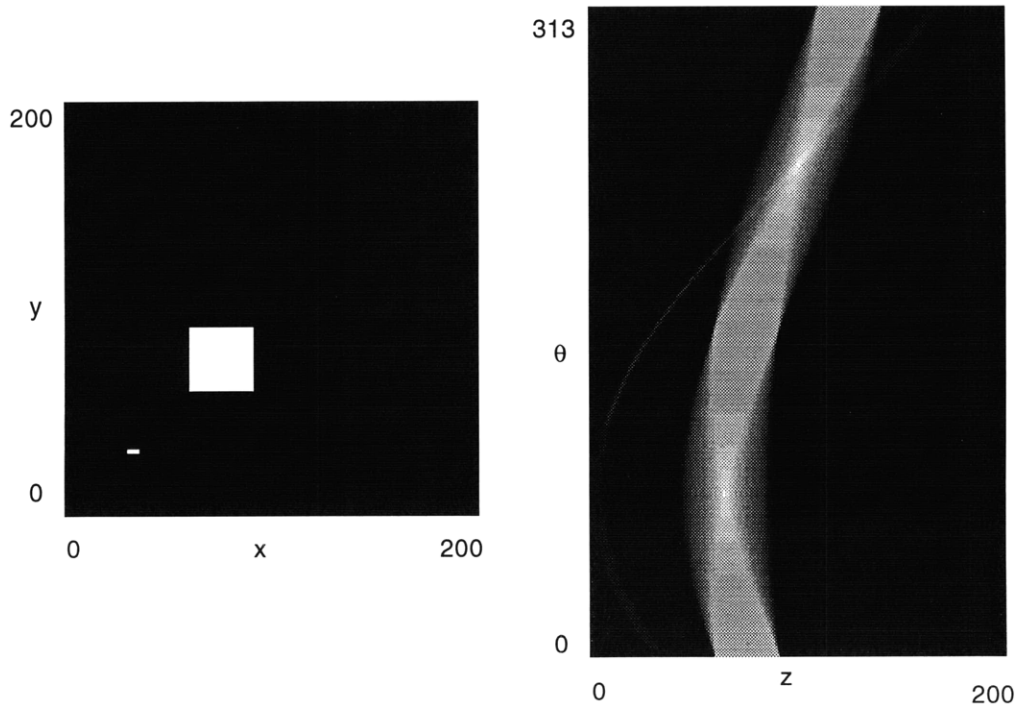

Figure 1.5. Example of a $\mu(x,y)$ distribution (left) and the corresponding sinogram $p(z,\theta)$.

After the experimental acquisition of the p function, it is necessary to invert the data back into its $\mu(x,y)$ form. The simplest method to obtain an approximation of μ is called *backprojection*. This technique consists of evenly re-distributing the integrated linear

attenuation coefficient along the line of projection. Unfortunately, this results in blurry images, as shown in Figure 1.6a.

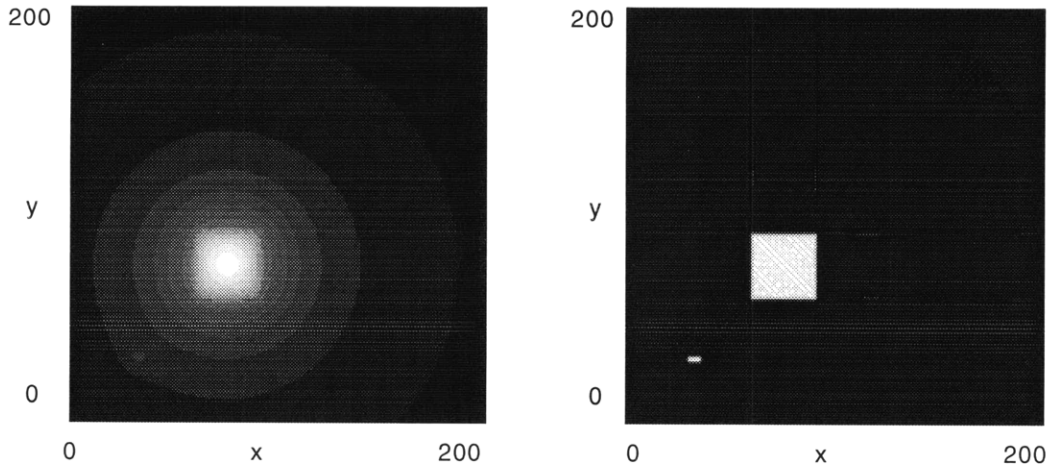

Figure 1.6. Reconstructed μ distribution using unfiltered backprojection (a) and filtered reconstruction (b).

A much more successful technique is *filtered backprojection* (FBP) [4]. A detailed explanation of the mathematical basis of FBP is found in [5]. The image reconstruction algorithm is summarized by the five following steps:

- obtain the sinogram $p(z,\theta)$ experimentally,
- take the z-axis Fourier transform of $p(z,\theta)$ to obtain $P(w_z,\theta)$,
- multiply $P(w_z,\theta)$ by the filter function $|w_z|$,
- take the inverse Fourier transform $p'(z,\theta)$ of the result,
- backproject the filtered sinogram.

As seen in Figure 1.6b, this technique yields excellent images. In addition to being accurate, it also has the advantage that it can be parallelized and executed rapidly on modern computers. For these reasons, FBP is today the prevalent method of image reconstruction in computed tomography. It should be noted however that this method requires the measurement of attenuation data around the entire object.

1.2.2. Types of CT Systems

Historically, CT systems have been categorized into five distinct generations [6]. These generations correspond to successive advances in CT technology.

First generation

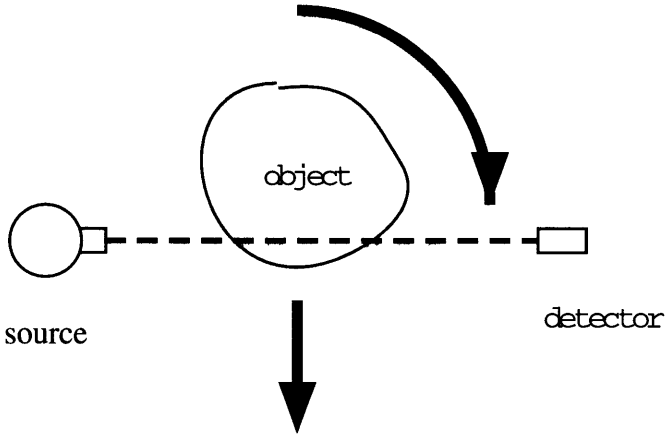

Figure 1.7. First generation CT

The first CT systems built used a single x-ray source and a single detector. Obtaining the complete sinogram required translating the object across the beam, then rotating it by a chosen angular increment, and repeating the procedure over 180°. Obviously, the disadvantage of this method is the long data acquisition time resulting from the need to mechanically translate and rotate the object. This technique presents a number of advantages however. Because the beam is collimated at the source and the detector, the influence of scattered photons is minimized. In addition, detector calibration is not crucial, as all attenuation measurements are made by the same detector and electronics.

Second generation

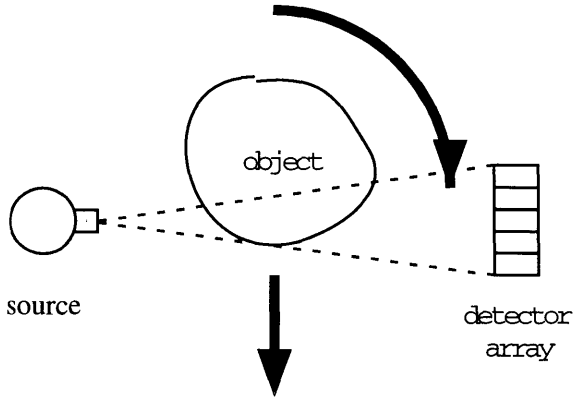

Figure 1.8. Second generation CT

Second generation CT replaces the single detector with an array of N detectors. Although the array is not wide enough to completely encompass the imaged object, imaging time is reduced by a factor of N because the object can be rotated in larger increments. On the other hand, precise calibration of the detectors becomes more important.

Third generation

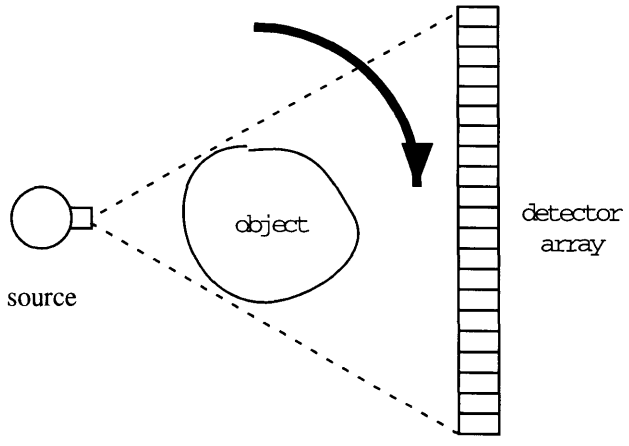

Figure 1.9. Third generation CT

In third generation CT, the detector array is made large enough to encompass the entire object. This setup implies a great speed gain, because object movement is reduced to a rotation. Detector calibration becomes crucial however. Indeed, each detector is responsible of producing the measurements corresponding to a certain radial distance from the object's center of rotation. A miscalibration can result in the presence of ring artifacts in the final images.

Fourth generation

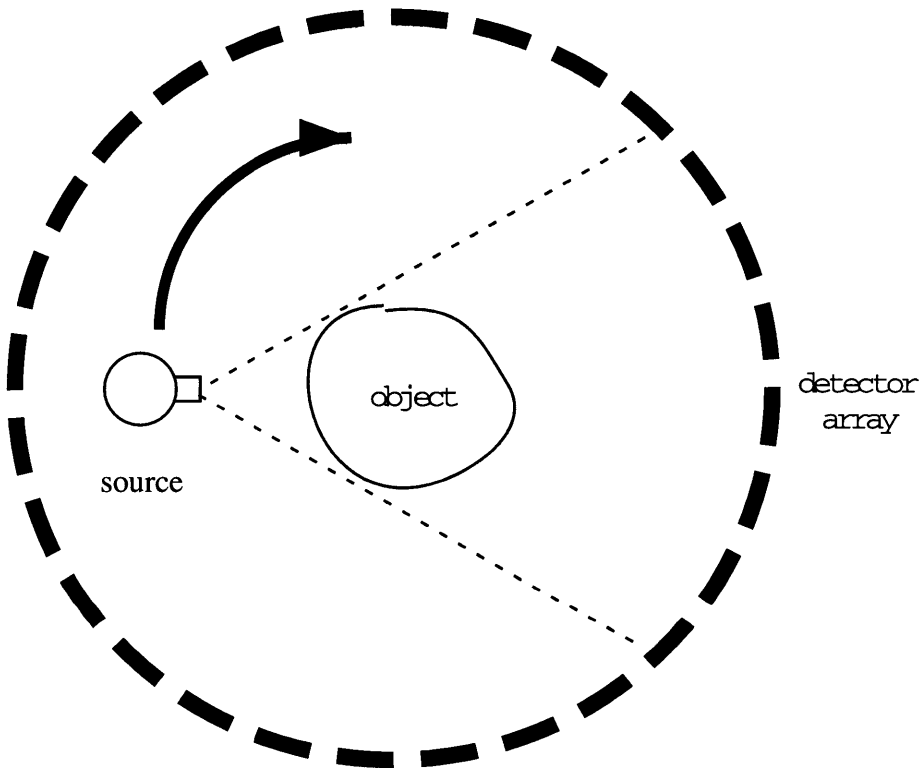

Figure 1.10. Fourth generation CT

Instead of using a linear or an arc array, fourth generation CT uses an entire ring of detectors. Although the cost of the system is increased, calibration issues are less important as in third generation systems because individual detectors are used to scan through the whole

beam. This system is very commonly used in medical CT, where the object must be fixed. In the context of a fixed object, third generation CT involves the rotation of both the source and the detector, whereas fourth generation CT restricts movement to the source alone.

Fifth generation

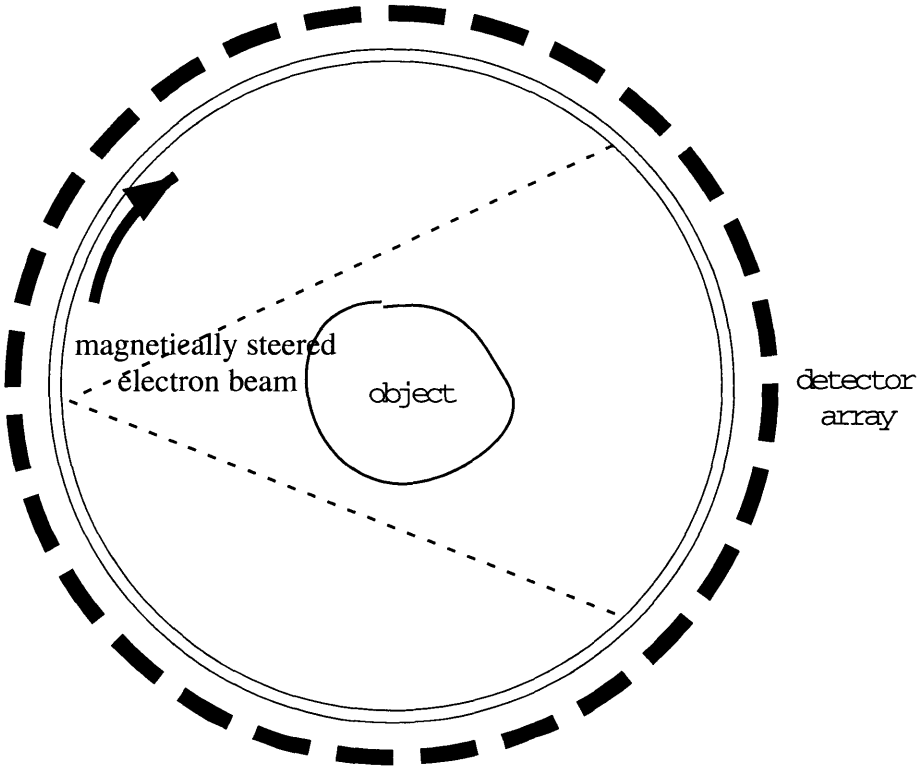

Figure 1.11. Fifth generation CT

All mechanical movements are eliminated in fifth generation CT. Indeed, x-rays are produced by a magnetically steered electron beam. As the beam is rotated around the object, its point of impact with the circular target becomes the source of photons. Such systems offer great speed. Their drawback is their high price.

1.2.3. CT System Properties

CT systems have been built for many applications. Requirements can vary from microscopic resolutions to imaging very large objects. Medical systems require great sensitivity, yet a low dose deposition in the patient is important. Some systems need only distinguish air gaps, which are high contrast features and hence require less sensitivity. For others, sensitivity is crucial in order to differentiate low contrast features. We will now examine some of the important characteristics of CT systems.

System geometry

A CT system is comprised of a source, a detection system, and an object being imaged. Important system variables include the following:

- L, the source to detector distance;
- q, the distance from the source to the system's center of rotation;
- a, the source spot size;
- d, the detector width.

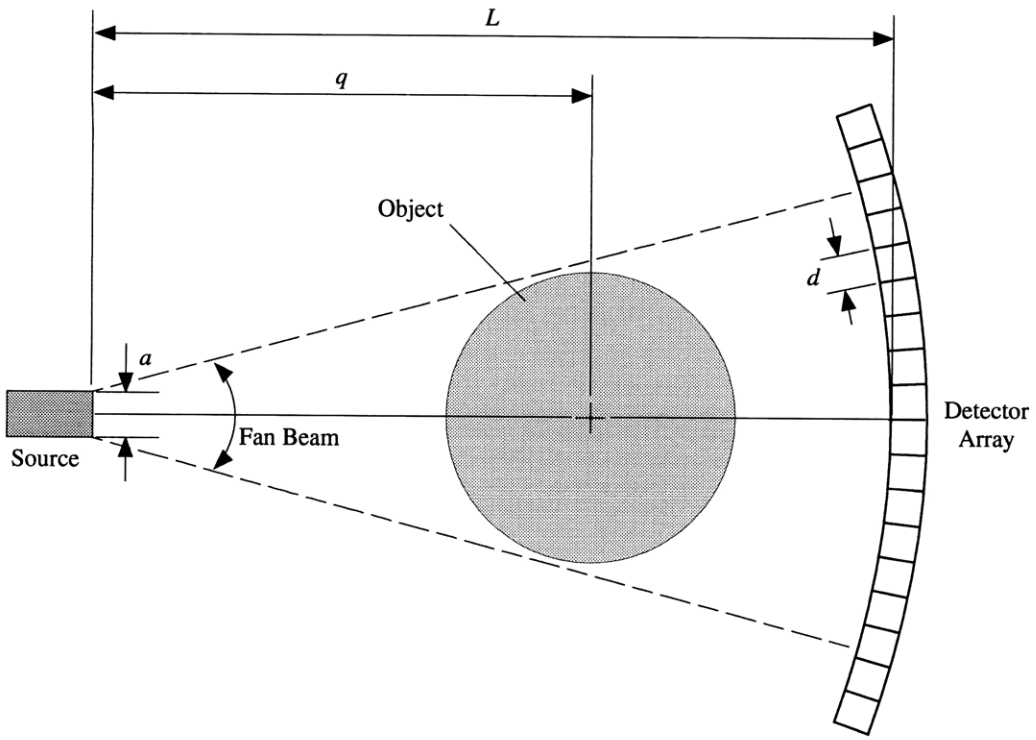

Figure 1.12. CT system geometry.

Sensitivity

Computed tomography provides a value for the linear attenuation coefficient of an object at a certain location. A feature is detectable if it corresponds to a local change in the linear attenuation coefficient. The difference in the coefficient is referred to as the feature's contrast.

$$Contrast = \frac{\mu_f - \mu_b}{\mu_b} \qquad \text{Eq. 4}$$

In Eq. 4, μ_f refers to the attenuation coefficient of the feature, whereas μ_b refers to that of the background. A number of parameters limit the ability of a CT system to accurately measure μ. The accuracy of this measurement is called the *sensitivity*, and it is measured as the standard deviation of the noise in a region of constant density. To distinguish a feature in a CT image, noise level of the system must be lower than the feature's contrast.

Spatial Resolution

Resolution refers to the system's ability to accurately measure the linear attenuation coefficient of small features. Features smaller than the system's resolution will see their apparent contrast reduced by the ratio of their size and that resolution. If the apparent contrast drops below the system's sensitivity, the feature will not be visible.

Two different resolutions characterize CT systems: planar resolution and vertical resolution, or slice thickness. Slice thickness is determined by the height of the x-ray beam at the center of the object. Planar resolution refers to the ability of the system to distinguish features within the slice plane, and is a function of the source spot size, the detector size, and the overall system geometry. A CT system's resolution can be approximated by Eq. 5 [7].

$$resolution \cong \frac{\sqrt{d^2 + [a(M-1)]^2}}{M} \qquad \text{Eq. 5}$$

where

$$M = \frac{L}{q} \qquad \text{Eq. 6}$$

Time resolution

As we have seen earlier, different CT generations acquire attenuation measurements in different manners and with various speeds. The speed at which data collection can be achieved determines the temporal resolution of the system. If a change in the attenuation coefficient of a feature occurs in a period of time shorter than the data acquisition time, a time-averaged value will be obtained. In addition, imaging artifacts can result from rapid

changes, as data from different measurements will not be consistent with the computed tomography mathematical model.

The data acquisition time is proportional to number of photons emitted towards a detector needed to achieve a chosen signal-to-noise ratio (SNR). This number can be calculated from the following expression [5]:

$$N_{emitted} = \frac{e^{\mu l}}{\eta}\left[\frac{SNR}{\mu s r}\right]^2 \qquad \text{Eq. 7}$$

where μ is the linear attenuation coefficient of the imaged object, l is its thickness, η is the detector's efficiency, s is the desired sensitivity and r is the desired spatial resolution. As is clear from Eq. 5, the spatial resolution is roughly proportional to the detector width. Because the number of detected photons is the product of the photon flux, the detector area and the data acquisition time. Consequently, the data acquisition time obeys the following rule:

$$\text{time resolution} \propto \frac{1}{r^3}\frac{1}{r_z}\frac{1}{s^2} \qquad \text{Eq. 8}$$

where r_z is the desired slice thickness.

1.2.4. Energy Requirement

We stated earlier that high-energy x-ray photons were very penetrating. Figure 1.13 shows μ as a function of energy in aluminum. Photons at these energies interact via three major mechanisms, i.e. photoelectric absorption, Compton scattering and pair production. Photoelectric absorption causes a complete deposition of photon energy, whereas the other mechanisms only account for a partial energy deposition. For this reason, an energy absorption curve is shown, and is distinct from the total attenuation coefficient. This last coefficient, representing the photon removal probability, is the important value in x-ray CT.

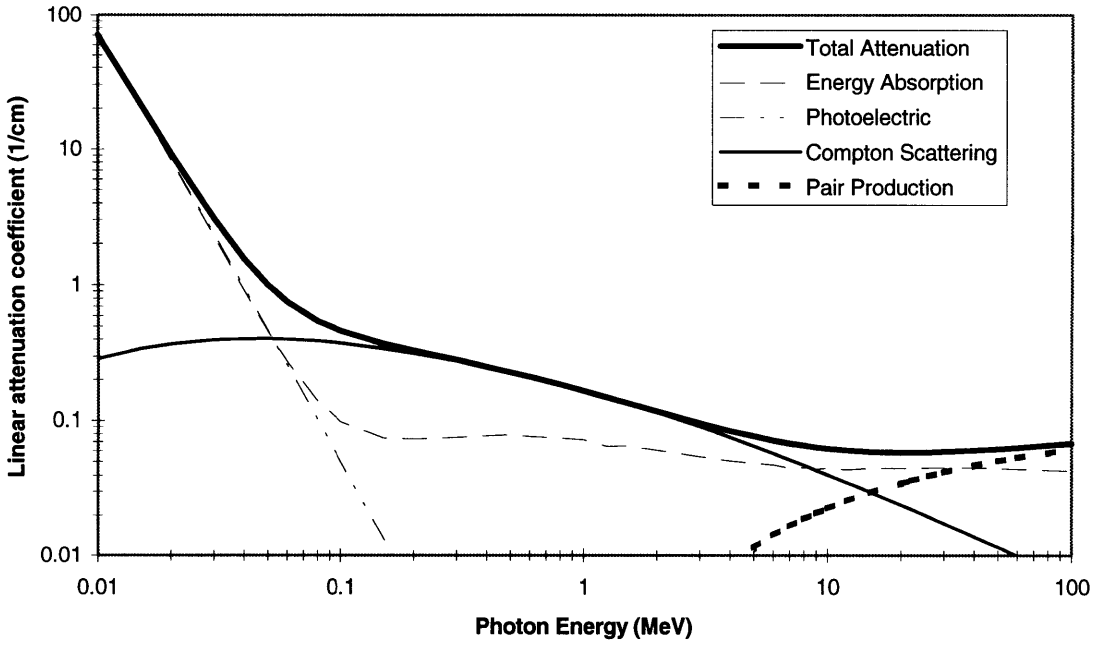

Figure 1.13. Linear attenuation coefficients for aluminum for photon energies ranging from 10 keV to 100 MeV.

Typical x-ray tubes used in medical applications produce x-rays with an average energy close to 60keV and a maximum energy around 140 keV. The attenuation coefficient μ at 60 keV, as seen in Figure 1.13, is about 0.075 mm^{-1} in aluminum. The corresponding half-value thickness, i.e. the material thickness leading to an attenuation of one half, is equal to 9.2 mm. This distance is short and thus makes conventional x-ray tubes inappropriate for CT applications involving thick objects of steel or aluminum. Indeed, an insufficient number of photons, if any, will be detected on the other side of the sample. Above 1 MeV, the attenuation coefficient is sufficiently low to allow imaging of large aluminum samples.

In general, CT imaging is optimized when 90% to 97% of the beam is attenuated by the object [8]. This is achieved when the product of the attenuation coefficient and the length of the object μL is between 2.3 and 3.5.

1.2.5. State of the Art of High Energy Computed Tomography and Solidification Monitoring

Computed tomography was originally used to obtain anatomical cross-sections of human being for diagnostic purposes. Because x-rays are harmful to humans, research in medical CT has focused on improving image quality while using as little radiation as possible. Industrial CT is not limited by dose deposition into the object being studied. However, it has not enjoyed the same success as medical CT because of limitations tied to x-ray source properties. For many applications, x-ray sources were too bulky, too expensive and too weak to be useful. CT imaging was generally limited to very small objects. Advances in linear accelerator technology have recently provided an appropriate source for new applications, and high-energy CT is now a non-destructive evaluation (NDE) tool of growing importance.

One of the first uses of high-energy CT was General Electric's X-Ray Inspection Module [9], which was used to detected high-contrast defects in turbine blades. Another system is ARACOR's Air Force Advanced CT System (AFACTS) [10]. This system was used to examine large rocket motors.

High-energy CT has been used to examine the state of nuclear waste inside drums [11]. A 2 MeV linear accelerator was used to produce the CT images. The linac produced 70 rad/min of radiation at one meter. A detector array containing 896 channels measured photon attenuation. As in the CastScan experiment, individual channels were comprised of a cadmium tungstate ($CdWO_4$) scintillation crystal coupled with photodiodes. The images represented slices 2 to 10 mm thick. Planar resolution was 2 mm, with a density sensitivity of nearly 1%. Data acquisition time ranged from 8 seconds for low-density objects to 20 minutes for denser (2.7 g/cm^3), solid objects.

A high energy CT system was also developed for industrial applications, such as imaging rocket engines or automobile engines [12]. The linear accelerator source had a peak x-ray photon energy of 12 MeV and an average energy of 4 MeV. Detection was accomplished via 15 cadmium tungstate crystals coupled to photodiodes. Slice thickness was less than 3 mm, and a planar resolution of 0.8 mm was achieved. Data was acquired over a period of 10 minutes in a translate-rotate mode.

X-rays have proven very useful in the study the solidification process. Real-time x-ray diffraction experiments using a 320 keV source have been used to detect solidification in nickel and aluminum alloy castings [13,14,15,16]. Low energy sources (20-200 keV) have been used to perform radiography on gallium and aluminum [17].

CT has been used to study the solidification of small samples of cadmium-telluride [18] and aqueous ammonium chloride [19].

Our group first explored the possibility of using CT for solidification monitoring using a Cobalt-60 γ-ray source [20,21]. Unlike the experiment described herein, the source output was continuous and emitted photons at only two discrete energies, 1.17 and 1.33 MeV. The source had an activity of 7 mCi, corresponding to a intensity over one million times less than the source used in the CastScan experiment. A single sodium iodide (NaI) detector was used to measure attenuation. Images of solidifying tin were obtained with a resolution of 3 mm. Data collection time was prohibitively long, lasting 14 days.

1.3. Goals and Contribution

Using computed tomography in the context of continuous casting presents a number of challenges, among which are:

- the high-density of the object under study;
- the low contrast between liquid and solid metals;
- the object under study is fixed in space;
- images must be acquired rapidly.

These requirements demand that the CT system rely on an intense source, such as a linac, but a light and compact one as well. The fast imaging time requires the usage of multiple detectors so that rotate-only acquisition can be accomplished. The systems described earlier often have a sufficient resolution and sensitivity to detect solidification, but are too bulky or use inappropriate data acquisition schemes to be used in this application. Other systems are small enough, but take too long or cannot penetrate large metal objects.

We have built a CT system based on a small, portable linear accelerator with an energy suited for imaging large metal samples. Images were obtained with sufficient resolution and

sensitivity to detect the solidification in a 15-cm wide sample of aluminum. Data acquisition was fast enough to observe, for the first time, the evolution of the solidification process in a large aluminum sample.

In addition, we investigated the possibility of solidification front monitoring using a set of projections obtained over a limited angular range in a translate-only mode. This novel method models the metal cast as a rectangular lower density zone (liquid) within a rectangular aluminum sample of normal density (solid). A theoretical model of the performance of such a system is presented, as well as experimental results confirming the validity of this approach. Such an approach could prove very useful in an industrial environment, where movement is limited, data acquisition time must be minimized, and where proper shielding must be provided.

2. EXPERIMENT DESIGN

Achieving the goals described above required the design and construction of a laboratory-scale solidification system that would lend itself to CT imaging. For practical reasons, aluminum was chosen to be the analyzed metal, because of its low melting temperature (660°C) relative to steel (1500-1700°C). A solidification platform was conceived that would allow the creation of a solidification front in a sample with a size comparable to that of commercial continuous casters. The experimental setup used to achieve this is detailed in section 3.6.1. The important feature of this experiment was that the aluminum sample was shaped as a cylinder 15 cm in diameter.

We will first describe what specifications were chosen in the design of the CT system to achieve the project targets. We will then overview the various components of the sensor and detail their roles.

2.1. Design Goals

As mentioned in section 1.1, a CT system must be able to distinguish a density difference of 9% to observe solidification in aluminum. In actuality, the target contrast must be lower, as 9% is the density difference between molten aluminum and aluminum at room temperature. The actual density difference between liquid and solid aluminum at 660°C is closer to 7% [22]. Another interest of this experiment is the study of solidification in aluminum alloys. Because of this, the system's sensitivity had to be chosen to be at least 5%. To allow for a safety margin, the system was designed to achieve a sensitivity of 1%.

Because the solidification platform presented the advantage of being cylindrically symmetric, it was decided that slice thickness was not critical. A target thickness of 10 mm was chosen. It was considered that a planar resolution of 1 mm would be sufficient.

2.2. General Description

An x-ray computed tomography system is composed of three components:

- An x-ray source
- An x-ray detection system
- A motion system

An object is placed between the source and the detector. The motion system allows the machine to make the x-ray attenuation measurements necessary for a tomographic reconstruction. This involves either moving the object through a stationary x-ray beam, or moving the source-detector pair around the stationary object. Most CT systems are built for medical use, in which case the object under study is a person. For obvious practical reasons, it is necessary to immobilize the patient during the scanning procedure. This requires a sophisticated circular gantry around which the source and detectors are placed. The entire gantry rotates around the patient. An example of such a system is shown in Figure 2.1.

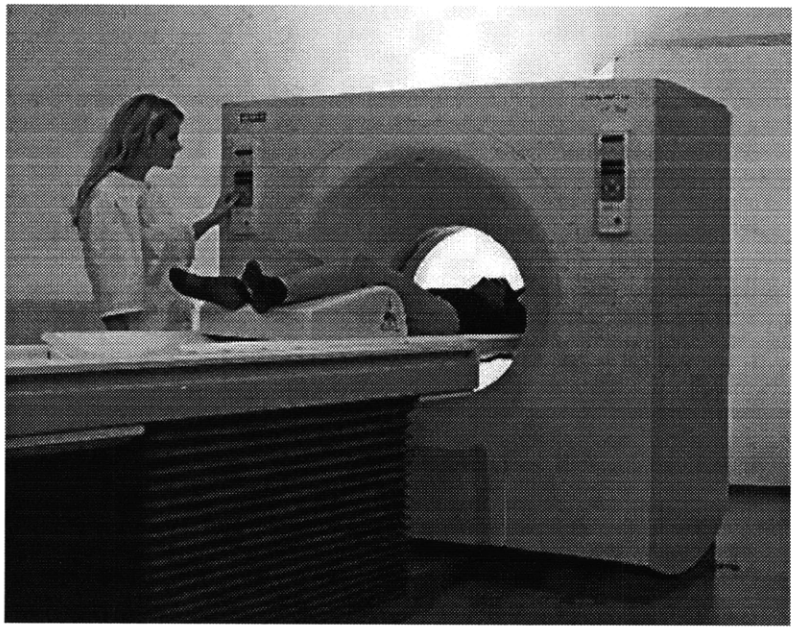

Figure 2.1. Siemens Somatom AR x-ray CT medical imager.

Because the source and the detector system must be precisely positioned with respect to one another, it is often preferable to fix them in space. This is only possible if the object

under study can be rotated and possibly translated. The CastScan system was designed in such a configuration. The overall system layout is shown in Figure 2.2.

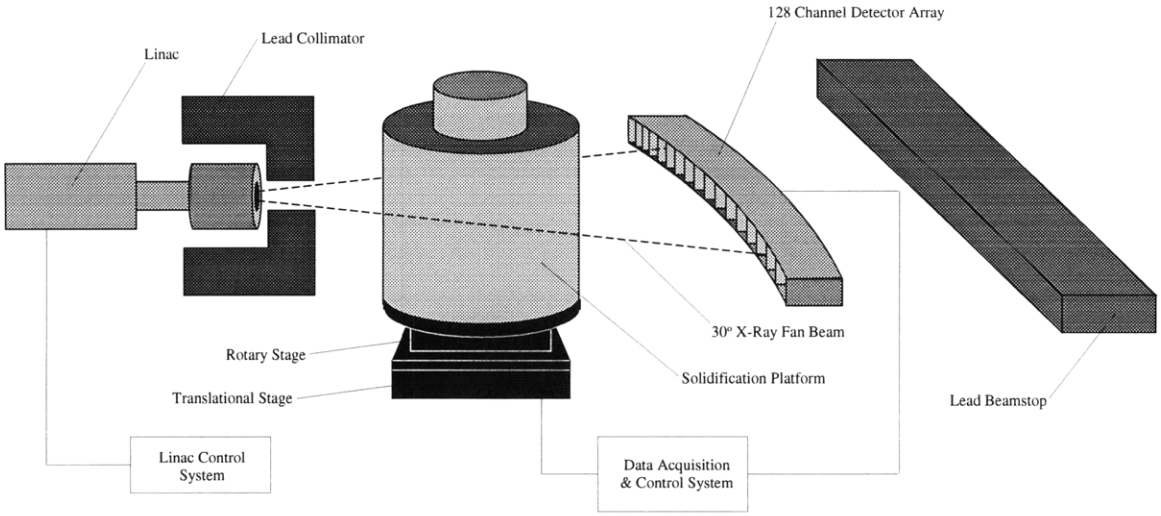

Figure 2.2: CastScan CT experiment setup.

The source produces an x-ray beam configured as a 32° cone. The beam characteristics are detailed in section 2.3.1. A lead collimation assembly further restricts this beam to a 32° fan, with a beam height chosen to satisfy the slice thickness design goals. The x-rays are transmitted through the object under study, placed 50 cm away from the source. This object is placed on a rotational and a translational stage, as described in section 2.3.2. This system allows the measurement of the object's transmission characteristics at the required angles and, if necessary, the required translational offsets. The transmitted photons reach the detector system, composed of 128 individual channels located along a 32° arc, at a distance of 845mm from the source. The properties of the detector system are detailed in section 2.3.3. All these components are placed on an optical table inside a shielded room. The shielded facility is described in section 2.3.4.

2.3. Component Description

2.3.1. Source

The x-ray source is a MINAC-6 linear accelerator, manufactured by Schonberg Research Corporation, of Santa Clara, CA. Most of its characteristics were previously described [5]. This linear accelerator functions by injecting electrons inside a waveguide cavity, where a radio frequency (RF) standing wave is produced by a magnetron. The field's frequency is such that some of the electrons find themselves at the right phase and speed to be accelerated to an energy of 6 MeV. The analogy is often made that those electrons "surf" along a wave in the electric field. At the end of the cavity, the monoenergetic electrons collide with a tungsten target. By a process known as *bremsstrahlung* radiation, part of their energy is converted to photons, called x-rays. These photons are not monoenergetic. Their energies follows the bremsstrahlung spectral distribution, ranging from 0 to 6 MeV.

The MINAC-6 linac is composed of several components, shown in Figure 2.3. Their description follows.

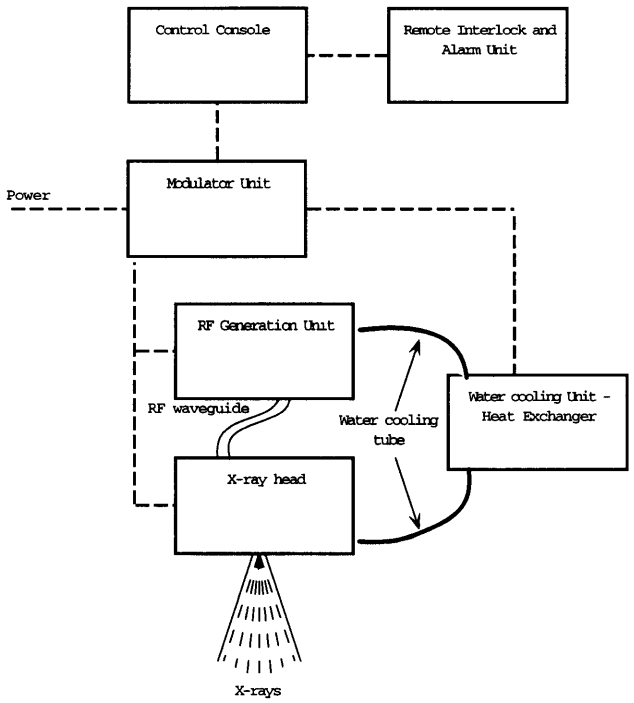

Figure 2.3. MINAC-6 component diagram.

The modulator produces high voltage pulses used by the magnetron and the x-ray head. Pulse rates between 50 and 200 pulses per second are available. Each pulse lasts 4 μs, with a rise and fall time of 0.5 μs. The pulses are externally triggered, typically by the control console.

The RF unit contains the magnetron, which is responsible for the production of the radio frequency radiation. It is driven by the high voltage pulses of the modulator. The radiation is produced in the X-band frequency, at 9303 MHz. It is emitted into a flexible waveguide. The waveguide is filled with SF_6 (sulfur hexafluoride) gas to prevent arcing.

The x-ray head is responsible for accelerating the electrons and producing bremsstrahlung x-rays. It includes an electron gun driven by the modulator, a 52-cm long standing-wave accelerating section, a high-density tungsten target, and a collimator. The length of the accelerating section is inversely proportional to the RF frequency. In addition, a linac's power requirement increases as the square root of the RF wavelength. The high frequency, and hence small wavelength, used in MINAC-6 is of major importance, as it makes this application practical by maintaining the x-ray head to a reasonable size.

The x-ray head receives the RF radiation from the flexible waveguide via a side port. The electron current during a pulse is 50 mA, with an average current of 50 μA, corresponding to a 1000-to-1 duty factor. The electron gun injects 15 keV electrons into the accelerating section. Before colliding with the target, the electrons reach an energy of 6 MeV. The target itself is made of a thin sheet of tungsten. The x-rays produced are then restricted into a 32° cone by a tungsten collimator.

The MINAC-6 x-ray head is shown in Figure 2.4, where the collimator is visible as a metallic cylinder on the right. The center section, in white, houses the RF coupling window and the connections for water cooling tubes. On the left, one can distinguish the power input to the electron gun.

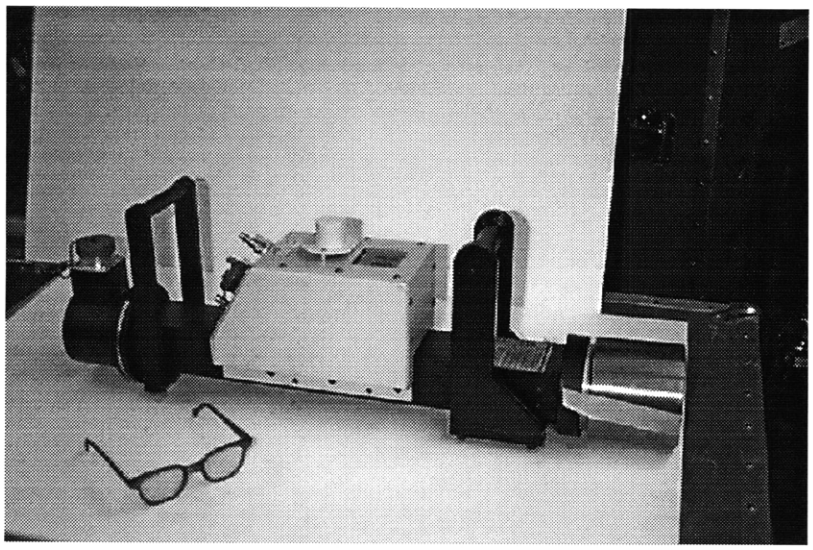

Figure 2.4. Photograph of the MINAC-6 x-ray head

The heat exchanger is a closed-loop water-cooling system that circulates water at 20°C through the RF module and the x-ray head to dissipate the heat produced by those units.

The control console is used to operate the linac and monitor its performance. It is equipped with readouts for the radiation output and the status of the accelerator. It also features a series of LED's that turn on in a sequence corresponding to the power-on procedure. Finally, a remote interlock and alarm unit is designed to reside in the vault in which x-ray head is used.

The linac produces a beam focused at a spot 2mm in diameter. The beam intensity is 300 R/min at a distance of 1 m. As indicated by previous calculations [5], this corresponds to approximately 10^{10} photons/cm^2/s at 1m. The beam's expected spectrum, as calculated in a Monte-Carlo simulation, is shown in Figure 2.5.

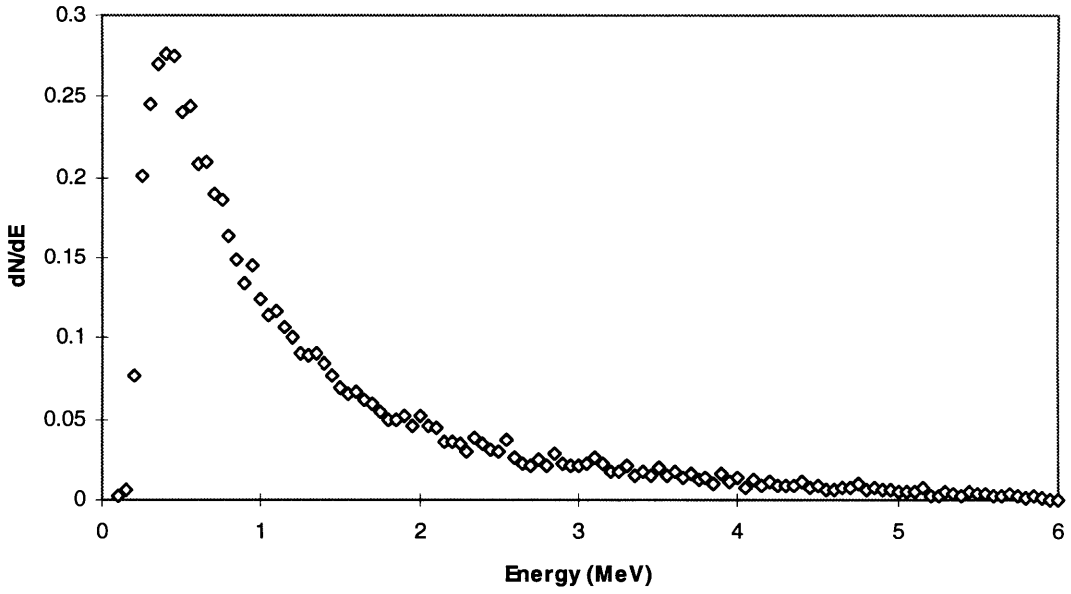

Figure 2.5. Calculated MINAC-6 photon number spectrum
dN/dE

This calculated spectrum shows an expected average energy of 1.3 MeV. The half-value thickness in aluminum for 1.3 MeV photons is 48 mm. The high penetration ability of this beam is crucial to this experiment.

Another attractive feature of this spectrum is illustrated by Figure 2.6, which shows the mass attenuation coefficient μ_m for a variety of materials. The mass attenuation coefficient is the ratio of the linear attenuation coefficient and the material density.

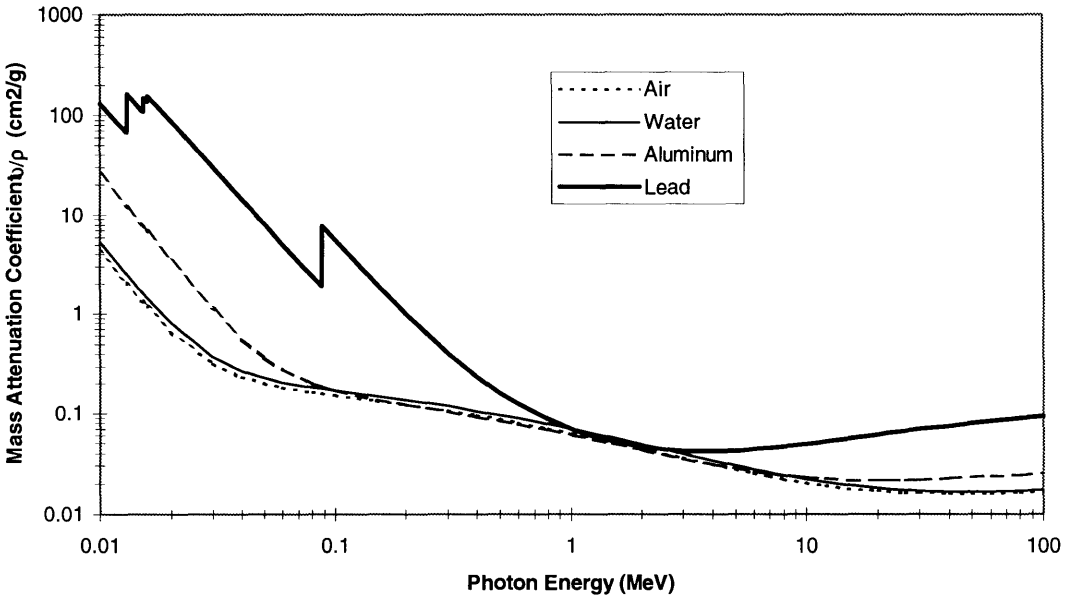

Figure 2.6. Mass attenuation coefficients of air, water, aluminum and lead as a function of photon energy.

A striking characteristic of these curves is their convergence in the 1 to 3 MeV regime. Because most of the MINAC-6 spectrum lies within this range, this system is less sensitive to inhomogeneities in material compositions than otherwise.

To confirm the spectrum calculation, the effective linear attenuation coefficient of the beam was directly measured. It is not possible to obtain a single linear attenuation coefficient value for the beam because it is not monoenergetic. However, one can obtain an aggregate coefficient $\overline{\mu}$ by integrating over the spectral distribution.

$$\overline{\mu} = \int_0^{E_{max}} \mu(E) \cdot \frac{dN}{dE} \cdot dE \qquad \text{Eq. 9}$$

In Eq. 9, E_{max} is the maximum photon energy, and is equal to 6 MeV in this case. The value of $\overline{\mu}$ was experimentally measured using the experimental setup shown in the following diagram.

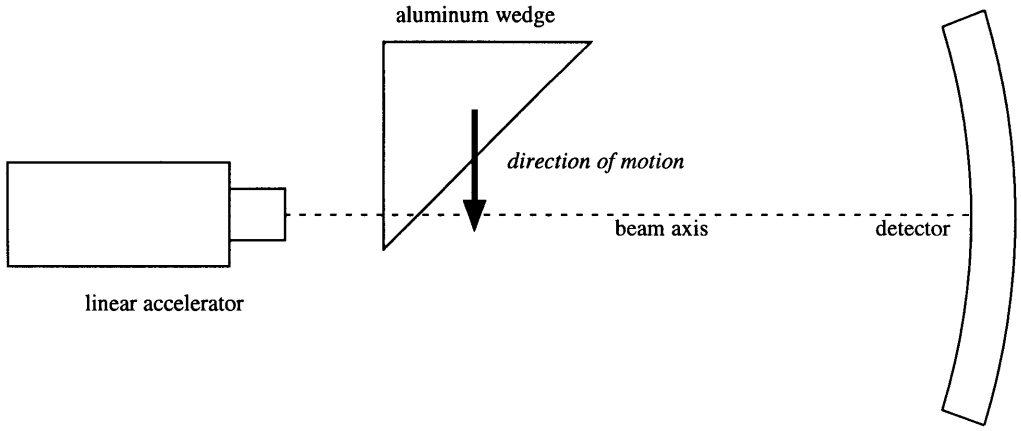

Figure 2.7. Setup for experimental determination of the beam linear attenuation coefficient.

An aluminum wedge was progressively translated through the x-ray beam. The transmitted photon intensity, $I(x)$, was measured by the detector as a function of the aluminum thickness x intersecting the beam. The definition of the linear attenuation coefficient μ is:

$$\mu = -\frac{1}{I(x)}\frac{dI(x)}{dx} \qquad \text{Eq. 10}$$

One can obtain a measure of the change in μ as the beam goes through the aluminum by approximating Eq. 10:

$$\mu(x) = -\frac{1}{I(x)}\frac{\Delta I(x)}{\Delta x} \qquad \text{Eq. 11}$$

The resulting curve is shown in Figure 2.8.

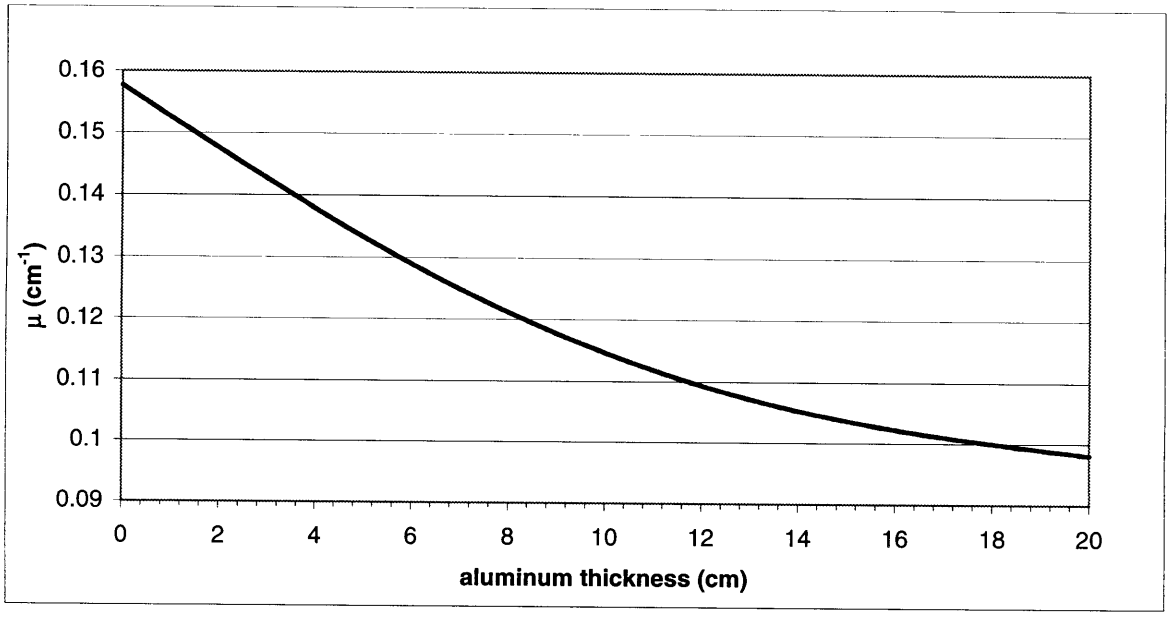

Figure 2.8. Change in the beam attenuation coefficient as a function of the aluminum thickness (beam axis).

As is evidenced by this result, the linear attenuation coefficient of the beam decreases significantly as the photons traverse more and more aluminum. Unfiltered, the beam's coefficient is almost equal to 0.16 cm^{-1}, corresponding to that of a monoenergetic beam at 1.1 MeV. After interacting through 20 cm of aluminum, μ drops to less than 0.1 cm^{-1}, corresponding to a 3 MeV beam. This is phenomenon is well-understood and is known as *beam hardening*. Its explanation can be found by examining Figure 1.13 and Figure 2.5 together. The MINAC-6 beam has spectral components at both low and high energies. Because low energy photons have a greater interaction probability with the medium than high energy ones, they are preferentially removed from the beam. Consequently, the beam's average energy increases, and its aggregate linear attenuation coefficient $\overline{\mu}$ decreases. One important implication of this property is that beam attenuation does not follow the ideal exponential attenuation curve described in section 1.2.1, which can result in artifacts in the final CT image. It is possible to compensate this effect using the methodology described in section 2.4.2.

As mentioned earlier, the MINAC-6 linac can be pulsed between 50 and 200 Hz. Triggering it at 200 Hz can initially appear to be the optimal choice to both maximize the

number of emitted photons and to maximize the number of angular measurements made. We discovered however that using the linac at this repetition rate resulted in a modulation in the beam intensity on the order of 2% (mean absolute deviation). The modulation had a frequency of 20 Hz, i.e. it would repeat every 10 samples. This modulation was caused by a propagation of the 60 Hz power frequency to the linear accelerator's pulse generation system. Modifications to the electron gun power supply provided a significant improvement, reducing the noise level to 1%. Further reducing this noise involved triggering the linac at a frequency of 180 Hz and synchronizing the triggering circuitry with the power lines by using a phase-locked loop scheme. The timing diagrams and circuit diagrams are detailed in the appendix. The modulation remained nonetheless, repeating every three samples. It was reduced to 0.1% by averaging over three consecutive samples, effectively reducing the sampling rate to 60 Hz.

In addition, it should be noted that the linear accelerator did not thermalize until approximately 15 minutes after it was turned on. After that period, the resonance frequency of the system remained stable and did not require manual adjustments.

The CT slice thickness is determined by the vertical extent of the beam as it traverses the center of the object. In its original configuration, the MINAC-6 linac generates its beam in a 32° cone. The desired vertical resolution was 12 mm, requiring additional collimation. A conical brass insert was cut in half and inserted in the 32° tungsten collimator. Additional collimation was provided by using lead bricks. A diagram showing the geometry of the collimation system is shown in Figure 2.9.

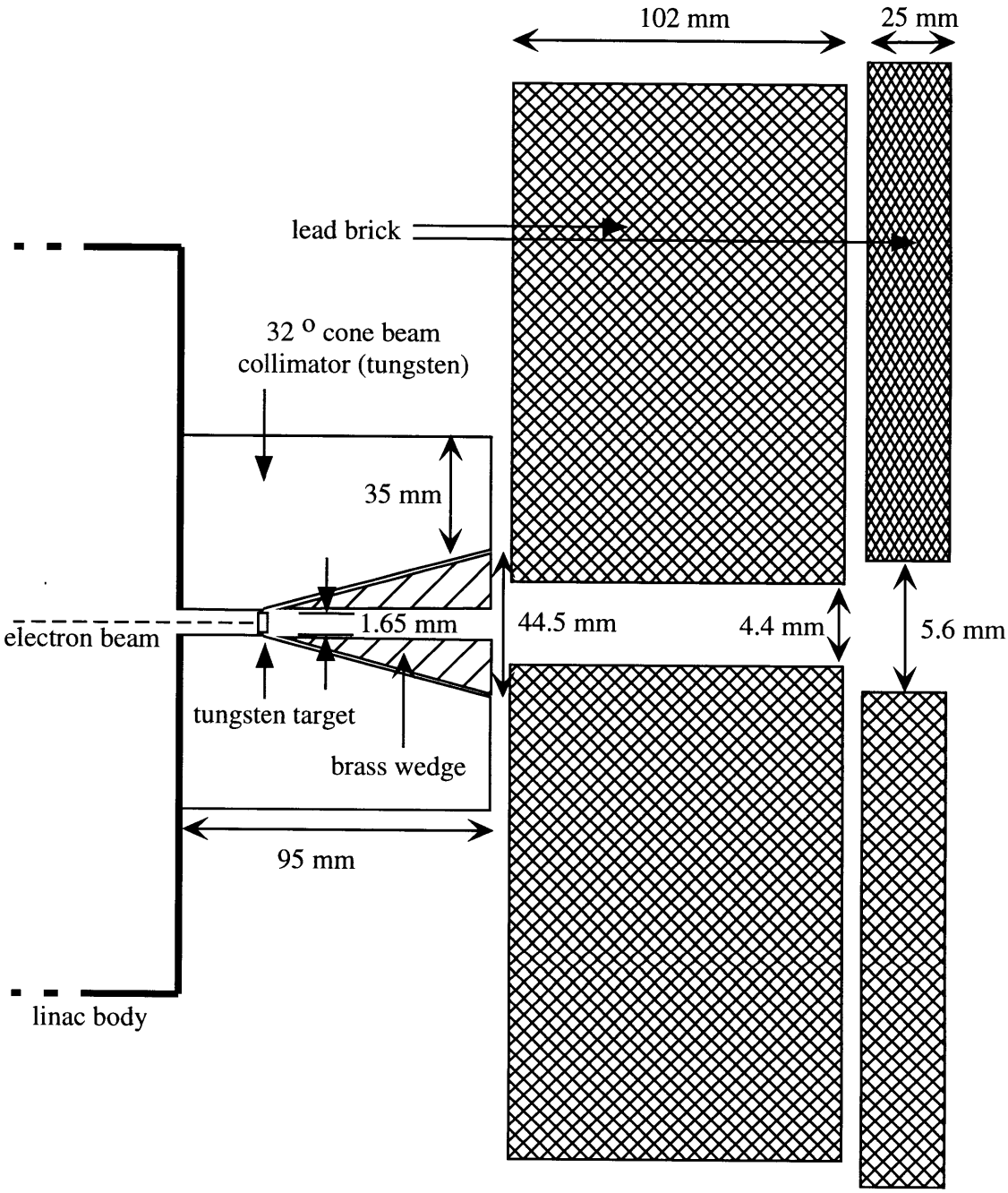

Figure 2.9. X-ray beam collimation assembly.

2.3.2. Motion System

Obtaining the data necessary for CT reconstruction requires the rotation of the object under study. Translation in the direction perpendicular to the beam axis may also be necessary. To achieve this, a motion system was built, comprised of a rotary and a linear translational stage placed underneath it. The rotary stage had a minimum angular step size of 0.01^{o} with an accuracy of 3.0 minutes and a repeatability of 0.3 minutes. The translational stage had a resolution of 0.01 mm and a repeatability of 0.01 mm. Each stage was driven by a 5 V stepper motor. Power and control was provided to the stages by an amplifier placed in the control room. The amplifier was computer controlled. Motion of the linear and translational stages was initiated by a trigger signal originating from the purpose-built circuitry detailed in the appendix. Both the rotary stage and the linear translation stage were operated in an open-loop mode.

A picture of the motion system is shown in Figure 2.10.

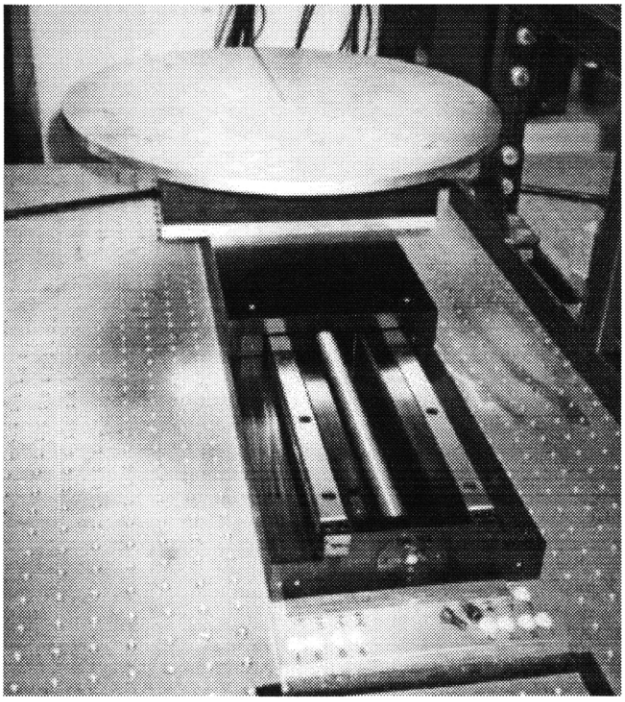

Figure 2.10. Picture of the rotary and linear translation stages.

2.3.3. Detector System

The detector system is based upon a medical x-ray CT system built by Analogic Corporation, of Peabody, MA. In its original form, it consisted of 384 channels placed along a 48° arc with a 845 mm radius. Because the MINAC-6 linac produces a beam 32° wide, only 256 channels were available for x-ray measurements. Furthermore, only one out of two channels was usable because of the need for thick anti-scatter plates placed in front of every other detector. Each channel consisted of a cadmium tungstate ($CdWO_4$) scintillation crystal coupled with a semiconductor photodiode. Scintillation crystals convert x-ray energy into visible light. This light is converted into a current by the photodiodes.

Although the high-energy photons' great penetration ability is an advantage for this application, it makes their detection difficult. To be efficient, a scintillation crystal is preferably dense and thick. Cadmium tungstate is an ideal material for this application because of its high density (7.9 g/cm3). Another significant advantage is its low afterglow. Afterglow corresponds to the delayed emission of visible light from a scintillator after x-ray absorption. Low afterglow is important in high-speed applications such as CT, because many independent measurements need to be made rapidly. The properties of cadmium tungstate are listed in Table 2.1. A discussion of detector technology can be found in [5].

Density [g/cm^3]	7.9
Melting Point [K]	1598
Wavelength of maximum emission [nm]	470/540
Primary Decay Time [μs]	20/5
Afterglow [%]	0.1 after 3 ms
Light Yield [photons/MeV γ]	$1.2\text{-}1.5 \times 10^4$

Table 2.1. Physical properties of $CdWO_4$.

In the CastScan system's configuration, each channel is 1.8 mm wide and 20 mm high. The crystal depth is 3 mm, as seen in Figure 2.11. This small depth explains the low detection efficiency of approximately 4% for the type of beam used in this experiment. At the low

energies used in medical applications, detection efficiency is virtually 100%. Thicker crystals (~30 mm) could achieve efficiencies closer to 50% for our application, if necessary. Beyond this thickness, self-absorption of the emitted visible light might reduce efficiency.

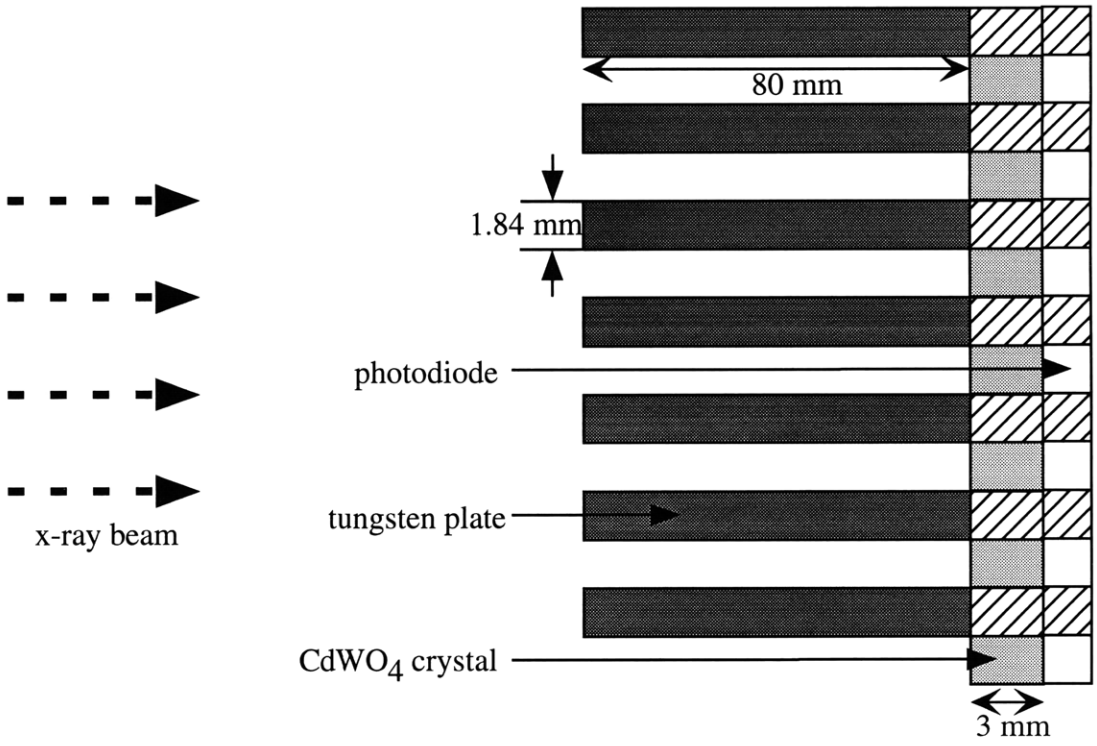

Figure 2.11. Detector and anti-scatter plate configuration.

As shown in the figure above, tungsten anti-scatter plates were placed in between each channel. Most of the interactions between the photons and the object material consist of Compton scattering events. A scattered photon can reach a detector and cause a decrease in the measured attenuation. This leads to artifacts in the images because the CT mathematical model assumes a photon is absorbed after an interaction. The influence of scattered photons can be greatly reduced by anti-scatter plates. These plates of high-density material do not represent an obstruction for unscattered photons because they are aligned toward the beam source. On the other hand, scattered photons usually reach a detector at an angle. The anti-scatter plates attenuate such photons. In our application, anti-scatter plates made of tungsten were used, and measured 80mm in length, 20 mm in height and 1.8 mm in width. Previous

calculations [5] suggested they could help reduce the proportion of detected scattered photons by a factor of a least 6, to about 2%. In addition, collimation in the vertical plane was enhanced by the presence of lead slabs above and below the anti-scatter plates. The slabs were shaped as arcs. The top slab had a depth of 78 mm and a height of 60 mm. The bottom one had a depth of 33 mm and height of 46 mm.

A picture of the detector array is shown in Figure 2.12. The lead collimation is visible above and below the array. Although the detectors are not visible, the tungsten anti-scatter plates placed in front of them can be seen. The data acquisition system (DAS) is mounted above, outside of the path of the beam.

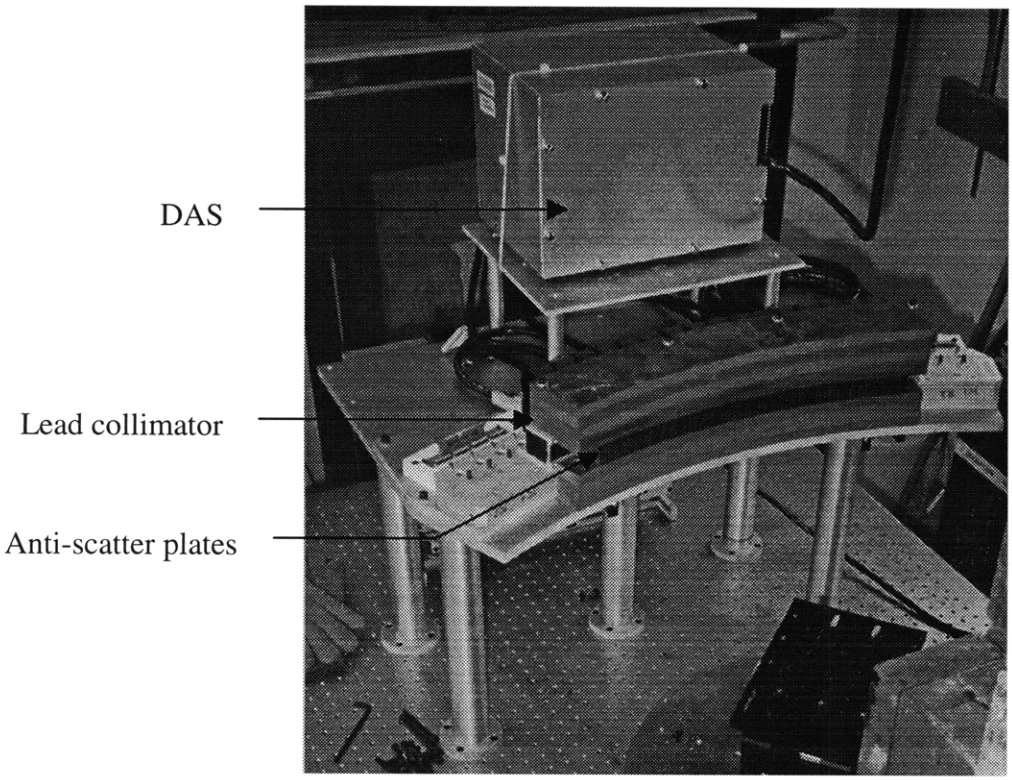

Figure 2.12. Picture of the CastScan detector array.

The photodiodes generate a current proportional to the photon intensity. This current is measured by the data acquisition system, also manufactured by Analogic Corporation. The DAS integrates the current between two measurements, then digitizes the result. The dynamic range of the DAS is equivalent to 22-bits, i.e. a 4,000,000 to 1 ratio. The digital data is then

transmitted to the control room for storage. Data acquisition is triggered externally. A timing diagram is available in the appendix.

One important feature of this system is that a current is generated even in the absence of x-rays. This phenomenon is called *dark current,* and it can cause an error in the measurement if it is not taken into account. The dark current changes with temperature, and is channel dependent. For this reason, it is typically measured in medical applications before and after each experiment. Because our source is pulsed, the dark current is measured between each x-ray intensity measurement by triggering the DAS at twice the linac pulse rate, i.e. at 360 Hz. X-ray intensity is obtained by subtracting the two currents.

2.3.4. Shielded facility

The MINAC-6 linac is a powerful source of penetrative radiation. This radiation can be harmful if proper shielding is not provided. The linac emits radiation at a rate of 300 R/min (18,000 R/hr) at a distance of 1 meter. The beam intensity, emitted from a point source, falls off according to the inverse square law, as shown in Eq. 12, where d refers to the distance from the source in meters.

$$\text{Dose rate}\,[R \cdot hr^{-1}] = 18000 \frac{1}{d[m]^2} \qquad \text{Eq. 12}$$

A shielded room was designed and built to accommodate the linac and provide the necessary x-ray attenuation. It is located at the MIT Bates Linear Accelerator Center, in Middleton, MA. The layout of the room is shown in Figure 2.13.

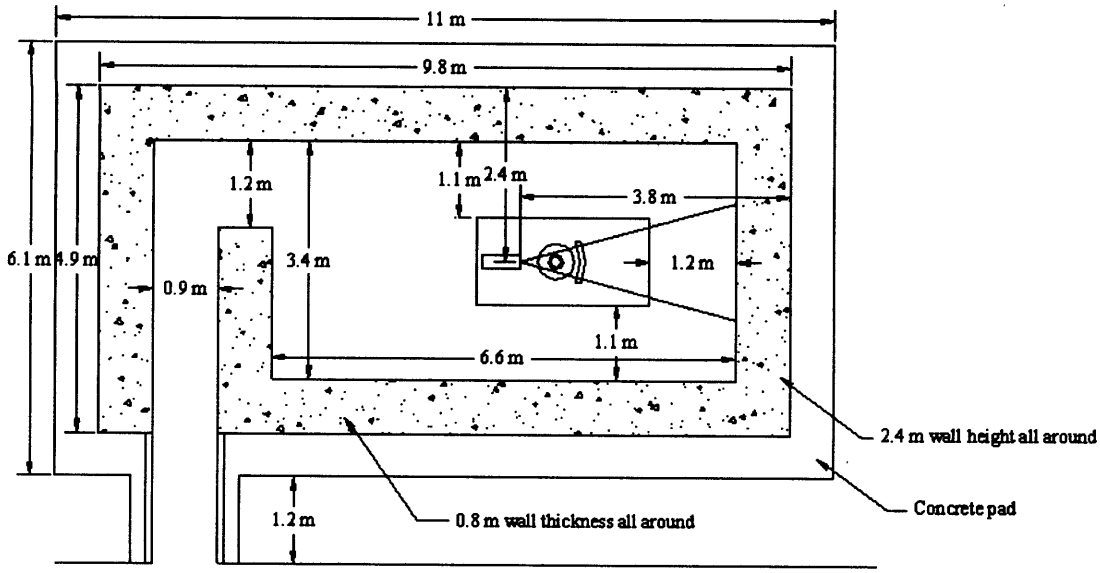

Figure 2.13. Schematic of the shielded room

All the walls in the room were made of concrete and are 30 inches thick. Its entrance followed a maze pattern, allowing for an open design where it is impossible to be outside the room and in the line of sight of the beam or its scatter. Because the beam is much more intense in the forward direction, it was necessary to build a re-entrant beam stopper. This beam stopper was constructed of lead and had a thickness of 30.5 cm. Finally, to reduce leakage radiation emanating from the sides of the source, the entire x-ray head was placed inside a lead "coffin" offering at least 15 cm of shielding in all directions.

Details of the shielding design and calculations were given in [5]. These calculations predicted an attenuation of the primary beam of at least $3x10^{-6}$ by the beam stopper itself. The concrete wall was expected to provide attenuation factors of $4x10^{-3}$ for the primary beam. The maximum dose deposition rate outside the room was therefore expected to be .02 mR/hr. Further simulations taking into account the room geometry and the presence of scattered radiation estimated a maximum dose deposition rate of .18 mR/hr.

Regulations provide two limits that cannot be exceeded to ensure a safe facility. First, the instantaneous dose rate received by any personnel must always remain below 2 mR/hr. In

addition, the maximum total dose to a person in a year is 500 mR. Assuming an overestimated 2000 hours of operation a year, the maximum yearly dose is 360 mR/year, below the 500 mR/year limit.

Direct measurements made on site during the operation of the linear accelerator confirmed that dose rates were undetectable or below predicted values. Dose rates inside the control room were found to be at background levels.

2.4. Data Acquisition and Imaging

We will now discuss the data acquisition procedure, signal processing and image reconstruction. This section describes the procedures in broad terms. Specifics can be found in the appendix.

2.4.1. Data Acquisition Procedure

To increase the data acquisition efficiency of the CastScan CT sensor, the object being studied was continuously rotated. The data acquisition system performed an attenuation measurement on each channel after each linac pulse. The object was rotated at a speed of 8°/s. Covering 360° therefore required 45 seconds. At a pulse rate of 180 Hz, 8100 individual measurements were taken during a rotation.

Because of the large separation between the detector channels, a second rotation was added to the data acquisition procedure. Between the two rotations, the object's center of rotation was shifted by an amount corresponding to half the width of a detector. The rays obtained from the two rotations could then be combined to obtain a sinogram similar to that measured by a 255-channel detector system.

2.4.2. Signal

The computed tomography mathematical model requires that measurements of the integral of the linear attenuation coefficient be taken throughout the imaged object and from all angles. As explained earlier, the DAS measures the current produced by the photodiode at

each channel. If the influence of scattered photons is neglected, this signal can be modeled by the following expression:

$$S_i = I_{0,i} \cdot e^{-p_i} \cdot \eta_i + I_{dark,i} \qquad \text{Eq. 13}$$

$I_{0,i}$ is the signal that would be detected by a perfect detector due the unattenuated beam directed towards detector i. η_I is the real efficiency of the detector i. $I_{dark,i}$ is the dark current produced by the detector i. Finally, p_i is the quantity that must be measured, i.e. the integral of the linear attenuation coefficient along the ray joining the source and detector i. Evidently, obtaining p from S requires prior knowledge of the dark current, the detector efficiency and the beam intensity.

Measurement of the dark current is simple. It can be obtained by turning off the linear accelerator and measuring S. In this experiment, the dark current was measured in the dead time between linac pulses.

Once the dark current is found, it is possible to measure the product of I_0 and η by removing the imaged object and measuring S. This product is referred to as the *flatfield*, as it correspond to the system's response to a uniform (flat) input. Once these parameters have been measured, p is calculated by inverting Eq. 13:

$$p_i = -\ln\left[\frac{S_i - I_{dark,i}}{(I_{0,i} \cdot \eta_i)}\right] \qquad \text{Eq. 14}$$

2.4.3. Beam Hardening Correction

According to Beer's exponential attenuation law, one would expect that the value given by Eq. 14 would be equal to the integral of μ. This would indeed be the case if the beam were monochromatic. As described in section 2.3.1, the beam's spectral composition changes as it traverses an object. Fortunately, it is possible to measure empirically the function relating the amount of aluminum traversed by the beam and the quantity p. The

experimental setup used to measure the change in the linear attenuation coefficient of the beam, described in section 2.3.1, can be used to this effect.

By translating an aluminum wedge of known dimensions through the beam, one can obtain the function $p(\int \rho \cdot ds)$. Inverting p returns the sinogram of the density of the aluminum object $\rho(x,y)$. This inversion is only possible because the object is mainly composed of aluminum. It would not be possible for an object composed of a variety of elements.

2.4.4. Image reconstruction

The computed tomography reconstruction algorithm overviewed in section 1.2.1 assumed a beam geometry where the rays were parallel. In the case of the CastScan system, the detector array is curved and the rays diverge from the source. Such a configuration is referred to as a *fan-beam geometry*.

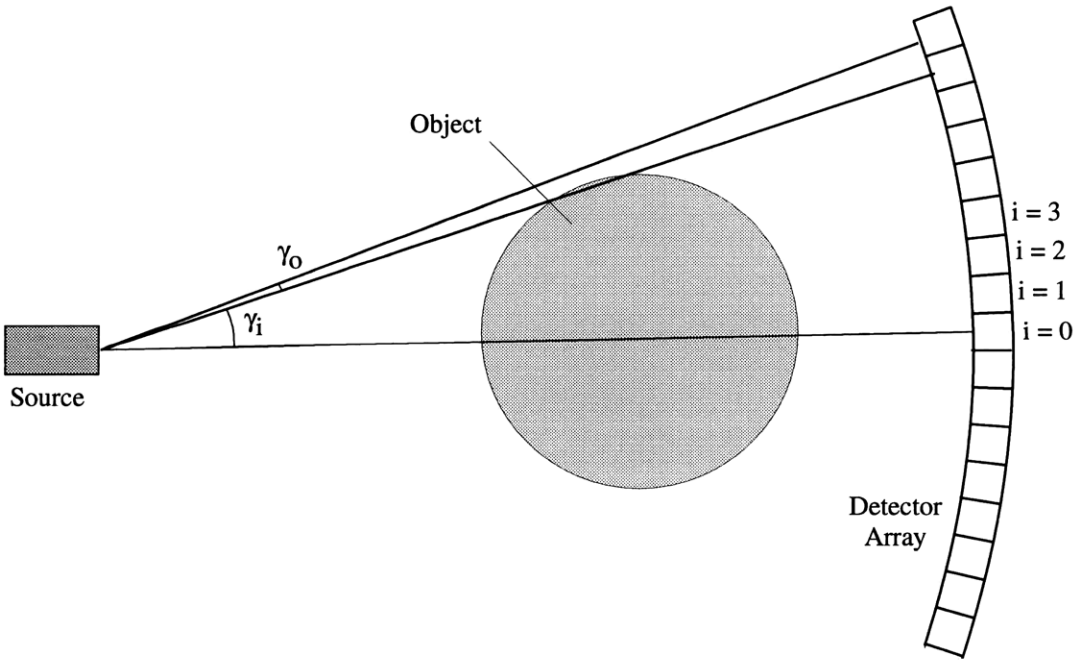

Figure 2.14. CT using a fan-beam geometry.

Instead of obtaining the projection data in $[z,\theta]$ space, it is obtained in $[\gamma,\theta]$ space. Filtered backprojection is still possible, but it requires additional steps.

First, a cosine weighing function is applied to the projection data p, such that:

$$p^*(i) = p(i) \cdot \cos(\gamma_i) \qquad \text{Eq. 15}$$

where γ_i is the angle between the ray i and the beam axis. The resulting function is then filtered. The filtering process is described in terms of the following convolution operation:

$$p^{**}(i) = \sum_{i'} p^*(i-i') \cdot q(i') \qquad \text{Eq. 16}$$

where

$$f(i) = \begin{cases} \pi/4 & i = 0 \\ -\dfrac{\gamma_0^{\,2}}{\pi \sin^2(\gamma_i)} & i \text{ is odd} \\ 0 & i \text{ is even} \end{cases} \qquad \text{Eq. 17}$$

Finally, the filtered data $p^{**}(\gamma,\theta)$ is backprojected into [x,y] space. Let $w(x,y,\gamma,\theta)$ be the function describing the length of intersection of the ray described by (γ,θ) and the pixel at (x,y). Standard backprojection corresponds to the following expression:

$$\rho(x,y) = \frac{\int_{\theta,\gamma} p(\gamma,\theta) \cdot w(x,y,\gamma,\theta)}{\int_{\theta,\gamma} w(x,y,\gamma,\theta)} \qquad \text{Eq. 18}$$

In the case of a fan beam geometry, the function w must include an additional weighing factor:

$$w' = \frac{w}{s^2} \qquad \text{Eq. 19}$$

where $s(x,y,\theta)$ is distance of between the source and the pixel at (x,y) with the object rotated by an angle θ.

2.5. Expected Performance

Returning to the framework described in 1.2.3, the CastScan system can be described in terms of the following geometrical parameters:

L (source – detector distance)	845 mm
q (source – object distance)	500 mm
a (source spot size)	2 mm
d (detector width)	1.8 mm

Table 2.2. Geometrical properties of CastScan system.

Using Eq. 5, the expected maximum resolution of the system is 1.35 mm. A similar calculation can be carried out to obtain the vertical resolution. Using a detector width d equal to 20 mm, Eq. 5 yields an expected slice thickness equal to 12 mm.

Sensitivity is a mainly a function of the noise in the system. Assuming the detector electronics do not contribute to noise, a CT system will be limited by the photon statistics. Photon emission is a random process that follows Poisson statistics. The variance in the number of emitted photons is equal to the square root of this number. Even a perfect system will be limited by this law. Reducing photon noise therefore implies longer data acquisition times and stronger sources.

The data acquisition time necessary to achieve a sensitivity of 1% was previously calculated to be 15 seconds [5]. The calculation assumed a linac pulse rate of 200 Hz.

Because this pulse rate was modified to 180 Hz, the expected data acquisition time was increased to 17 seconds.

The expected performance characteristics of the CastScan system are summarized in the following table:

Planar resolution	1.3 mm
Slice thickness	12 mm
Sensitivity	1%
Time resolution	17 sec

Table 2.3. Expected performance characteristics of the CastScan CT system.

3. EXPERIMENTAL RESULTS

In this chapter, we will review the measured performance characteristics of the CastScan CT system. We will examine the topics of spatial resolution, sensitivity and temporal resolution. We will also discuss the topic of image artifacts. We will then address the system's ability to identify the solidification front in pure aluminum. Finally, performance and future improvements will be discussed.

3.1. Data Acquisition Parameters

As stated in section 2.4.1, attenuation measurements were made at 8100 different angle positions around imaged objects. Because of source fluctuation issues which are examined in detail in the appendix, consecutive angular samples were averaged together in groups of three, yielding a total of 2700 views in a sinogram. Each view consisted of 255 ray measurements.

3.2. Spatial Resolution

Planar Resolution

The planar spatial resolution of a CT system can be obtained by a series of measurements [7]. The procedure consists of the following:

- Obtain the CT image of a cylindrical object.
- Obtain the edge response function (ERF) by plotting the density profile from the center of the cylinder to the edge of the image.
- Calculate the line spread function (LSF) by taking the radial derivative of the ERF.

- Calculate the modulation transfer function (MTF) by taking the Fourier transform of the LSF.

The ERF shows how the system responds to the presence of a sharp edge in an object. Ideally, the drop-off in density would be infinitely sharp. However, the limited resolution of the system will result in a blurring of the edge. The LSF measures the sharpness of the drop-off. A CT system's resolution is equal to the full width at half maximum (FWHM) of the LSF:

$$resolution = FWHM(LSF) \qquad \text{Eq. 20}$$

Finally, the modulation transfer function gives the system's response to features of a given spatial frequency. For example, if the MTF is equal to 0.8 for a spatial frequency of 0.1 mm, a grid with 10-mm spacing will appear as a density modulation with an amplitude equal to 80% of the actual contrast.

To perform this measurement, an aluminum alloy cylinder with a 100 mm diameter was imaged in the system. The resulting tomogram is shown in Figure 3.1, along with the corresponding three dimensional surface plot in Figure 3.2.

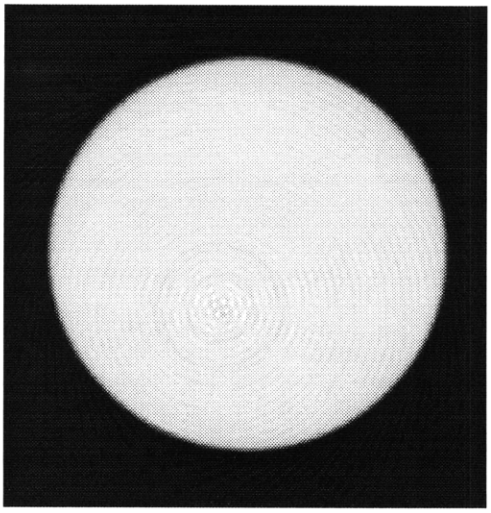

Figure 3.1. CT image of an aluminum cylinder.

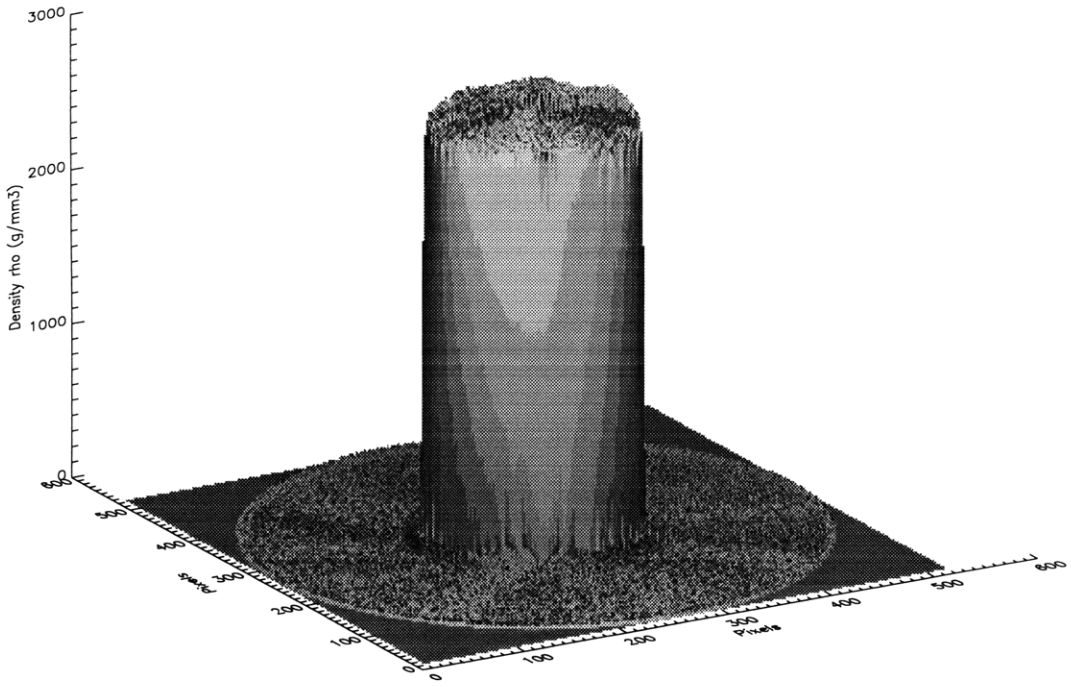

Figure 3.2. Surface plot of an aluminum cylinder tomogram.

From the center of the cylinder, a series of 360 radial density plots were obtained and averaged. The resulting edge response function is shown in Figure 3.3.

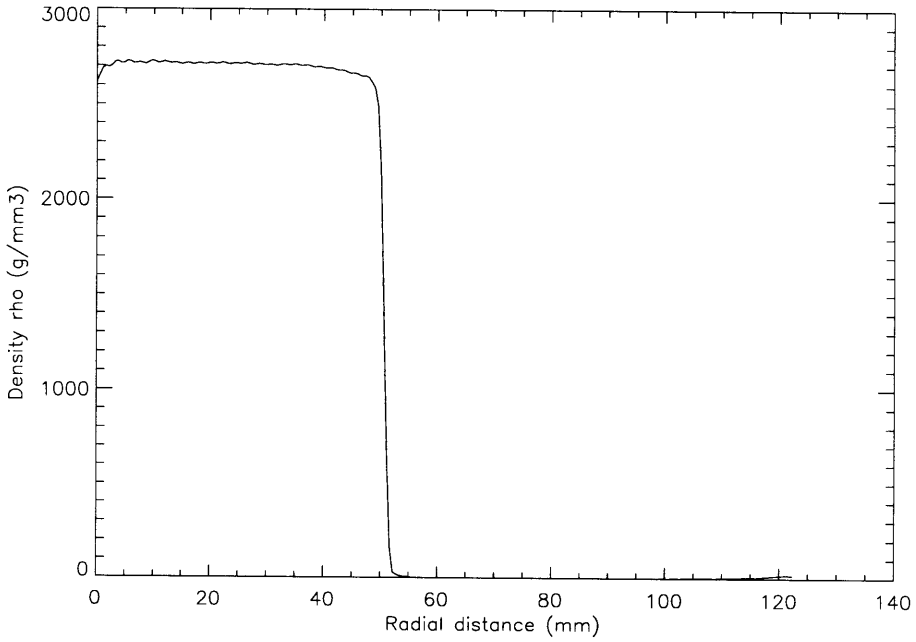

Figure 3.3. CT system edge response function (ERF).

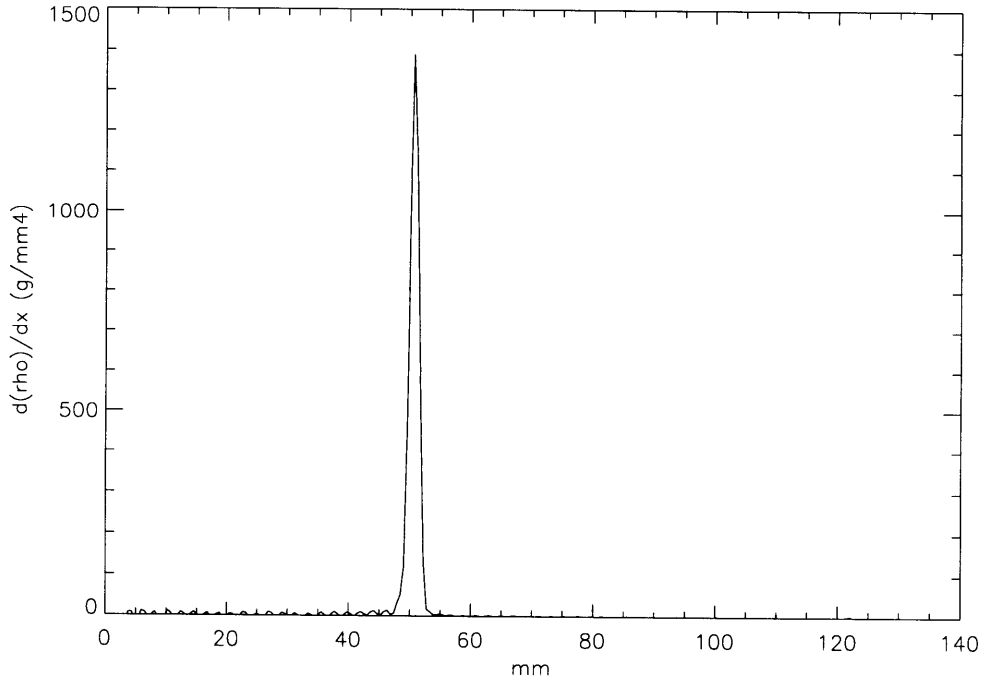

Figure 3.4. CT system line spread function (LSF).

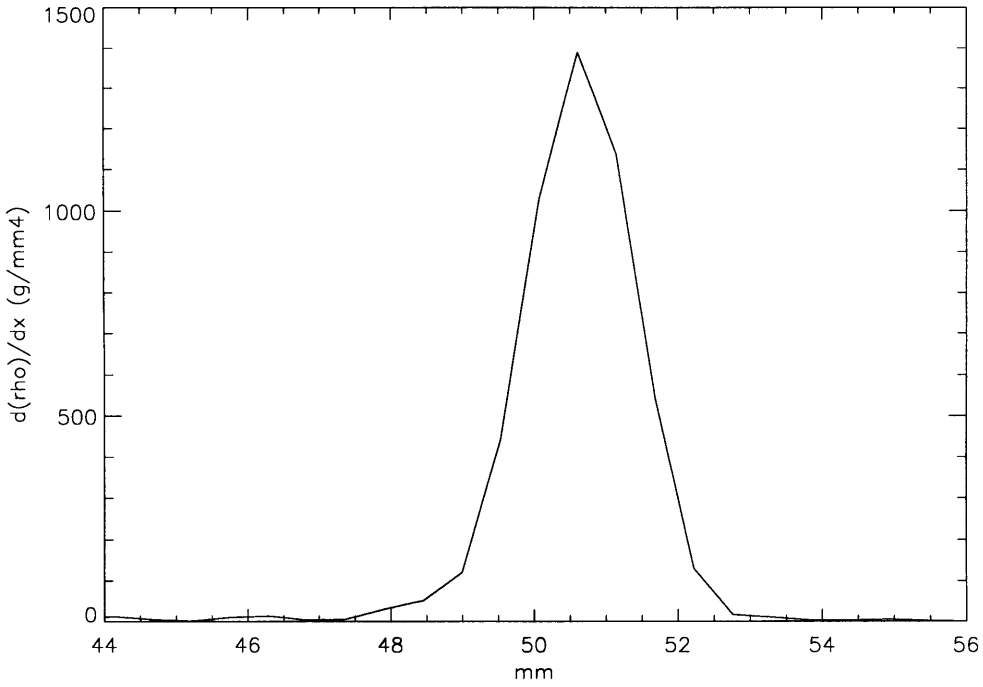

Figure 3.5. CT system LSF (detail).

Figure 3.4 shows the line spread function obtained from the measured ERF. Because the LSF is critical to calculating resolution, it is shown in detail in Figure 3.5. Measuring the FWHM of the LSF yields a resolution of approximately 1.6 mm. Finally, the modulation transfer function is shown in Figure 3.6.

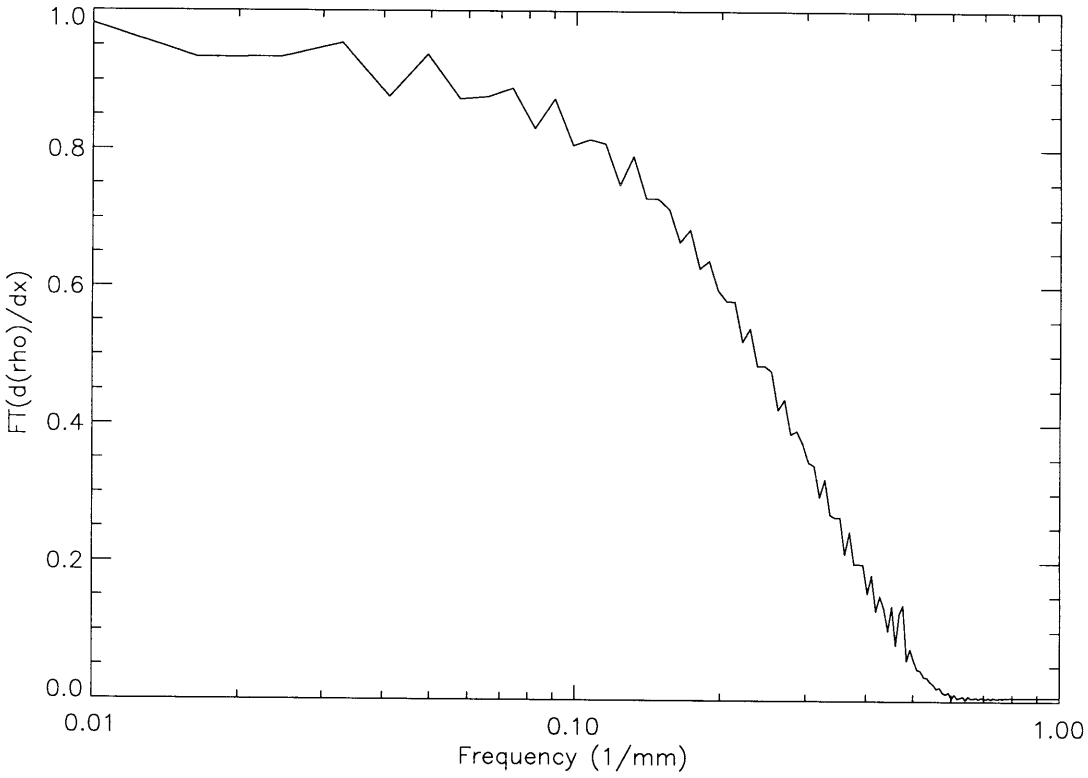

Figure 3.6. CT system modulation transfer function (MTF).

To verify the CT system's resolution, an aluminum block was manufactured. The block was 133 mm long, 52 mm wide, and 24 mm thick. A number of holes were drilled through it, with diameters ranging from 3mm to 1mm. A picture of the block is shown in Figure 3.7, along with a corresponding schematic (Figure 3.8).

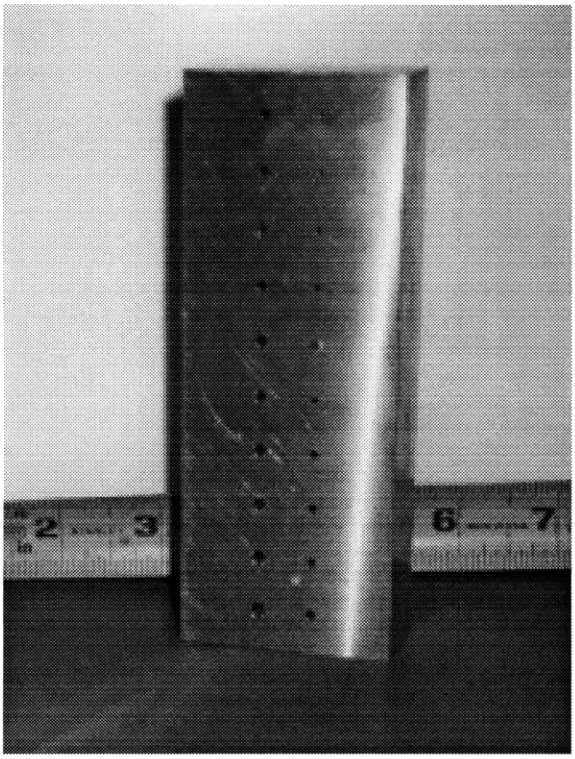

Figure 3.7. Picture of aluminum block with drilled holes.

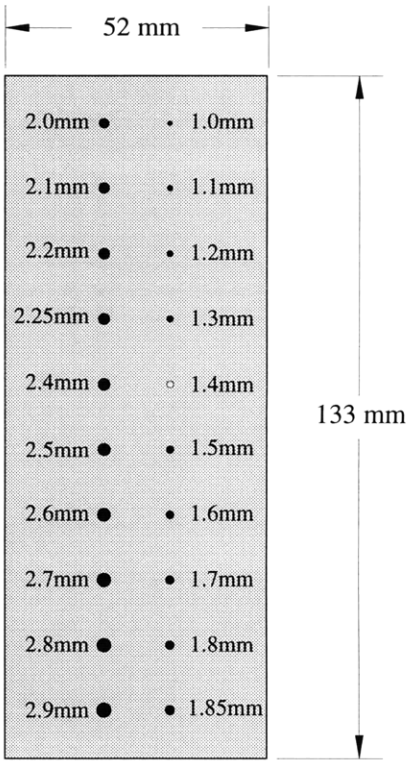

Figure 3.8. Schematic of aluminum block with drilled holes.

The resulting CT image is shown in Figure 3.9.

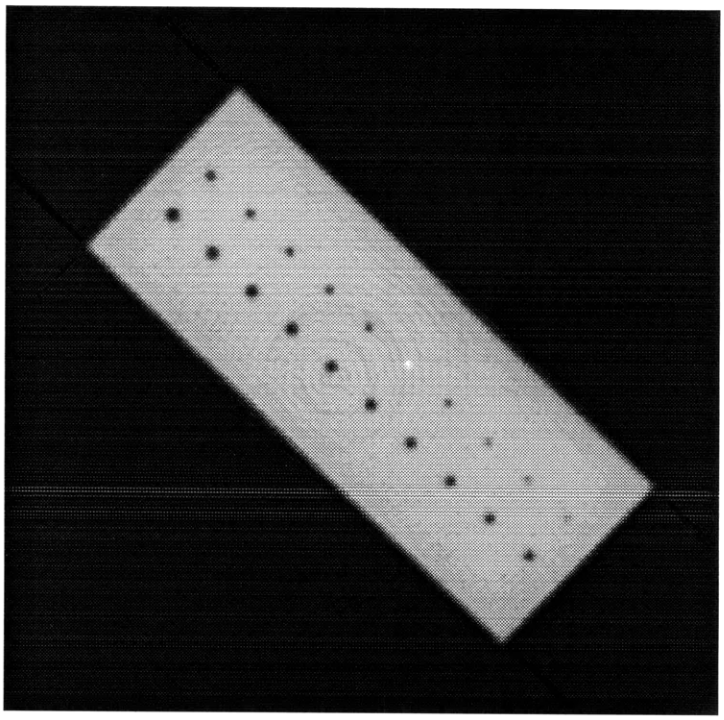

Figure 3.9. CT image of aluminum block with drilled holes.

All the holes are visible in the picture, although it is apparent that holes smaller than 1.5 mm suffer from a decreased contrast. During the manufacture of this object, a drill bit was broken in the 1.4 mm hole. It is evident as a bright dot.

Slice Thickness

The slice thickness of a CT system is its vertical spatial resolution. To measure this value, a rectangular block of aluminum was machined with a 0.5 mm deep depression. The dimensions of the block are given in Figure 4.3. A second rectangular block of identical dimensions was placed above the first one. The resulting object was 127 mm long, 76 mm wide with a rectangular air gap within it. The air gap was 108 mm long, 57 mm wide and 0.5 mm deep. The resulting tomogram is shown in Figure 3.10.

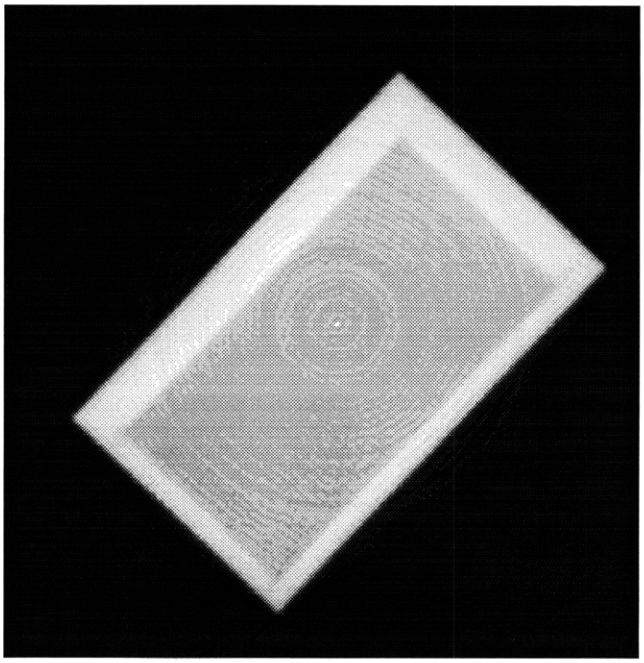

Figure 3.10. Tomogram of an aluminum block with a 0.5- mm deep air gap.

The experiment revealed an 11% apparent density difference between the solid aluminum outer area and the inner partially void area. The slice thickness is therefore equal to 0.5 mm divided by the contrast, i.e. 4.5 mm.

3.3. Sensitivity

The sensitivity of a CT system is determined by the noise level in the image of an object of constant density. Traditionally, this noise level is measured by calculating the fractional standard deviation in the density distribution within a region of interest (ROI). This calculation was performed using the CT data obtained from the aluminum cylinder discussed above, and using an ROI comprising over 20,000 pixels. The resulting sensitivity was found to be approximately 1.5%.

3.4. Temporal Resolution

Data acquisition for a single image requires two 45-second rotations of the object being imaged. Time is required for the acceleration and deceleration of the object being imaged. In addition, the object needs to be translated back and forth by half a detector width between scans. Finally, synchronizing the DAS, the motors and the linac takes additional time. Overall, image acquisition is accomplished in 120 seconds. This time is equal to the time resolution of this system.

3.5. Artifacts

The image quality is usually not uniform in CT images. We will now discuss what can cause this to happen, and how these problems have manifested themselves.

3.5.1. Detector Drift

As stated in section 1.2.2, third generation CT systems are very sensitive to detector calibration imperfections. The miscalibration of a detector will affect all the data collected at a certain radius from the center of rotation of the system. As a result, rings can appear in the final image. Figure 3.11 shows the image of the aluminum cylinder introduced in section 3.2. The contrast has been increased to emphasize the ring artifacts, and the image has been blurred to de-emphasize the source drift artifact discussed in the following section.

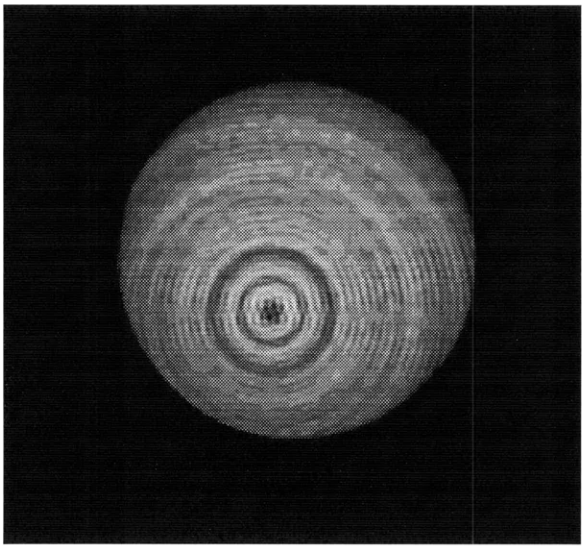

Figure 3.11. Detector drift ring artifact example.

3.5.2. Source Drift

The intensity of the x-ray source was not perfectly uniform. Power supply fluctuations can affect the beam. In addition, thermal changes in the linac waveguide can lead to changes in the resonant frequency of the system. Such drifts can cause the intensity and/or the angular spectral distribution of the beam to change.

The CastScan CT system did not attempt to take into account source fluctuations in interpreting the attenuation data. In addition, the data was collected in two rotations, resulting in ray measurements that were interleaved. Because the filtered backprojection filter is a high-pass filter, the high spatial frequency fluctuations caused by the source drift resulted in closely packed rings. Figure 3.12 shows an example of this effect in our test cylinder. The contrast was increased to emphasize the rings.

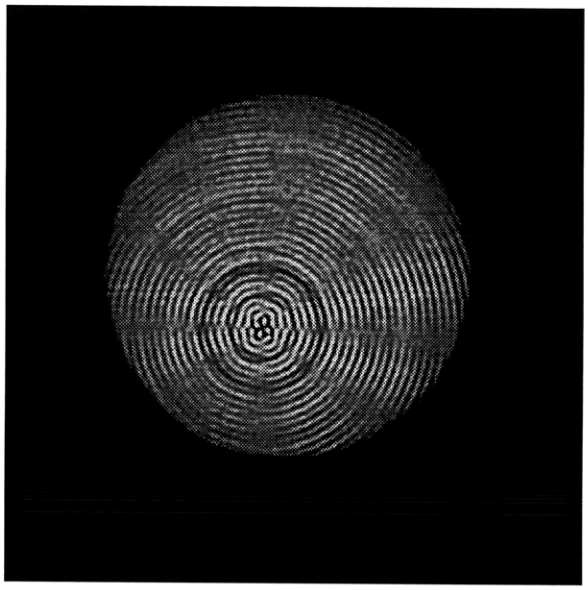

Figure 3.12. Source drift ring artifact example.

3.5.3. Undersampling Artifacts

As in all sampling processes, undersampling is a critical issue. Sampling theory indicates that a signal of frequency f must be sampled at the Nyquist frequency to insure accurate reproduction [23].

$$f_{\text{Nyquist}} = 2 \cdot f_{\text{Signal}} \qquad \text{Eq. 21}$$

If the sampling frequency is lower than the Nyquist limit, the sampled signal will be reproduced as a lower frequency harmonic. In CT systems, sampling is performed in two dimensions: angular space (θ) and translational space (z).

Consider a system that meets the planar resolution requirements to measure an object of diameter D. If this system samples the attenuation along N_z translational steps, the object is scanned with a resolution equal to $r = D/N_z$. For systems that require angular measurements over 360°, maintaining this performance requires sampling a circle of radius πD with a resolution r, so that:

$$N_\theta = \frac{\pi D}{D/N_z} = \pi N_z \qquad \text{Eq. 22}$$

Although this calculation is true for parallel-beam CT systems, it also holds for fan-beam systems. This expression tends to overestimate the required number of angular steps because most objects do not contain much high frequency information in that dimension.

As stated earlier, the data acquisition method used in the CastScan system results in 255 rays sampled over 2700 angles. According to Eq. 22, 765 angular steps would be sufficient to maintain resolution. For this reason, angular undersampling was not expected to be a concern. Indeed, Figure 3.13 shows the contrast between a properly sampled imaged (a) and a severely undersampled image (b). Undersampling is particularly severe because of the high frequency content of the object in the polar axis.

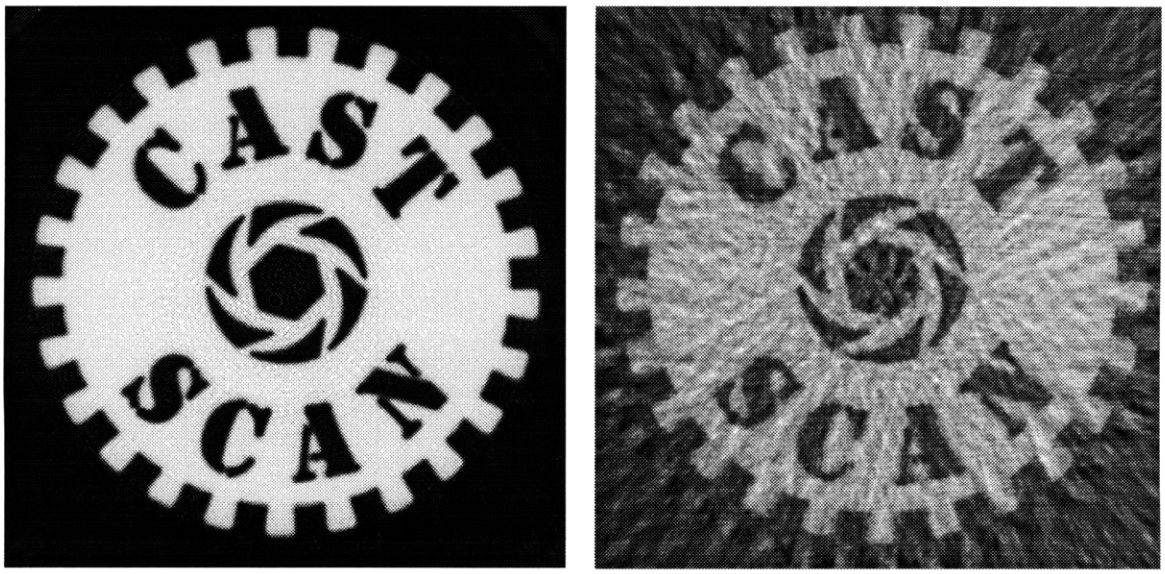

a. CT image with 2700 views. b. CT image with 67 views.

Figure 3.13. Angular undersampling artifact example.

Undersampling in the translational dimension can occur if a feature is smaller than the system's resolution. Figure 3.14 shows an image of the aluminum cylinder reconstructed with only half of the 255 rays available. The image contrast was modified to emphasize the streaks visible around the edge of the cylinder, which is a high frequency feature.

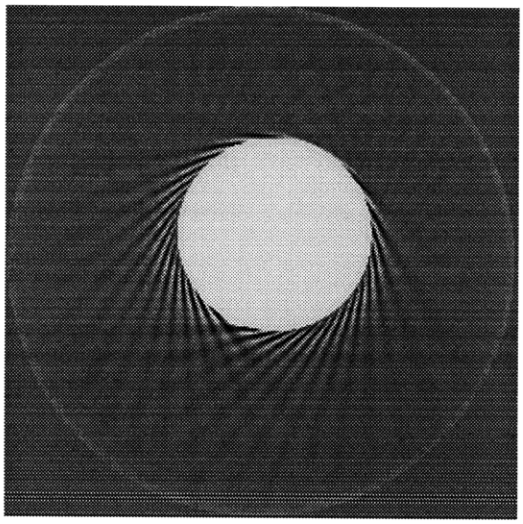

Figure 3.14. Translational undersampling artifact example.

3.5.4. Beam Hardening Artifacts

As explained in section 2.4.3, the signal measured by the detectors was corrected to compensate for the beam hardening effect caused by the multi-spectral properties of the x-ray beam. This correction was crucial, as illustrated by Figure 3.15. As can be seen, the beam hardening artifact manifested itself as a drop in the measured density at the center of large objects. The correction solved this problem, as can be observed in the cross-sectional plots (c,d).

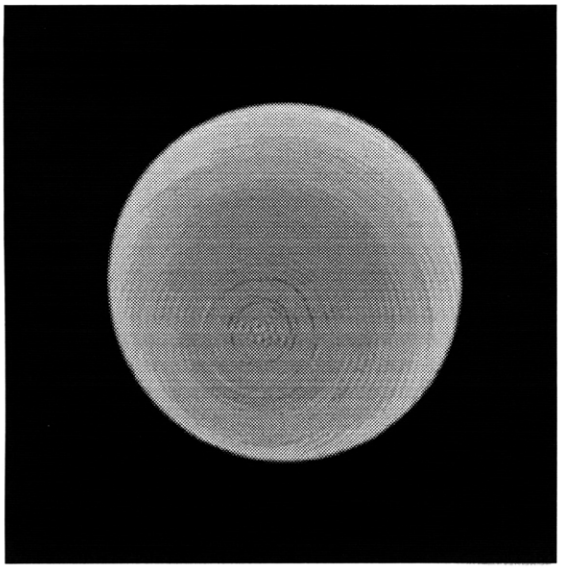

a. Uncorrected image.

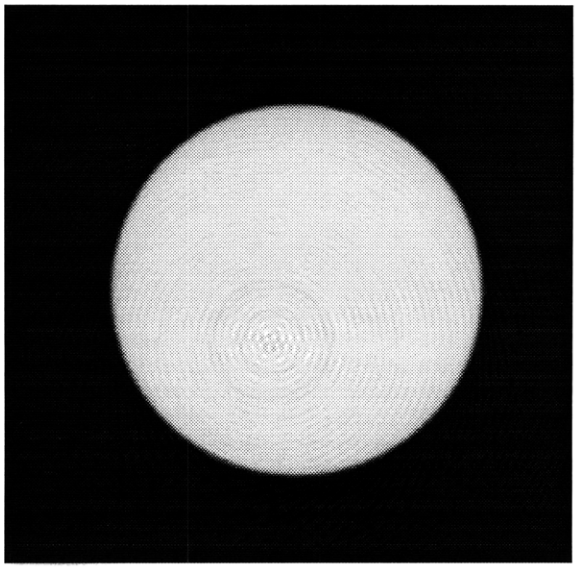

b. Beam-hardening corrected CT image.

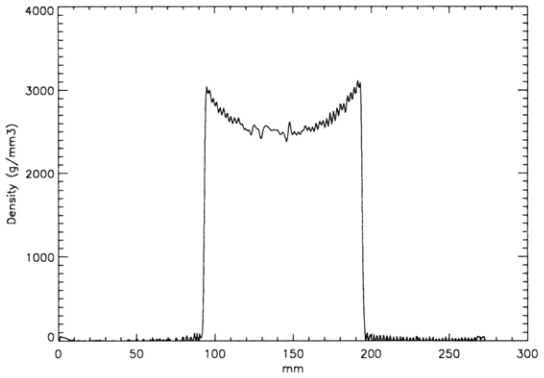

c. Cross-sectional plot of (a).

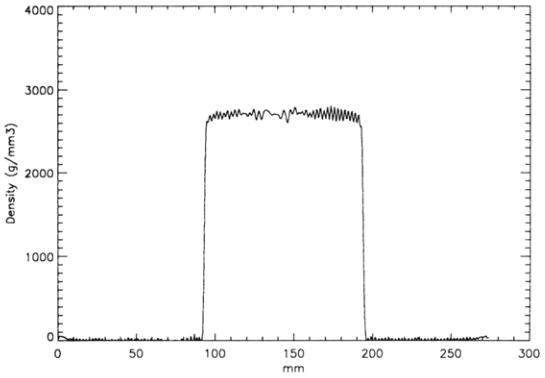

Cross-sectional plot of (b).

Figure 3.15. Beam hardening artifact example.

3.6. Example: Pure Aluminum Solidification

The CastScan CT system was designed to identify the solidification front in aluminum. To verify the sensor's ability to perform this task, a solidification experiment was conducted in the laboratory. The experiment and the computed tomography results are described in this section. Further details may be found in [24].

3.6.1. Experiment Description

Because of the size constraints imposed by the CT system's dimensions, a cylindrical furnace was chosen to melt aluminum. A cylindrical graphite crucible was placed inside the furnace. Pure aluminum (99.9%) was melted in the crucible. To sustain a solidification front, a cooling system was placed at the center of the sample. The cooling apparatus was composed of two stainless steel tubes concentrically placed. Compressed air was channeled through the inner tube, and exited from the section between the tube walls. To monitor the temperature of the aluminum melt, sixteen thermocouples were placed at various radial positions. The thermocouple tips were placed in the imaging plane to accurately measure the temperature of the imaged section. The entire solidification platform was placed on the rotary and linear stages. Figure 3.16 shows a side view of the experimental setup.

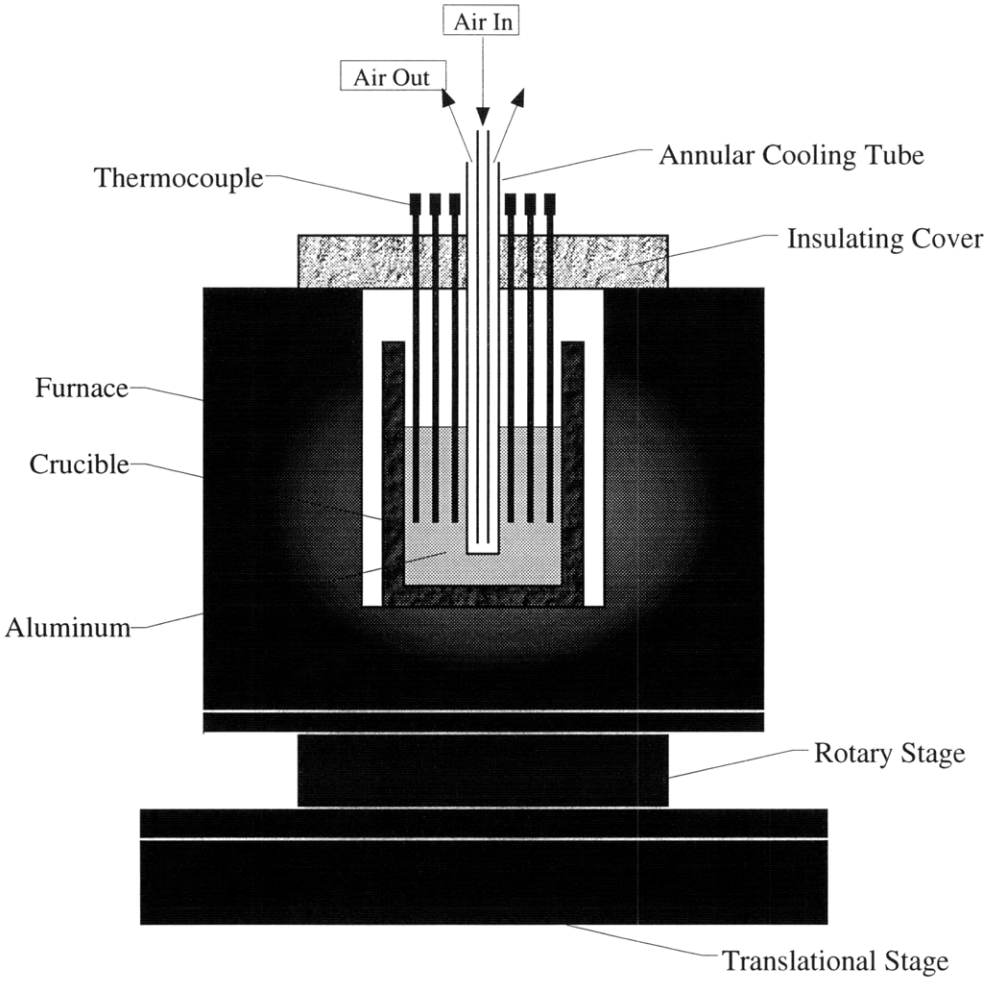

Figure 3.16. Side view of the solidification platform.

The dimensions of the furnace and crucible are shown in Figure 3.17, as well as their composition.

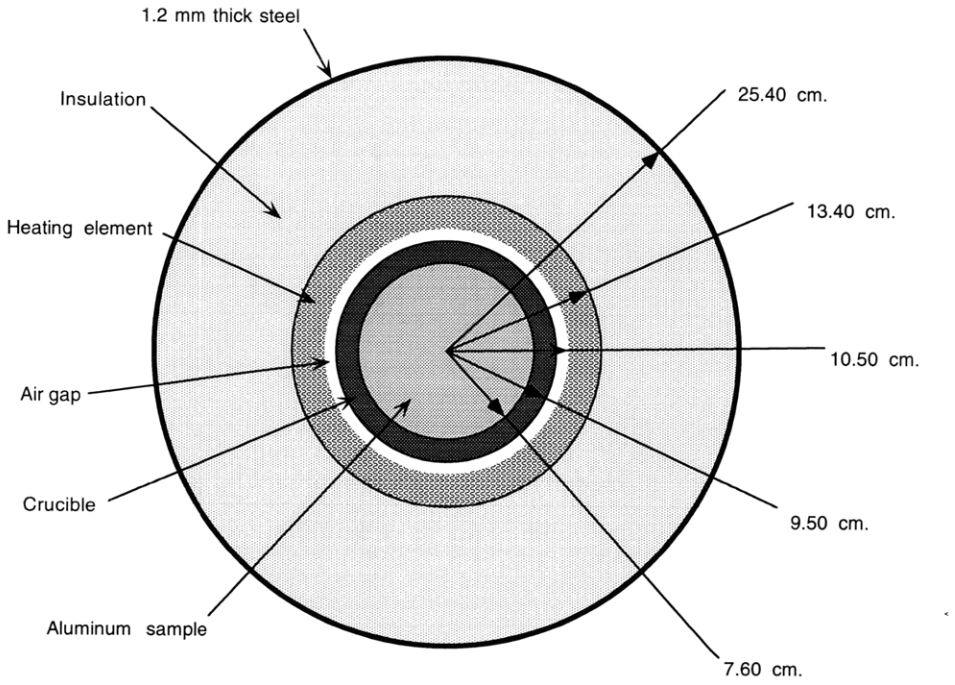

Figure 3.17. Cross sectional of the furnace, with dimensions.

Because the furnace is larger than the beam width, it could not be imaged using this CT system. It was possible to image the crucible and its contents however. Let $\mu_{fur}(x,y)$ be the linear attenuation coefficient distribution of the furnace, and $\mu_{cru}(x,y)$ be that of the crucible and its contents. Eq. 3 can be decomposed in the following way:

$$\begin{aligned} I &= I_0 e^{-\int_0^s \mu(s')ds'} \\ &= I_0 e^{-\int_0^s (\mu_{fur}(s')+\mu_{cru}(s'))ds'} \\ &= I_0 e^{-\int_0^s \mu_{fur}(s')ds'} e^{-\int_0^s \mu_{cru}(s')ds'} \end{aligned} \qquad \text{Eq. 23}$$

As stated above, it was not possible to measure the integrals corresponding to the furnace for all z translational positions, preventing CT reconstruction. However, because the crucible was small enough, all the necessary integrals were measured, but superimposed with those from the furnace. Obtaining them involved dividing the sinogram obtained with the furnace and crucible by that obtained with the furnace alone. This could be achieved by performing an

independent measurement of the empty furnace sinogram. This procedure is illustrated by Figure 3.18.

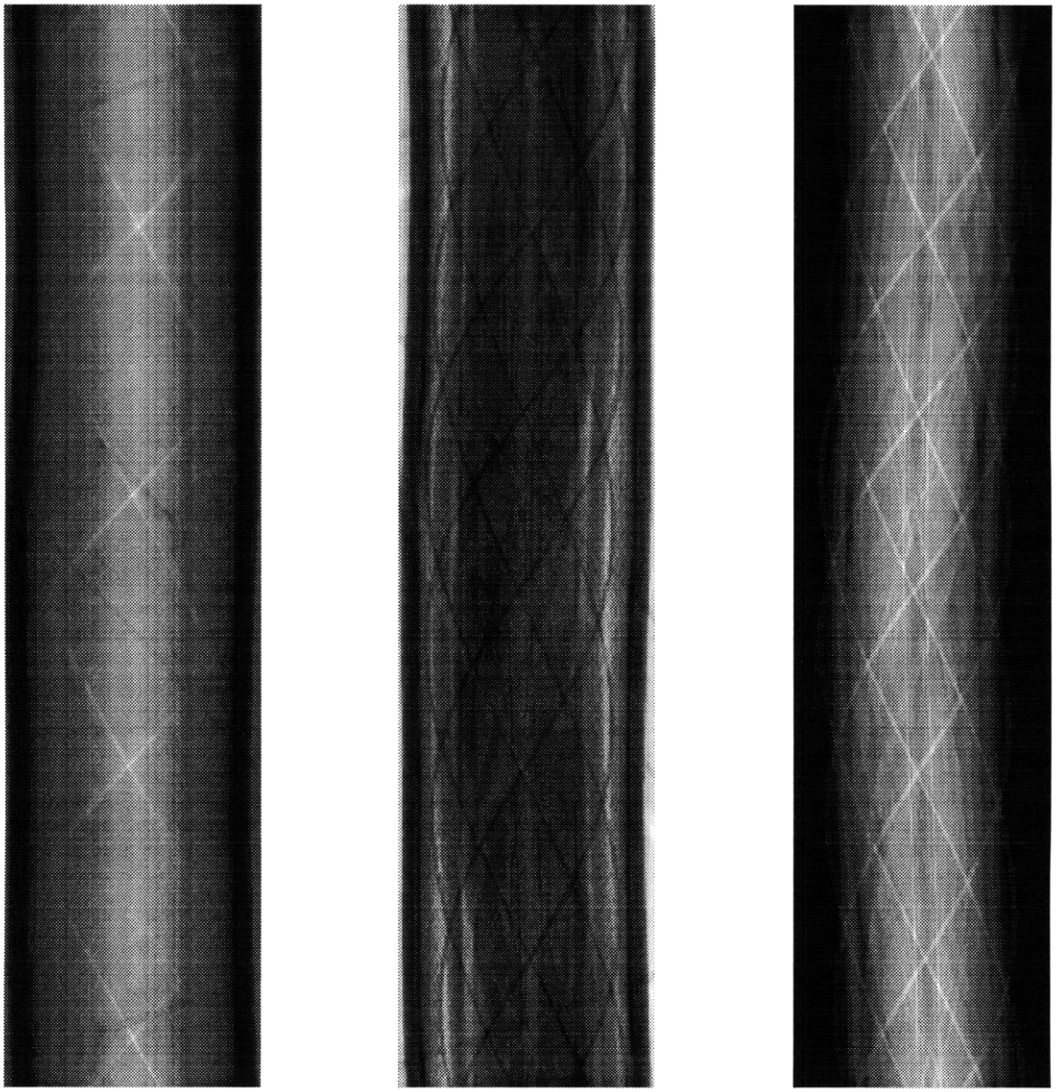

a. Empty furnace b. Furnace and crucible c. Crucible alone

Figure 3.18. Sinogram measured with the empty furnace (a), the furnace and the crucible (b), and their ratio(c).

A typical solidification experiment proceeded as follows:

- The empty furnace was heated to the desired temperature.
- Its sinogram was measured.
- The crucible, filled with aluminum, was placed within it.

- After the aluminum was melted, the cooling tube and thermocouples were inserted.
- The furnace was turned off, and cooling was turned on.
- Images were obtained continuously during the solidification process.

A series of images were obtained every minute. Each image shows the density map of the crucible and its contents averaged over two minutes.

3.6.2. Results

A typical CT image of the aluminum solidification front is shown in Figure 3.20a. Because of the low contrast between solid and liquid aluminum, the solidification front was difficult to recognize. To accentuate it, we subtracted an image of completely liquid aluminum from an image of partially solidified aluminum. The resulting difference image showed the changes in density between the two snapshots, i.e. the solid zone. Such an image is shown in Figure 3.20b. A diagram also illustrates the features visible in these images (Figure 3.19).

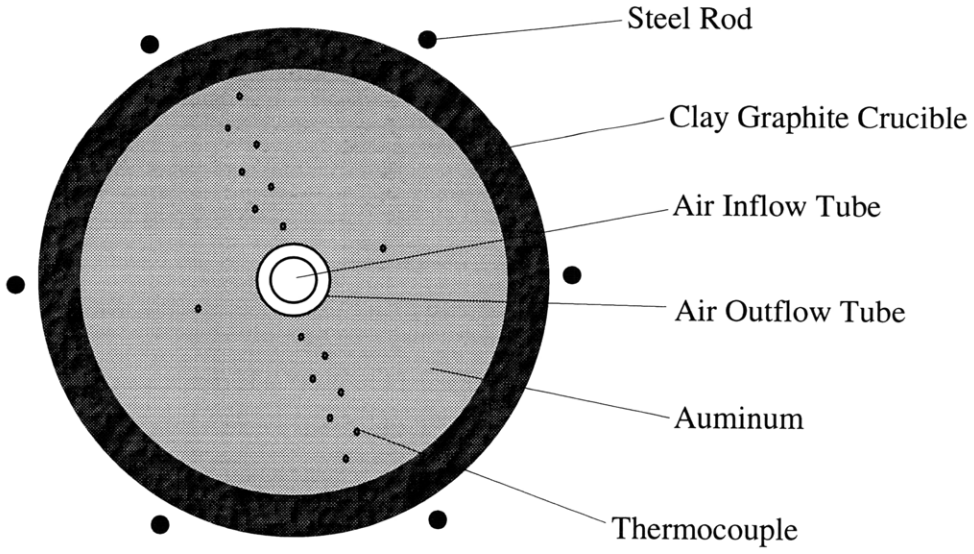

Figure 3.19. Schematic of features shown in the aluminum solidification CT images.

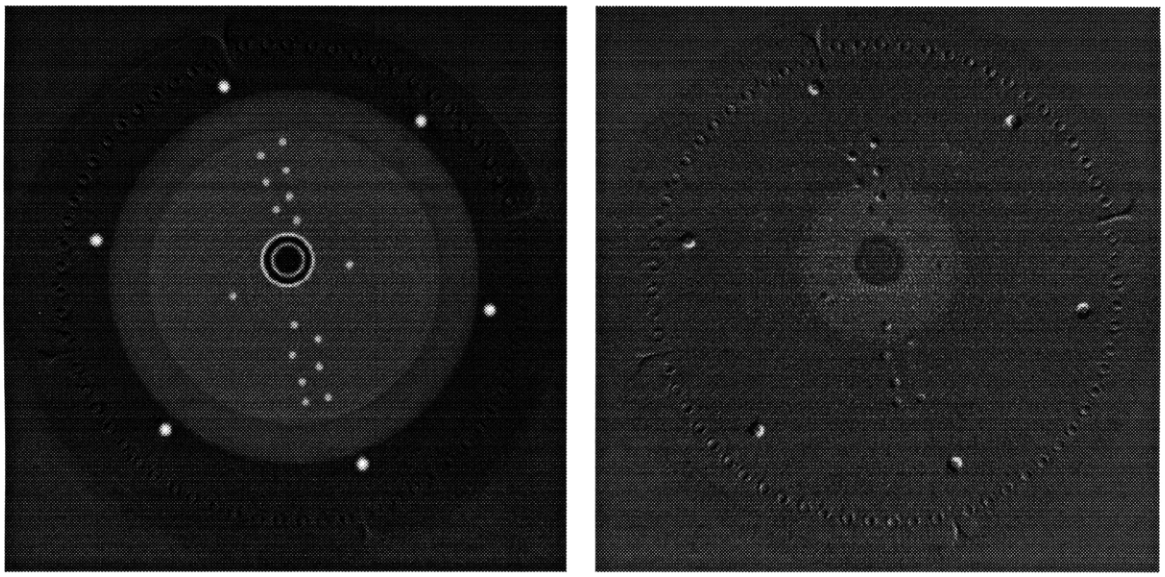

a. b.

Figure 3.20. Images of partially solidified aluminum on an absolute scale (a), and difference image (b).

3.7. Other examples

Figure 3.21 shows a number of images obtained using the CastScan CT sensor.

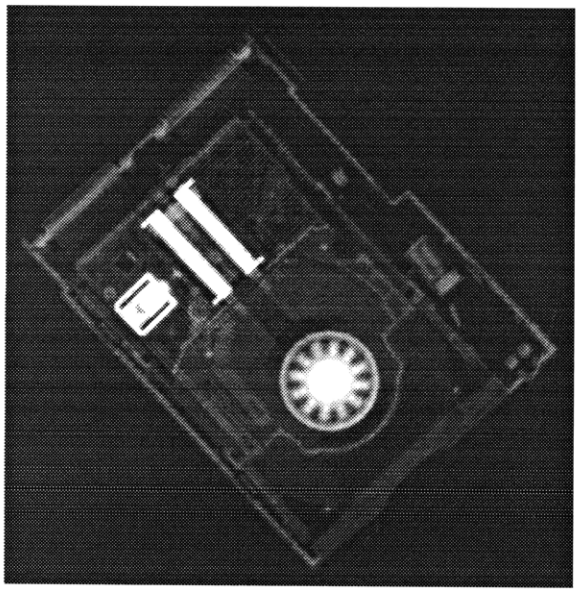

a. Iomega Zip ® drive.

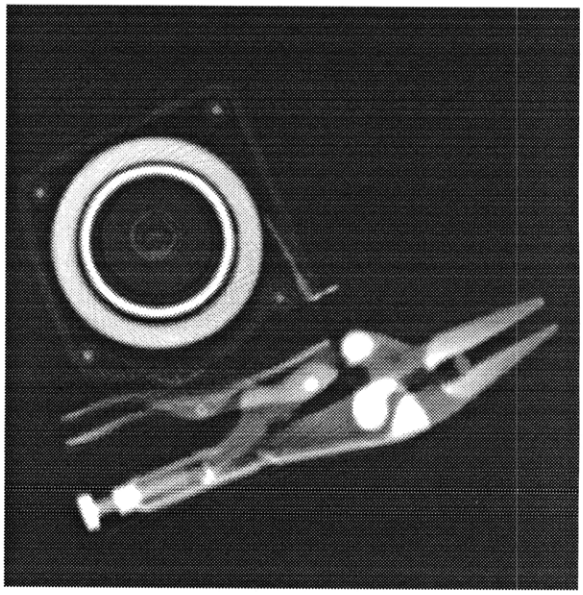

b. Measuring tape and pliers.

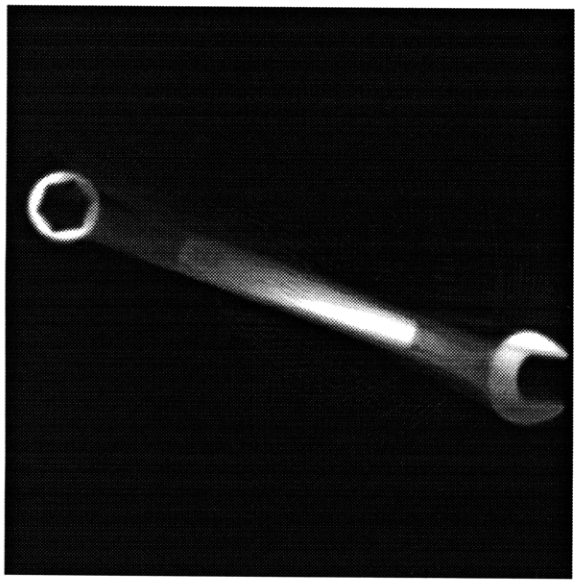

c. Wrench.

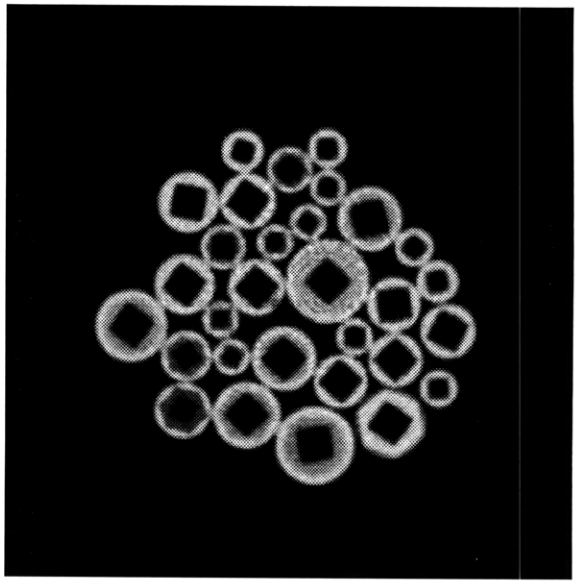

d. Collection of sockets.

Figure 3.21. Examples of CT images.

3.8. Discussion and Future Improvements

We will first compare the expected performance parameters with the measured ones. An analysis of the discrepancies between the two will follow. Solutions to the encountered problems will be discussed. Finally, we will examine potential future improvements to this system.

3.8.1. Expected vs. Actual Performance

The important performance characteristics of a CT system are planar resolution, slice thickness, sensitivity and time resolution. Table 3.1 summarizes their expected value, along with their measured value.

	Expected	Measured
Planar resolution	1.35 mm	1.6 mm
Slice thickness	12 mm	4.5 mm
Sensitivity	1%	1.5%
Time resolution	17 sec	2 min

Table 3.1. Expected vs. measured performance parameters.

The measured resolution was slightly worse than the expected value. The expected value corresponds to the best resolution attainable with a CT system having the geometrical properties of the CastScan machine. The calculation assumed an infinite data acquisition time, so that photon statistical noise was not an issue. It also ignored other sources of noise, such as source variability and electronic noise. Given this idealization, achieving a resolution of 1.6 mm was a good result.

The measured slice thickness was less than expected. This may be due to imprecision in the manufacture and assembly of the linac beam collimator. Very small variations in the collimation geometry close to the source can lead to substantial changes in the CT slice

thickness. Because slice thickness was not a critical issue in the design of this system, the vertical collimation system was not carefully calibrated. It must also noted that the system's response to features at various vertical displacement from the beam center was not a square function. The 4.5 mm slice thickness value is a measure of how thick the slice would be if the response was uniform and had a sharp cutoff. In reality, the response was more spread out, although no attempt was made to quantify the vertical response profile.

The sensitivity of 1.5% was slightly worse than expected, but was well below the threshold needed to image the aluminum solidification front. One must keep in mind that sensitivity calculations only accounted for photon statistical noise, and other sources of noise were not accounted for. In the laboratory, source intensity fluctuations and electronic noise contributed to worsening the sensitivity.

One performance goal was not achieved by the CastScan system in its current form. The time resolution was about seven times worse than expected. This was due to two main factors. Firstly, achieving the necessary spatial resolution required using a two-rotation data acquisition method. This method doubled the time needed for data acquisition, and added a substantial time overhead. Secondly, it was found that the rotary stage could not be operated at a rotation rate faster than 8°/s with the furnace placed on it. The combination of these two factors imposed a data acquisition time of two minutes. As we will discuss in the following section, using a faster rotary stage could substantially reduce the data acquisition time without reducing the image quality.

3.8.2. Future Improvements

The most obvious improvement to this system is to replace the current rotary stage with a faster one. As mentioned earlier, the current data acquisition algorithm involves acquiring 8100 angular views, averaged down to 2700 to reduce source noise. We estimated in section 3.5.3 that 765 views would be sufficient to maintain planar resolution without undersampling artifacts. In reality, that number could probably be lower. To illustrate this fact, two images were reconstructed, one using all the available views (2700), and the other one with one fourth of them (675). The images are shown in Figure 3.22a-b, along with the

difference between the two(c). The images were qualitatively identical. The difference image showed that no artifacts were present in the second image, and that reconstructing the image with four times less data did not produce coherent noise. The noise level did increase somewhat however. Measuring the fractional standard deviation in both images in an ROI of constant density showed that the noise level increased by 15%. This is a small sacrifice to pay for an image data acquisition time reduced from 2 minutes to 30 seconds.

a. CT image with 2700 views.

c. CT image with 675 views.

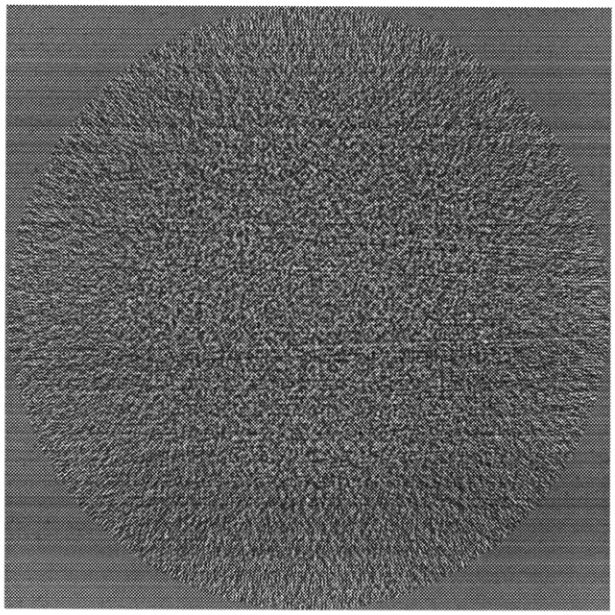

c. Difference between (a) and (b).

Figure 3.22. CT image reconstructed with 2700 views (a), 675 views (b), and the difference (c).

Although data was collected over 8100 views, it needed to be averaged down to 2700 views to reduce the effect of the intensity fluctuations of the source. Because it was designed for radiography, pulse-to-pulse variations were not critical for the MINAC-6 linac. Retrofitting it with a more stable power supply could remove the remove the need to average

the data. Another factor of three would then be gained in data acquisition time, reducing it down to about 10 seconds.

If it proved to be a priority, slice thickness could also be reduced with a minimal re-design of the CastScan system. As stated earlier, the detector system was designed for medical use and had an efficiency of about 5%. Using thicker crystals could improve this efficiency by an order of magnitude. Slice thickness could then be reduced without deteriorating the photon noise statistics. A slice thickness of 1 mm should be readily attainable.

If future needs dictated an improvement in the system's resolution, modifications would be more drastic. As mentioned in section 1.2.3, a CT system's best resolution can roughly be calculated using Eq. 5. Improving the system's resolution involves reducing the source's spot size, the detector width, or both. Reducing a single parameter could be sufficient, but the system's compactness would suffer. The only way to obtain both an improved resolution and to maintain a small system size is to reduce both at the same time. Linear accelerators are available with smaller spot sizes today, however their intensity can be expected to be lower than the MINAC-6 linac's. The lower intensity will result in worse photon statistics. Longer acquisition time could compensate for this effect. Smaller detectors could also be used. It is important to remember that the size of the detector collimation is not dependent on the detector width, but on the photon energy. If the energy is not lowered, smaller detectors will imply a reduced geometric efficiency. This will increase the data acquisition time. The data acquisition procedure may also find itself complicated. Indeed, object or detector translations will be necessary to avoid translational undersampling artifacts, as discussed in section 3.5.3.

While many improvements can be achieved without drastically modifying the CastScan system and its parameters, resolution improvements would require a complete re-design. As the discussion above shows, resolution comes at a heavy price. It is the most important factor in designing a new CT system. Resolution should be sufficient to achieve the project goals, but an over-design could result in technical and cost problems.

As we have discussed above, the results obtained with the CastScan system using conventional computed tomography show promise for further study of the solidification

phenomenon in metals in the laboratory. Experiments were performed in our laboratory to examine how pure aluminum and some of its copper alloys solidified, and are described in [24]. However, the operating conditions in a metal casting plant may not allow for the installation of a CT system requiring data gathered over 360°. In the following chapter, we depart from the traditional concepts of CT and we examine methods of extracting valuable information about metal casts using x-ray attenuation data obtained over a limited angular range.

4. LIQUID/SOLID DISCRIMINATION FROM TRANSLATE-ONLY DATA

So far, we have discussed a conventional computed tomographical solution to the problem of the identification of the solidification front in metals. The system described in the last two chapters can be used as a research tool to study the phenomenon of solidification in pure metals or alloys. However, it cannot be used in its present form as a sensor in a commercial casting plant. Some of the challenges that must be overcome to adapt it to the industrial environment are the following:

- The system must be able to operate in a rough environment,
- radiation shielding must be adapted to the plant layout and limits,
- the source and detectors must rotate all around the cast.

The last point refers to the fact that the geometry of many commercial casters does not leave enough room for a CT system to perform a 360° rotation. In fact, many commercial casters are arranged such that several casts are placed side-by-side.

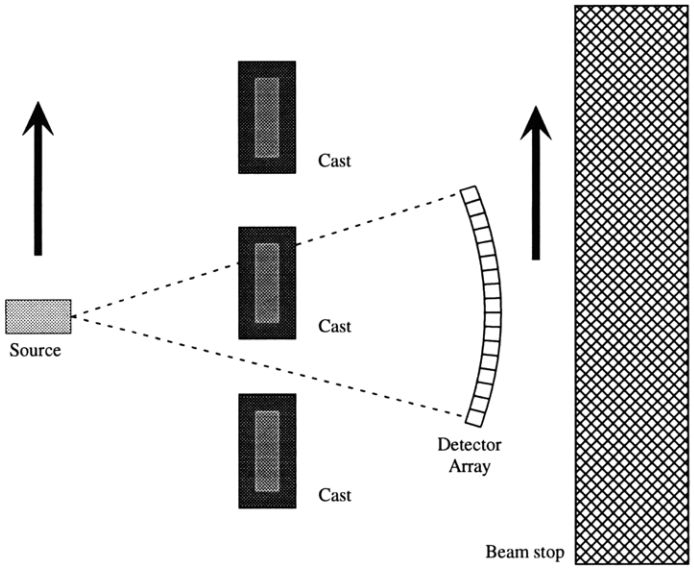

Figure 4.1. Schematic of a translate-only tomography system.

An advantageous source-detector configuration is shown in Figure 4.1. In this geometry, the source and detectors are moved together along the cast, or casts, in a translate-only mode. This approach is attractive in a number of ways:

- data acquisition is rapid because no rotation is required;
- the motion system is simpler and cheaper;
- shielding is required only on one side.

Unfortunately, attenuation measurements are obtained over a limited angular range, equal to the source's fan angle. In section 4.1, we will review previous solutions to such limited-angle problems, and we will examine their applicability to this situation. We will then present a translate-only experiment performed in the laboratory using the equipment built for the conventional CT system described earlier. We will explore possible solutions to imaging a cast-like object. Finally, we will discuss practical implementation issues of a translate-only tomographic system.

4.1. Review of Possible Approaches

The problem described above involves the reconstruction of the density distribution in an object cross-section using a data set limited in angular range. Tomographical reconstruction using such data is referred to as *limited-angle tomography*. Because of its potential applications in the fields of medical imaging, sonar, radar, atmospheric measurements, etc., research in this area has been extensive, and many algorithms have been developed.

Reeds and Shepp [25] present an algorithm based on "squashing" the image function of the object. They estimate that high-quality reconstructions could be achieved with 160° of angular data, and could probably be attained with only 140°. Other algorithms rely on completing the missing portion of the sinogram based on its consistency, its smoothness and its noise properties [26]. Unfortunately, the quality of the image reconstruction is typically poor. Other algorithms rely on iterative techniques to complete the sinogram [27][28]. In general, it can be stated that the feasibility of limited-angle reconstruction is highly dependent

on the noise present in the sinogram. The less angular information is available, the less noise can be tolerated. There are no algorithms available that are practical for a system such as the proposed one, where attenuation data is available for a very limited angular range.

Another approach is that of *laminography* [29][30][31][32][33][34]. This modality allows the reconstruction of the density maps in different layers of an object. The experimental setup of laminography is shown in Figure 4.2.

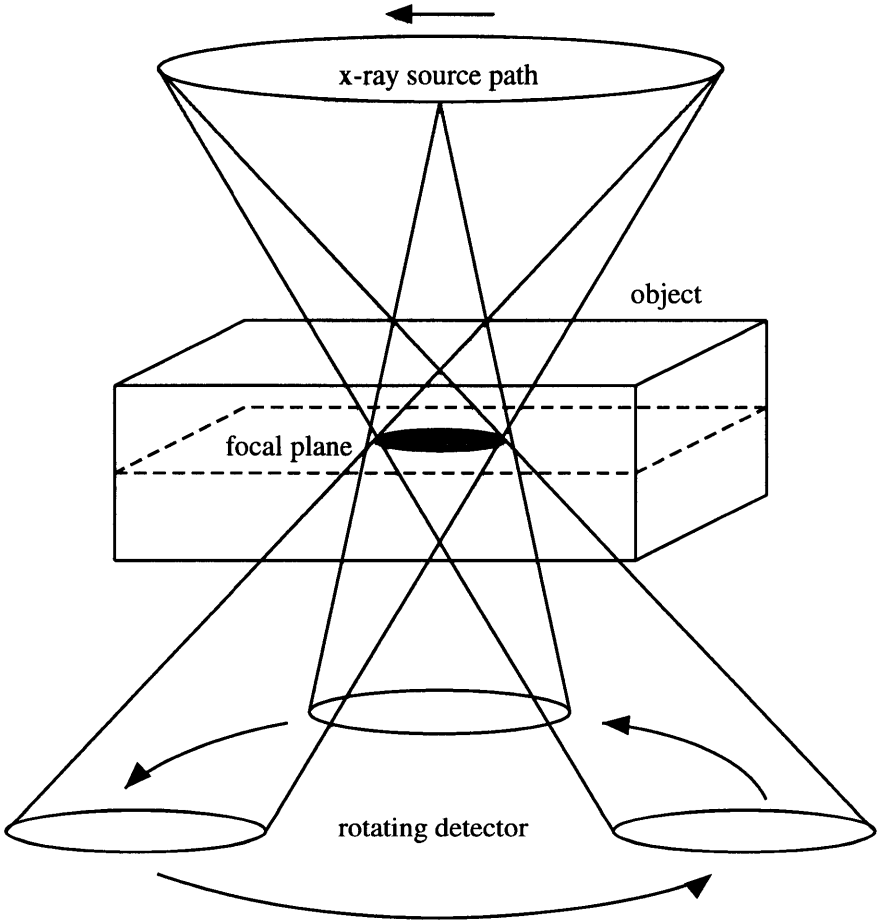

Figure 4.2. Diagram of a laminography experiment.

An x-ray source and a detector array rotate in a circular path. As can be seen in the figure, this geometry defines a focal plane in the imaged object. Points in this plane will be projected in the same position on the detector array throughout the rotation, whereas points in adjacent planes will be projected on a circle on a circular path. The radius of this circle is proportional to the distance between the plane under consideration and the focal plane.

Consequently, the attenuation data from planes other than the focal plane is blurred, and an image of the focal plane is formed. This method is essentially a backprojection technique, and suffers from the same artifacts as one would encounter using backprojection from a limited-angle data set, i.e. blurring in the unsampled dimensions. As a result, the plane-to-plane resolution in this technique is quite poor.

The techniques described above are general reconstruction techniques in the sense that they do not use *a priori* knowledge about the object being imaged. In the situation we are interested in, many features are known, such as:

- the physical boundaries of the object,
- the density limits of the object,
- the binary nature of the object (i.e. solid/liquid, to a first approximation) ,
- the basic geometry of the object (i.e. roughly rectangular melt zone).

We will now present an experiment in which a projection data set for a cast-like object was obtained. We will then present a number of different approaches to locating its melt-like zone.

4.2. Translate-Only Imaging Experiment

An experiment was conducted to investigate the issues involved in the image reconstruction of a cast using a translate-only data set. The experimental setup will be described in section 4.2.1. Subsequent sections focus on a variety of methods to calculate the geometry of the object from the limited data set obtained.

4.2.1. Experimental Setup

A typical industrial metal cast has a rectangular exterior cross-section. The metal is separated into two phases, with a solid outer skin and a roughly rectangular inner liquid zone. To model such an object in the laboratory, a rectangular aluminum block, shown in Figure 4.3, was machined. It was previously described in section 3.2. The block was 127mm long

and 62 mm wide. A low density region was present inside, with a rectangular shape 108 mm long by 57 mm wide. The low density region was created using the partial volume of a 0.05 mm thick air cavity, and its effective density was 11% lower than the rest of the block. The inner rectangle corresponds to the liquid area of a metal cast, whereas the outside represents the solid zone. Although the system was capable of measuring attenuation data through larger cross sections, the block was kept small in order to allow standard CT imaging.

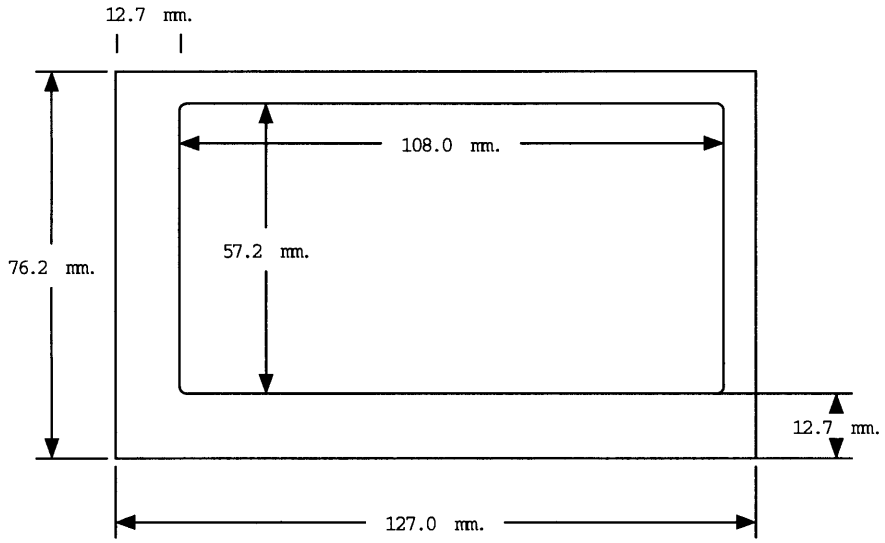

Figure 4.3. Diagram of an aluminum block with a 0.5 mm rectangular depression.

The block was placed at the center of rotation of the system, and a tomogram was obtained, shown in Figure 3.10. It was then translated through the beam, as illustrated by Figure 4.4.

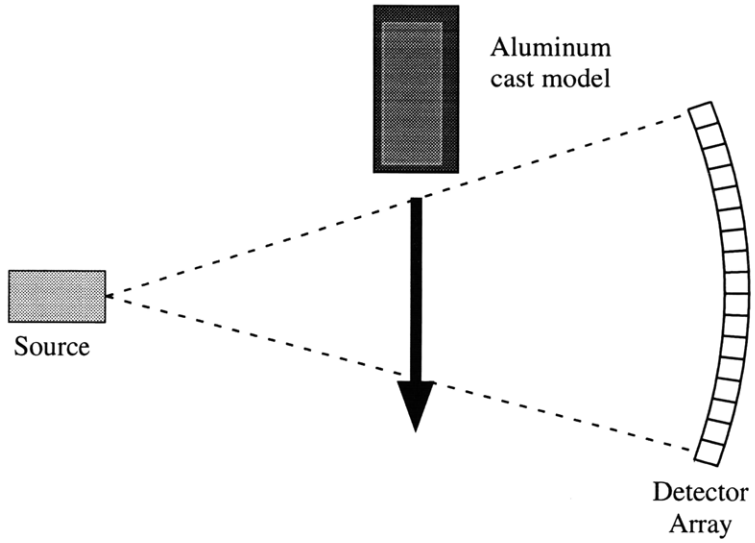

Figure 4.4. Diagram of the laboratory-scale translate-only experiment.

Attenuation data was measured 60 times per second for a period of 68 seconds during which the block was continuously translated through the beam. Attenuation measurements were performed by all 128 detectors at 4096 translational steps of 0.134 mm each. The angular range of the measurements was 32°. The resulting data set is shown in Figure 4.5.

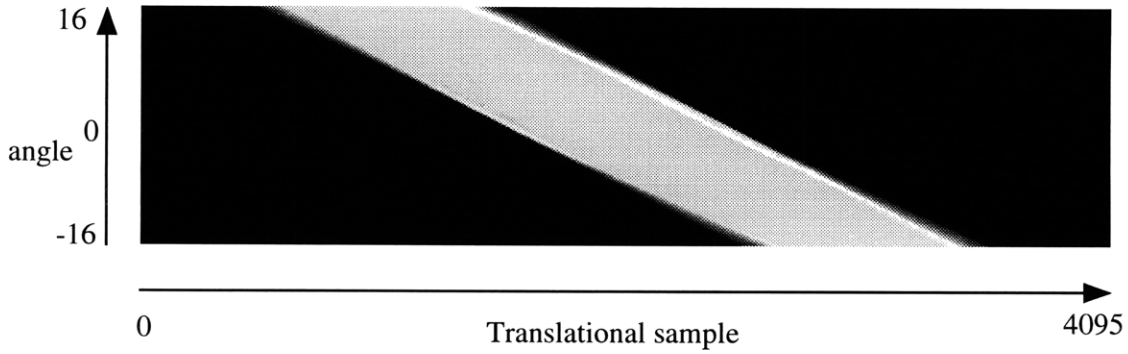

Figure 4.5. Attenuation data of cast model in translate mode.

Plotting the curve corresponding to the density integral at 0° can help understand the data presented above. The plot is shown in Figure 4.6.

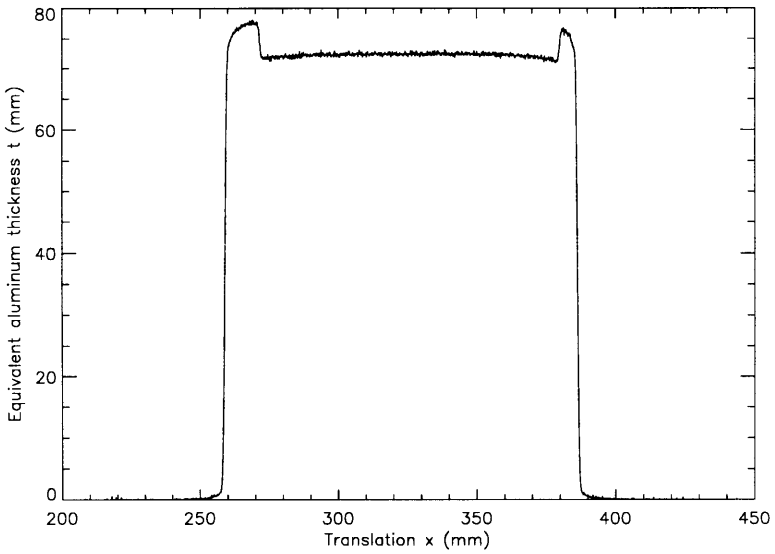

Figure 4.6. Measured aluminum equivalent thickness of the cast model at 0°.

The vertical axis of the plot shows the measured aluminum equivalent thickness t of the sample. This represents the measured aluminum thickness if the sample were entirely solid. The horizontal axis is the distance x by which the block was translated. The low-density area can be identified as the region of constant lower equivalent aluminum thickness in the middle of the plot. The edges represent the high-density (i.e. solid) part of the block. This plot can be used to measure the solid wall thickness on either side of the liquid area in the direction of translation. The situation becomes more complicated when one plots the thickness at angles different than zero. However, such measurements contain the information necessary to identify the location of the melt-like zone. The methods described in the following section attempt to extract this information in different ways and with various degrees of success.

4.2.2. Laminographic Reconstruction

As explained earlier, image reconstruction via laminography relies on the backprojection of the data such that a single plane is in focus. Figure 4.7 helps to understand how this principle can be applied to our situation:

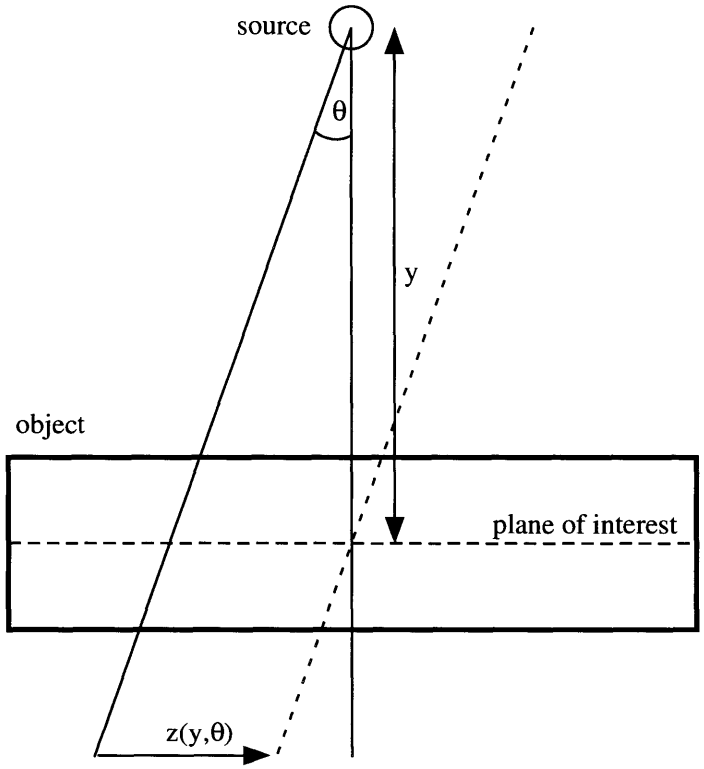

Figure 4.7. Geometry of a translate-only experiment in the context of laminography.

Consider the ray originating from the source at an angle θ from the beam axis. Photons are emitted from the source, transmitted through the block, and detected on the other side. This measurement yields the integral p of the aluminum density along the ray in question:

$$p(x,\theta) = \int\int \rho(x', y') \cdot \delta(x' - x + y' \tan\theta) dx' dy' \qquad \text{Eq. 24}$$

To reconstruct the density distribution in a given plane of interest, or focal plane, backprojection must be performed in such a way that the rays corresponding to a given point on that plane intersect. Figure 4.7 shows a ray at an angle θ as well as the central ray. If the latter is used as a reference, one must backproject the ray corresponding to a relative translation z such that:

$$z(y,\theta) = y\tan\theta \qquad \text{Eq. 25}$$

In this equation, y is the distance between the source and the focal plane, θ is the angle between the backprojected ray and the center ray, and z is the translation distance between the two rays. An image of the focal plane is reconstructed using the following equation:

$$i(x,y) = \frac{1}{\theta_{\max} - \theta_{\min}} \cdot \int_{\theta_{\min}}^{\theta_{\max}} p(x',\theta)\,d\theta \qquad \text{Eq. 26}$$

where

$$x' = x - y\tan\theta \qquad \text{Eq. 27}$$

θ_{max} and θ_{min} are the maximum and minimum projection angles available, and p is the projection data obtained at a translation x' and an angle θ. The transformation from $p(x,\theta)$ to $p(x',\theta)$ is illustrated in Figure 4.8 for a focal plane at y = 50cm from the source.

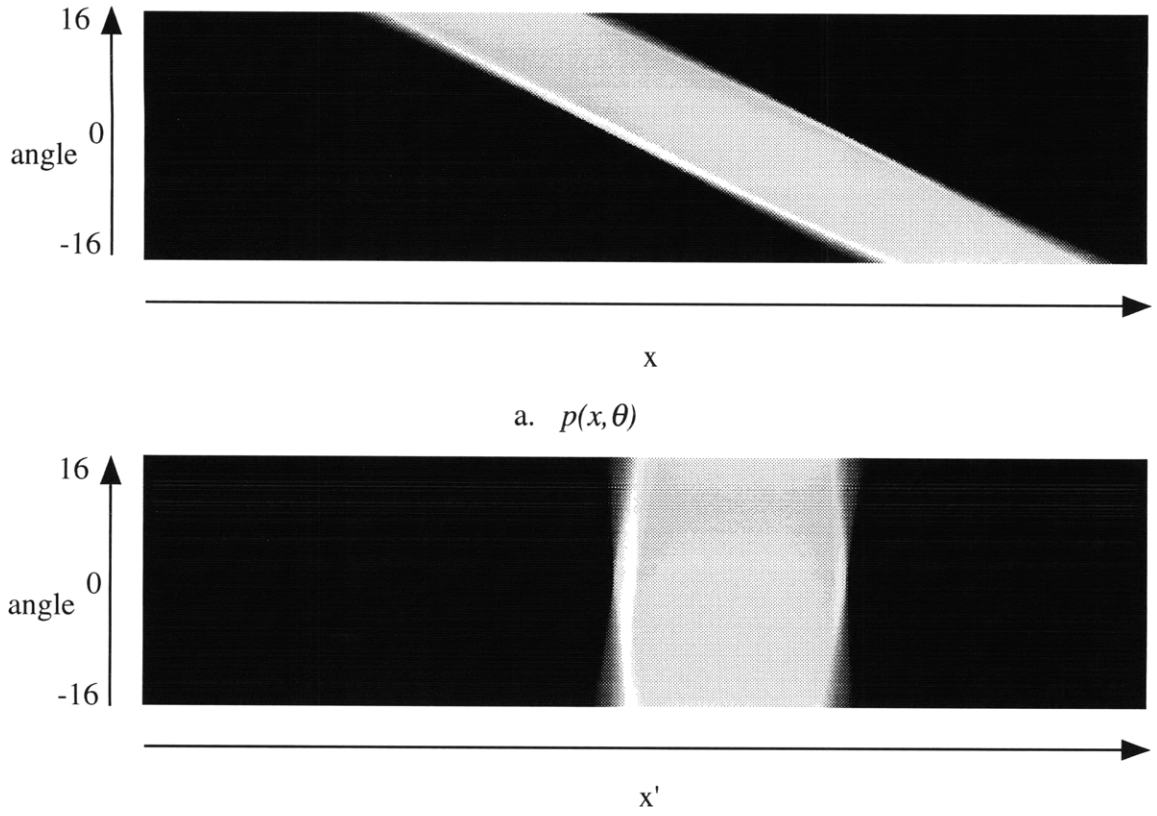

Figure 4.8. Original projection data (a) and transformed projection (b) for a focal plane at 50 cm from the source.

Once the transformation described in Eq. 27 is made, a summation over θ is performed. This operation can be repeated for several focal planes in order to obtain a complete image. The result is shown in Figure 4.9.

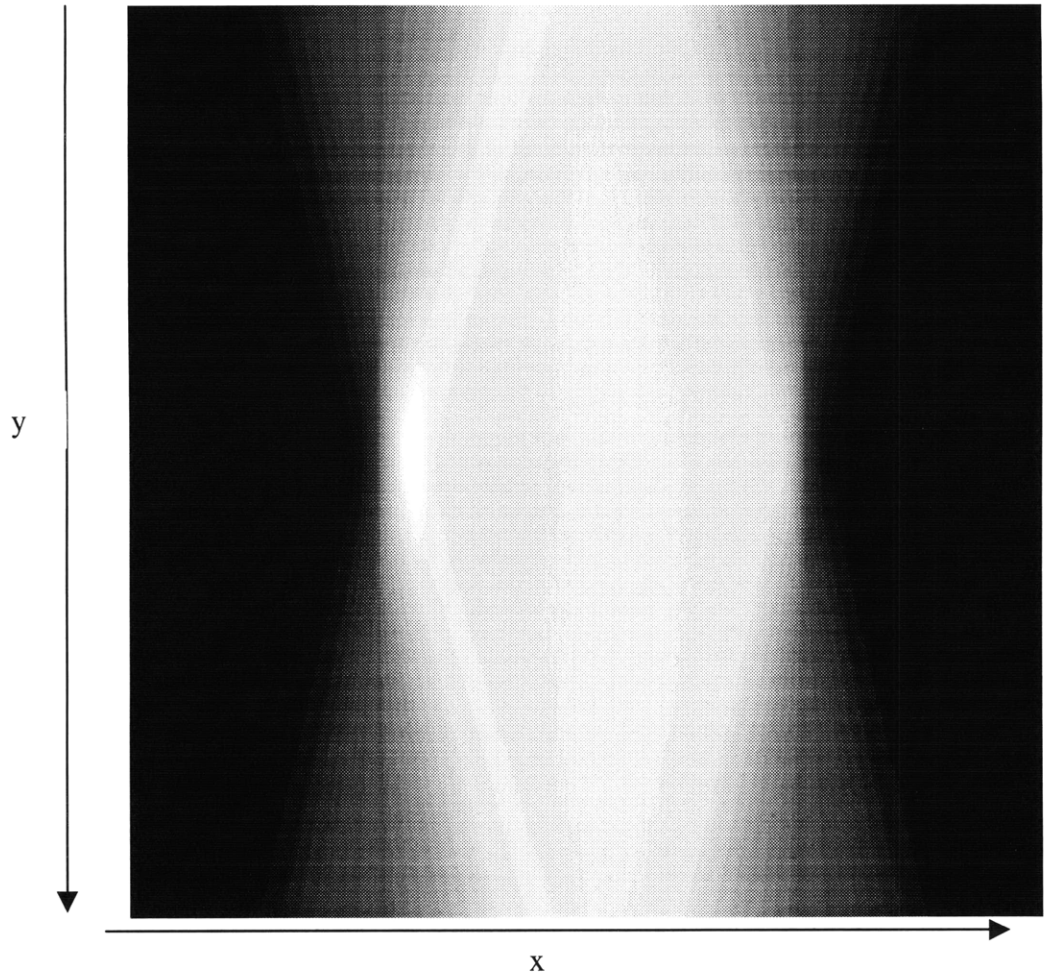

Figure 4.9. Image of the cast-like aluminum block reconstructed using laminography.

This image shows that on the translational axis (x), the block's edges could be clearly discerned. The edges of the low-density area could also been noticed. The edge was thicker on the left than on the right. However, because the resolution on the beam axis (y) is so poor, the other edges could not be located.

Laminography is well suited to detect high-contrast, localized features in an object. In this application however, the feature to detect had a low contrast and was large in extent. In addition, the small angular range available for attenuation measurements contributed to the poor resolution along the beam axis. For these reasons, it is apparent that laminography is not a suitable solution for this application.

4.2.3. Iterative Reconstruction Method

Iterative image reconstruction techniques assume a two-dimensional density distribution $o(,x,y)$ through which a number of line integrals are experimentally measured. Each measurement is labeled p_j, where j is corresponds a particular ray, without reference to an angle or a translation distance. Reconstruction is performed using the following process:

1. Start with an initial estimate of the density distribution, $i(x,y)$.
2. Calculate the line integrals p'_j though $i(x,y)$ corresponding to the measurements p_j.
3. Compare p'_j and p_j.
4. Modify $i(x,y)$.
5. Restart from step 2.

There exist many possible implementations of this algorithm. One is free to choose how to perform steps 3 and 4, and whether to perform them for a single j and return to step 2, or to perform them for all j at once.

A number of techniques were attempted for the reconstruction of the cast-like block. We will focus on the most successful one. The algorithm was the following:

1. Start with a uniform density distribution of 0 g/cm^3.
2. Calculate p'_j for all j by p.
3. Calculate the difference $d_j = p_j - p'_j$ for all j.
4. For each point (x,y), calculate the sum $s(x,y)$ of all d_j for all rays that intersect it.
5. Add $w \cdot s(x, y)$ to $i(x,y)$, where $w(x,y)$ is a normalization factor.
6. Restart from step 2.

Because this algorithm was very computer-intensive, the number of rays j for which integrals were calculated was reduced by a factor of 16 by averaging over the translational axis. Figure 4.10 shows the calculated distribution $i(x,y)$ after 1, 5, 10, 20, 50 and 100 iterations.

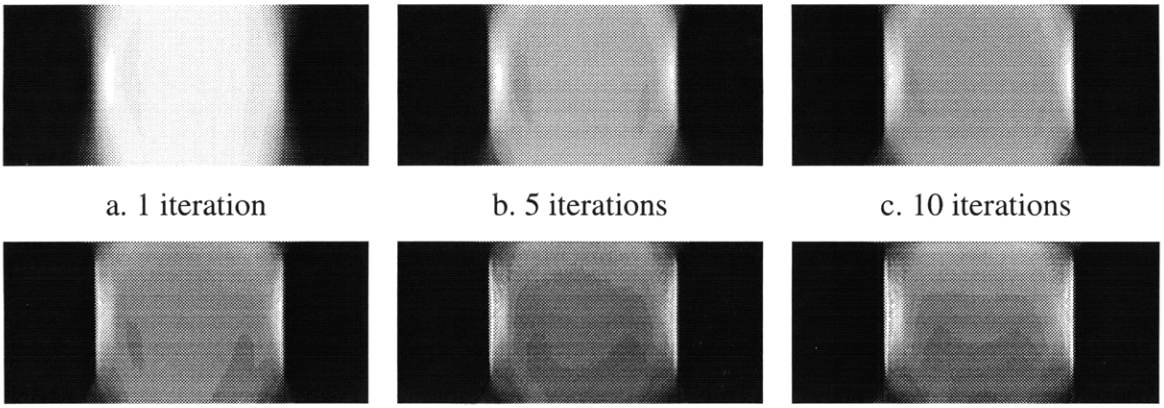

a. 1 iteration b. 5 iterations c. 10 iterations

d. 20 iterations e. 50 iterations f. 100 iterations

Figure 4.10. Iterative reconstruction images of the cast-like aluminum block.

The first iteration was essentially a backprojection, so that one expected a very blurry image. After five iterations, one could already distinguish the edges perpendicular to the translational axis. The low-density area was also visible on that axis. Features on the beam axis were still blurred. Further iterations did not significantly improve the image quality. After 100 iterations, the process showed a tendency to converge toward a special solution that did not correspond the correct distribution.

This poor result was due to the small angular range of available projection data. As is shown in Figure 4.11, projections through the central area of the block all yield the same integral value, and so contribute no new information although statistical noise is reduced.

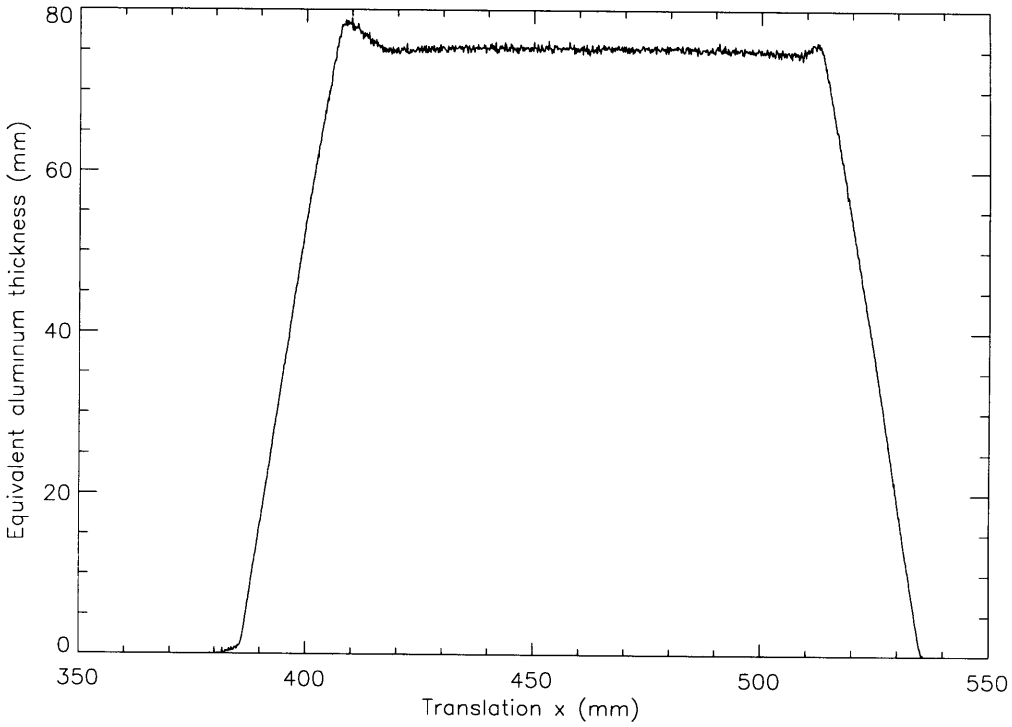

Figure 4.11. Measured aluminum equivalent thickness of the cast model at 16°.

In essence, all the information relating to the position of the low-density area along the beam axis was located in the few projections going through the edges of the object. To distinguish features on the beam axis and at the center of the block, the algorithm requires a good knowledge of the distribution further away from the center. This technique could work with noiseless data. Unfortunately, noise in the measurements reduced the quality of the reconstruction at the edges. Its cumulative effect from iteration to iteration steered the algorithm toward a special solution rather than towards the real density distribution.

In the iterative technique, each point in the reconstructed image is a degree of freedom, and too many solutions give a projection set close to the measured one to allow one to distinguish the correct one, given the noise level. If one were to reduce the number of degrees of freedom sufficiently, a simplified model might fit the data. This is the topic of the next section.

4.2.4. Model Optimization Method

We stated earlier that the melt zone inside a cast is roughly rectangular in shape. In this section, we will examine how to model the object as a low-density rectangular zone inside a higher density rectangle, and we will present the results obtained after fitting the measured data to this model.

First, it is important to obtain an analytical model of the projection data though a rectangular object. A diagram of this situation is shown in Figure 4.12.

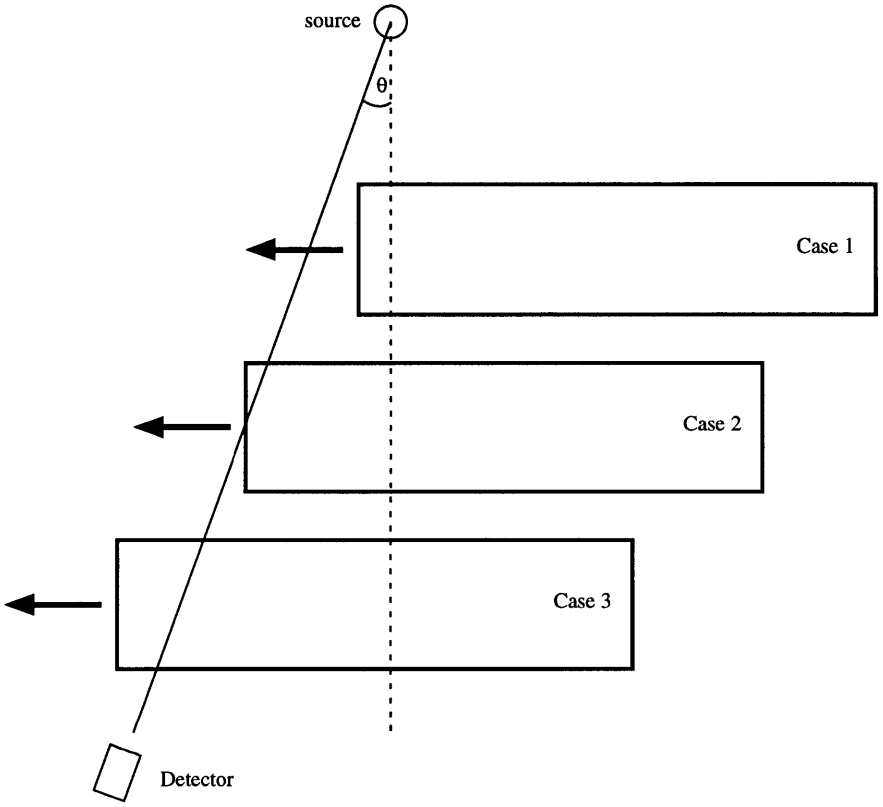

Figure 4.12. Rectangular object passing though a ray.

The process of a rectangular object traversing a ray can be divided into three special cases. In case 1, the ray does not intersect the object, and its integral is equal to zero. Eventually, the top left corner reaches the ray, and the integral increases linearly until the bottom corner is reached. This is the situation described in case 2. Finally, once the bottom

corner is cleared in case 3, the integral becomes constant. Figure 4.13a shows an idealized plot of the integral $p(x,\theta)$.

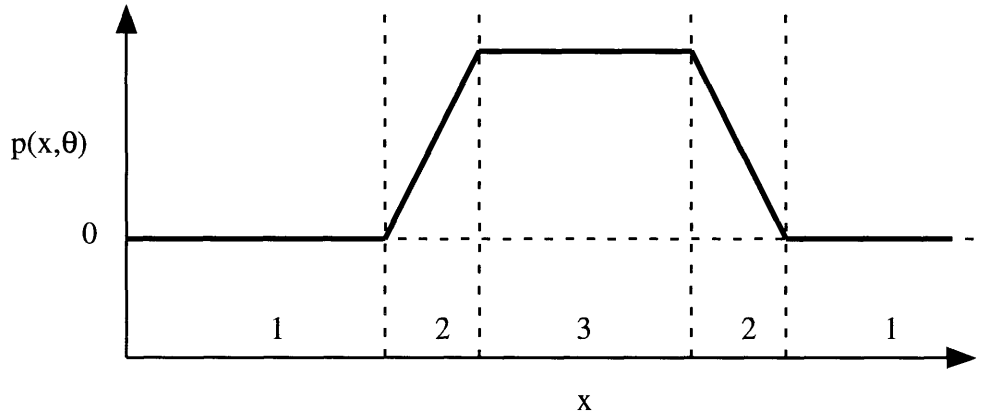

Figure 4.13. Plot of the ideal density integral $p(x,\theta)$ as a function of the translation x.

Locating the position of the slope change for each angle is crucial in determining the position of the rectangle from a measured data set. Let z be the closest distance between the source and the corner of interest. The position x' of the slope change corresponding to that corner is given by:

$$x' = x_{offset} + z\tan\theta \qquad \text{Eq. 28}$$

where x_{offset} is a constant and corresponds to the position of the corner at 0°. By fitting the experimentally measured $x'(\theta)$ to Eq. 28, one can obtain both x_{offset} and z, and therefore completely determine the location of the corner in question. If the data were ideal, the x-positions of the two left corners would be equal, as well as those of the right corners. The z-positions should also be self-consistent.

Although this method functions for a rectangle-shaped object, we are specifically interested in a rectangle-within-a-rectangle configuration. If one could separate the problem of locating the geometry of the outer limit of the block from that of locating the shape of the low-density area, this method could be used. This can be achieved by measuring the

projection data $p(x,\theta)$ of a solid block of aluminum with the same external dimensions as the cast-like block. Let p_{solid} be the projection data set obtained from an entirely solid block, $p_{composite}$ be that the two-density block, and $\Delta\rho$ be density difference between the solid and liquid area. One can calculate the difference between the two data sets:

$$p_{liquid} = p_{solid} - p_{composite} \qquad \text{Eq. 29}$$

The remainder, labeled p_{liquid}, is equal to the integral of the density difference $\Delta\rho$ along the ray defined by the translation distance x and the angle θ. If the algorithm described above is applied to both $p_{solid}(x,y)$ and $p_{liquid}(x,y)$, the geometry of both the outer solid edge and the inner liquid area can be determined.

As stated above, the first step in this process was to measure p_{solid} and $p_{composite}$, and then to calculate the difference between the two. These data sets are shown in Figure 4.14.

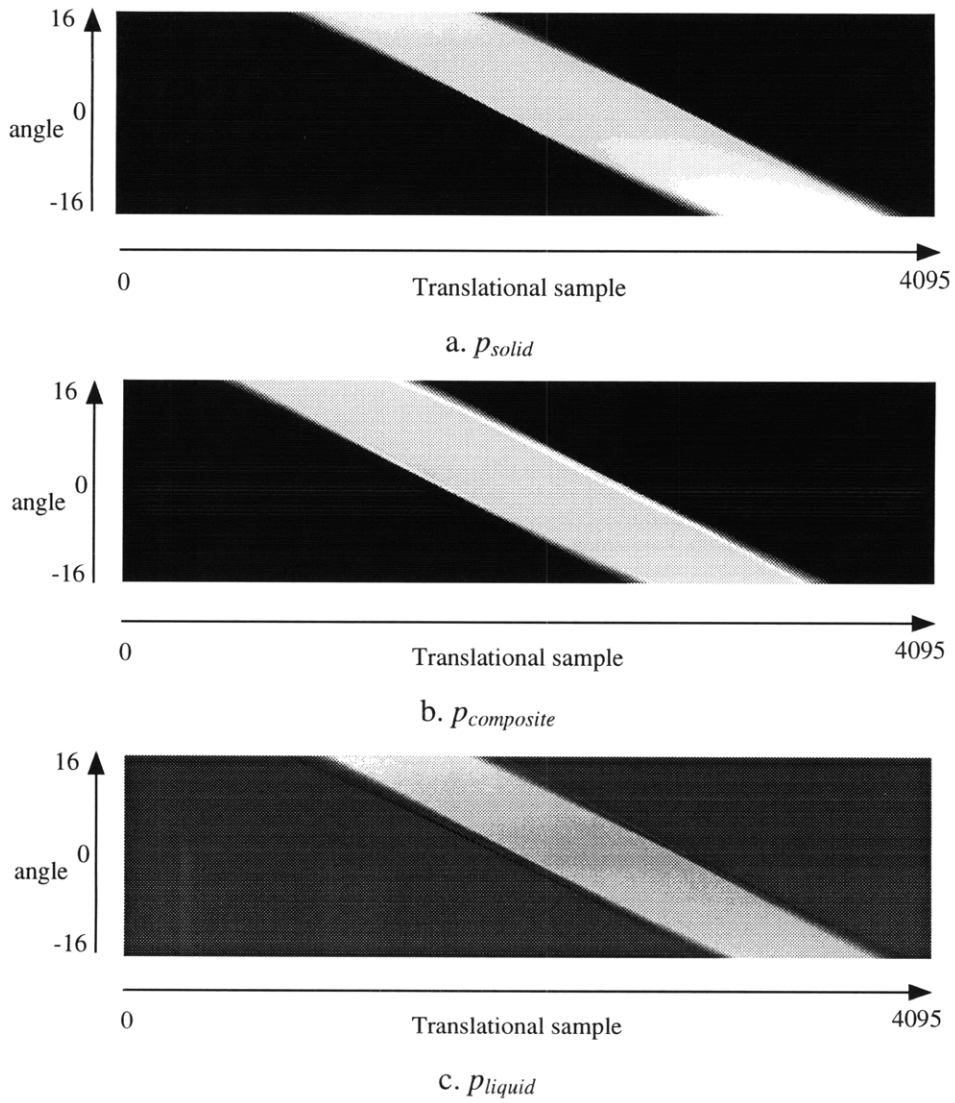

Figure 4.14. Projection sets through a solid aluminum block (a), a composite block (b) and the difference (c).

To determine the translational position x' of each corner for a given angle θ, the profile was fitted to a trapezoid shape using least-squares linear regression, as shown in Figure 4.15.

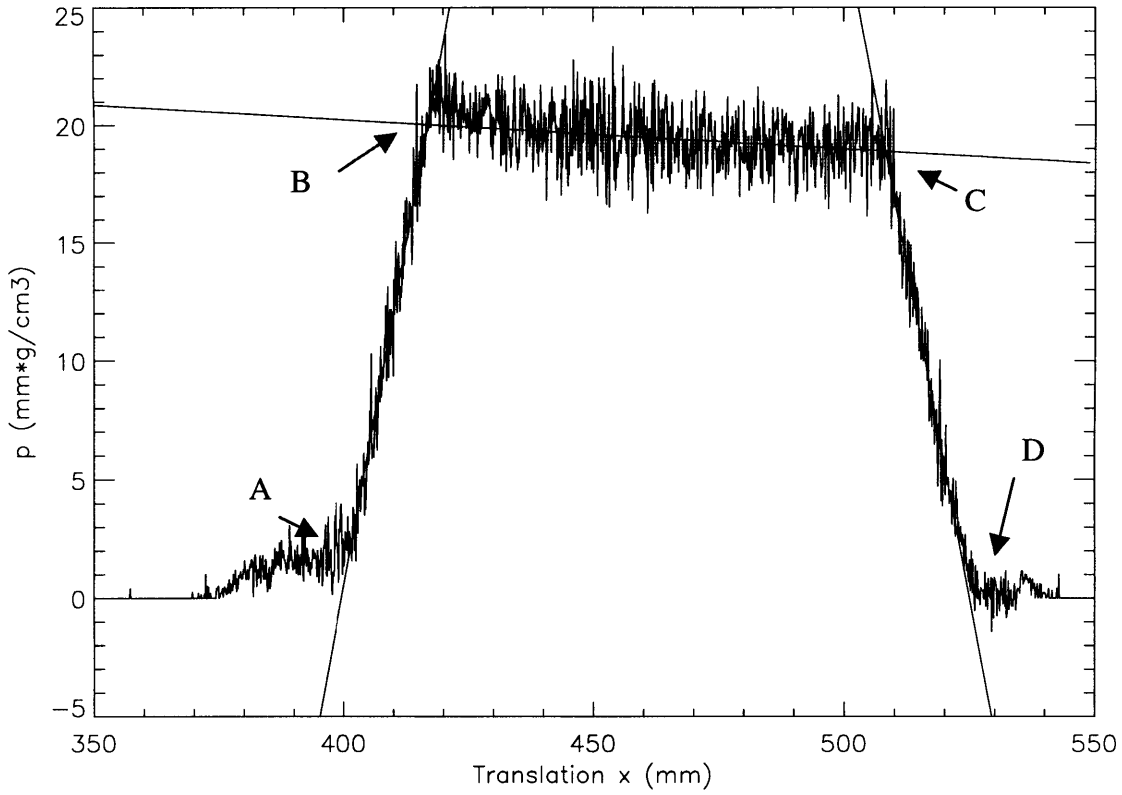

Figure 4.15. $p_{liquid}(x,\theta)$ function measured at θ=16° and fitted to a trapezoid.

The intersections of the fitted lines yield four points, labeled A, B, C and D, corresponding respectively to the top left, the bottom left, the top right and the bottom right corners of the liquid zone, as can be inferred from Figure 4.12. The abscissa x' of each point where obtained for all angles and fitted to Eq. 28. The geometry of the liquid zone was therefore fully determined. The same process was applied to the solid data set p_{solid}. A diagram of the block geometry was created from the calculated corner coordinates, and is shown in Figure 4.16.

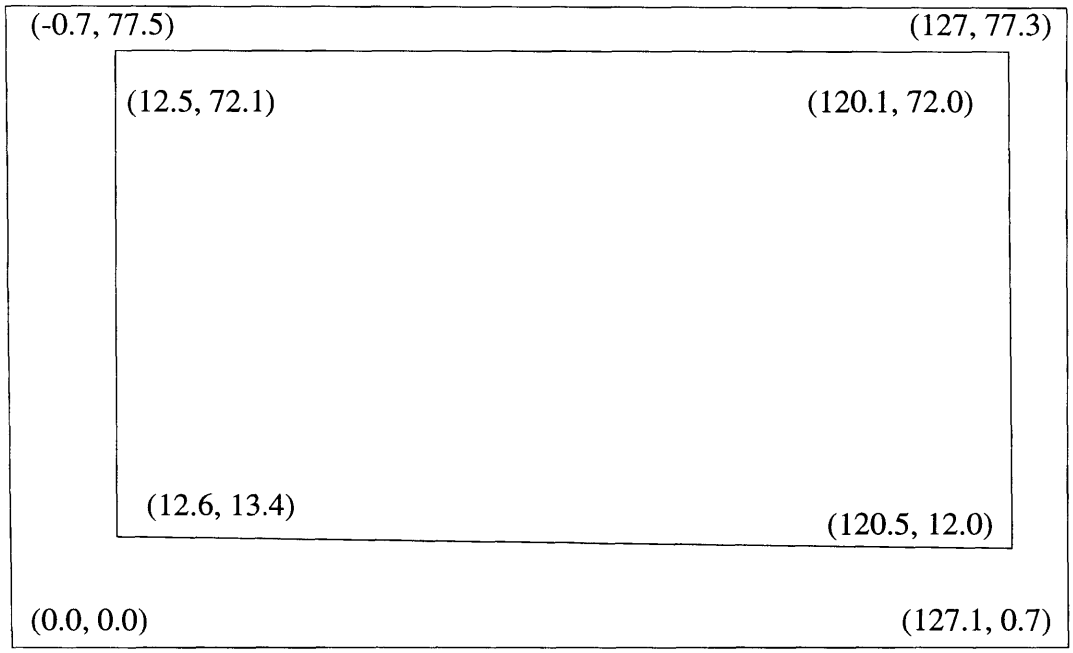

Figure 4.16. Geometry of the cast-like aluminum object obtained using model-based reconstruction.

To quantify the performance of this algorithm, we compare the results shown above to the expected quantities:

Dimension	Actual value (mm)	Reconstructed value (mm)	Error (mm)
Block width	127.0	127.5	+ *0.5*
Block height	76.2	77.4	+ *1.2*
Liquid zone width	108.0	107.7	- *0.3*
Liquid zone height	57.2	59.3	+ *2.1*
Left wall thickness	12.7	12.9	+ *0.2*
Right wall thickness	6.4	6.8	+ *0.4*
Bottom wall thickness	12.7	12.7	+ *0.0*
Top wall thickness	6.4	5.3	- *1.1*

Table 4.1. Actual and reconstructed dimensions of the cast-like object.

The numbers presented in Table 4.1 were obtained by averaging the coordinates shown in Figure 4.16 under the assumption that the solid and liquid boundaries were rectangular. Agreement between expected and measured values was good, with an error on the order of 1 mm. If one relaxed the requirement that the boundaries be perfectly rectangular, i.e. if one took the corner coordinates at face-value, the algorithm still produced fairly good results, although the error in the measurements was greater.

4.3. Discussion

It is clear from the results presented in the previous section that an object model based algorithm is the most promising approach in identifying the geometry of the solidification front in a metal cast using a translate-only experimental setup. Laminography suffers from severe blurring and will not work when locating large features. Iterative reconstruction algorithms are too sensitive to noise to be successful. By reducing the numbers of degrees of freedom in fitting the experimental data, a model-based approach allows one to discriminate between geometries more successfully. Because many samples are used to perform a single fit, the result is less sensitive to noise.

4.3.1. Performance Analysis

Because the beam width of the CastScan system is approximately 1.4 mm in the neighborhood of the imaged object, one can expect that the smallest feature detectable using this technique, such as a solid wall thickness, is on the same order. In the implementation described in section 4.2.4, the coordinates of the block corners were obtained by measuring the point at which slope changes occur in the translation data. If the sloped part of the curve extends over a translational distance on the order of the beam width, the fit cannot be performed. Indeed, experimental results showed that corner coordinates obtained using small angle data were incorrect and could not be used in the fitting process. This shows the importance of measuring line integrals at large angles.

The question arises of how many angular measurements are needed and how fine the translational steps must be to accurately locate the position of a corner. The limiting factor in an experiment such as this one is noise, which is typically caused by the photon statistics of the attenuation measurements, but can also be related to the equipment, such as source or electronic fluctuations. The quality of the calculation of x' is a function of the quality of the linear regression fit on the rising and falling slopes of the trapezoid shown in Figure 4.15. Let (x_i, y_i), i =1, ..., M, be a series of M measured data points that must be fit to the linear equation:

$$y = a + bx \qquad \text{Eq. 30}$$

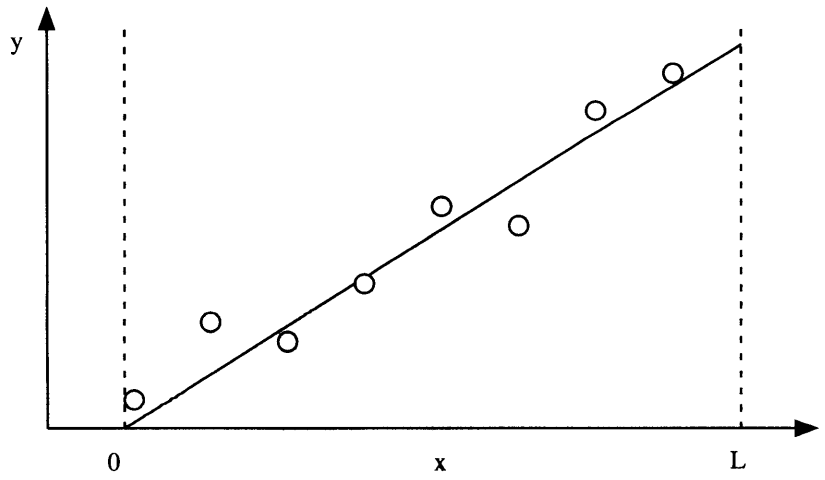

Figure 4.17. Example of a linear fit.

The parameters a and b are found using the following expressions [35]:

$$b = \frac{\sum_i x_i y_i - M\overline{xy}}{\sum_i x_i^2 - M\overline{x}^2} \qquad \text{Eq. 31}$$

$$a = \overline{y} - b\overline{x} \qquad \text{Eq. 32}$$

where $\overline{x}$ and $\overline{y}$ are the average values of x_i and y_i respectively.

Assuming the x_i's are exactly known and the variance of the measurement of y_i is σ_y^2, the variance of b is given by:

$$\sigma_b^2 = \frac{\sigma_y^2}{S_{xx}} \qquad \text{Eq. 33}$$

where

$$S_{xx} = \sum_i (x_i - \overline{x})^2 \qquad \text{Eq. 34}$$

These expressions can be simplified by assuming the x_i values range from 0 to L and are evenly spaced. In that case, their average $\bar{x}$ is equal to $L^2/4$, and Eq. 34 becomes:

$$\begin{aligned} S_{xx} &= \sum_i x_i^2 - M\bar{x}^2 \\ &= \sum_{i=1}^{M}\left(\frac{i-1}{M-1}L\right)^2 - M\frac{L^2}{4} \\ &\approx \frac{ML^2}{3} - \frac{ML^2}{4} = \frac{ML^2}{12} \end{aligned} \qquad \text{Eq. 35}$$

Eq. 33 can now be written as:

$$\sigma_b^2 = \frac{12\sigma_y^2}{ML^2} \qquad \text{Eq. 36}$$

The variance in a is given by:

$$\begin{aligned} \sigma_a^2 &= \frac{\sigma_y^2 \sum_i x_i^2}{MS_{xx}} \\ &= \sigma_y^2 \frac{ML^2/3}{M^2L^2/12} \\ &= \frac{4\sigma_y^2}{M} \end{aligned} \qquad \text{Eq. 37}$$

Let us assume that we need to locate a rectangular liquid zone that has a height t_l, as shown in Figure 4.18.

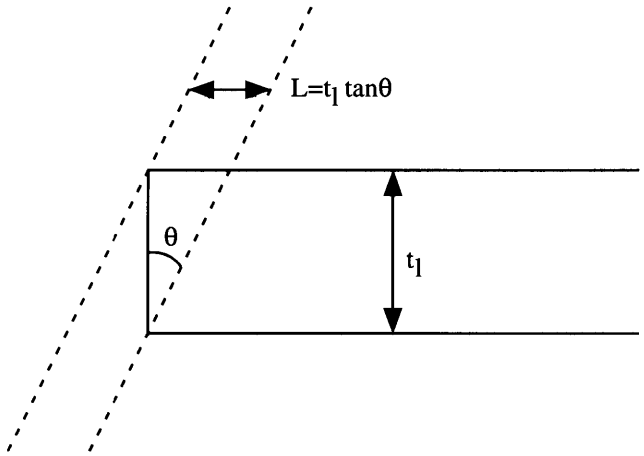

Figure 4.18. Width of the linear fit region.

The slope of the fitted points, b, is expected to have the value:

$$b = \frac{\Delta\rho}{\sin\theta} \qquad \text{Eq. 38}$$

where $\Delta\rho$ is the density difference between the solid and liquid areas.

Let us consider the bottom left corner of the liquid area. The goal of the fitting process is find the value x' for which:

$$y_0 = \frac{\rho t_l}{\cos\theta} = a + bx' \qquad \text{Eq. 39}$$

Solving for x' gives:

$$x' = \frac{y_0 - a}{b} \qquad \text{Eq. 40}$$

Knowing the variances of a and b allows us to calculate that of x':

$$\sigma_{y_0-a}{}^2 = \sigma_a{}^2 \qquad \text{Eq. 41}$$

Then:

$$\sigma_{x'}{}^2 = \left(\frac{1}{b^2}\right)^2 \sigma_{y_0-a}{}^2 + \left(\frac{(y_0-a)^2}{b^4}\right)\sigma_{b^2} \qquad \text{Eq. 42}$$

Using the identity:

$$y_0 - a = bL \qquad \text{Eq. 43}$$

one obtains

$$\begin{aligned}\sigma_{x'}{}^2 &= \frac{4\sigma_y{}^2}{b^2 M} + \frac{b^2 L^2}{b^4}\frac{12\sigma_y{}^2}{ML^2} \\ &= \frac{16}{b^2 M}\sigma_y{}^2\end{aligned} \qquad \text{Eq. 44}$$

If measurements are performed with a translational spacing Δx, the number of samples used in the fit is equal to:

$$M = \frac{L}{\Delta x} = \frac{t_l \tan\theta}{\Delta x} \qquad \text{Eq. 45}$$

So that:

$$\sigma_{x'}{}^2 = \frac{16\sin^2\theta}{\Delta\rho^2}\sigma_y{}^2\frac{\Delta x}{t_l \tan\theta} \qquad \text{Eq. 46}$$

Finally, the value of z, which is the distance from the source to the corner, is obtained by inverting Eq. 28:

$$z = \frac{x' - x_{offset}}{\tan\theta} \qquad \text{Eq. 47}$$

The variance in z becomes:

$$\begin{aligned} \sigma_z^{\,2} &= \frac{\sigma_{x'}^{\,2}}{\tan^2\theta} \\ &= \frac{16\sigma_y^{\,2}}{\Delta\rho^2}\frac{\Delta x}{t_l}\frac{\cos^3\theta}{\sin\theta} \end{aligned} \qquad \text{Eq. 48}$$

Recognizing that y_i are the measured values of p_{liquid}, we obtain the standard error of the measurement of z as a function of $\sigma_{p,liquid}$:

$$\sigma_z = \frac{4\sigma_{p_{liquid}}}{\Delta\rho}\sqrt{\frac{\Delta x}{t_l}\frac{\cos^3\theta}{\sin\theta}} \qquad \text{Eq. 49}$$

It is now necessary to quantify the standard error in the measurement of the p_{liquid} integral. Let t be the thickness of the aluminum block. If N_0 photons are emitted toward the detector, the number of detected photons N is equal to:

$$N = N_0 e^{-\frac{\mu t}{\cos\theta}} \qquad \text{Eq. 50}$$

and consequently,

$$p = \frac{\rho t}{\cos\theta} = -\frac{\rho}{\mu}\ln\left(\frac{N}{N_0}\right) \qquad \text{Eq. 51}$$

The standard error in the number of detected photons is equal to the square root of N, so that the standard error of the ratio N/N_0 is equal to:

$$\sigma_{\frac{N}{N_0}} = \frac{\sqrt{N}}{N_0} \qquad \text{Eq. 52}$$

In general, if u is a function of a variable x, then its variance is given by the following equation:

$$\sigma_u^{\,2} = \left(\frac{\partial u}{\partial x}\right)^2 \sigma_x^{\,2} \qquad \text{Eq. 53}$$

Consequently, the standard error of the measurement after calculating its logarithm is equal to:

$$\sigma_{\ln\frac{N}{N_0}} = \frac{N_0}{N}\frac{\sqrt{N}}{N_0} = \frac{1}{\sqrt{N}} \qquad \text{Eq. 54}$$

One obtains the standard error for the measurement of p:

$$\sigma_p = \frac{\rho}{\mu}\frac{1}{\sqrt{N}} = \frac{\rho}{\mu\sqrt{N_0}} e^{\frac{\mu t}{2\cos\theta}} \qquad \text{Eq. 55}$$

The quantity p_{liquid} is equal to the difference between the measured values of p_{solid} and $p_{combinaed}$. One can assume that each of the later values has a approximately the same standard error σ_p, so that the standard error of p_{liquid} is equal to:

$$\sigma_{p_{liquid}} = \sqrt{2}\sigma_p = \frac{\sqrt{2}\rho}{\mu\sqrt{N_0}} e^{\frac{\mu t}{2\cos\theta}} \qquad \text{Eq. 56}$$

Combining Eq. 49 and Eq. 55, and recognizing that the z-resolution r_z is equal to $2.35\sigma_z$ for a normal distribution, gives us the resolution for the corner position z as a function of the angle θ:

$$r_z = 2.35\sigma_z = \frac{2.35 \cdot 4\sqrt{2}}{\mu\sqrt{N_0}} e^{\frac{\mu t}{2\cos\theta}} \frac{\rho}{\Delta\rho} \sqrt{\frac{\Delta x}{t_l} \frac{\cos^3\theta}{\sin\theta}} \qquad \text{Eq. 57}$$

The system parameters for the experiment described in the previous section are:

- $\mu = 0.016\ \text{mm}^{-1}$
- $\Delta\rho/\rho = 11\%$
- $t = 76.2\text{mm}$
- $t_l = 57\ \text{mm}$
- translation step size $\Delta x = 0.13\ mm$
- $N_0 = 6 \times 10^7$ photons over three pulses

Figure 4.19 shows the vertical resolution as a function of θ calculated using Eq. 57.

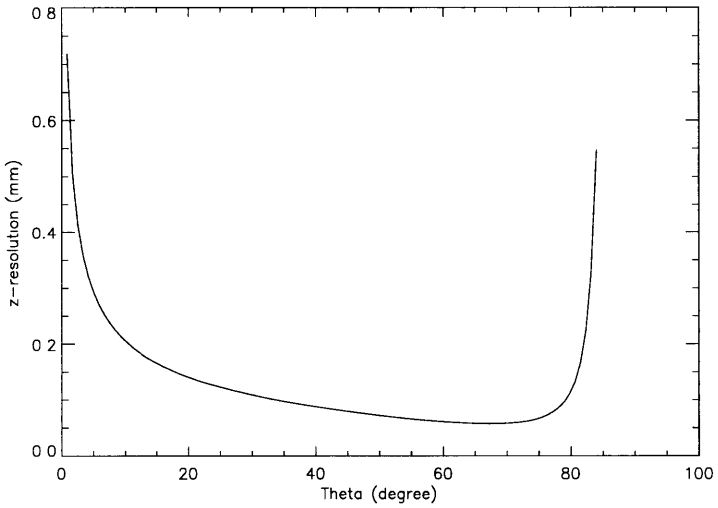

Figure 4.19. Theoretical z-resolution as a function of the ray angle.

As expected, the resolution is extremely poor at low angles because few data points are obtained across the edge at those angles. As the angle increases, the resolution improves until photon noise becomes important at very large angles.

Using the parameters specified above, the theoretical value of σ_p at $\theta=0$, calculated Eq. 55, is approximately equal to 40 mm·g/mm^3. To confirm this prediction, it was measured using the collected experimental data, and was found to be 646 mm·g/mm^3. This difference was caused by the linac fluctuations which correspond to a modulation of the measured intensity on the order of 0.1%. Let q be the fractional modulation in the linac output N_0, such that:

$$q = \frac{\sigma_{N_0}}{N_0} \qquad \text{Eq. 58}$$

Eq. 52 becomes:

$$\sigma_{\frac{N}{N_0}} = \sqrt{\frac{N}{N_0^{\,2}} + \frac{N^2}{N_0^{\,2}} q^2} \qquad \text{Eq. 59}$$

After taking the logarithm, we find:

$$\sigma_p = \frac{\rho}{\mu}\sqrt{\frac{1}{N} + q^2} \qquad \text{Eq. 60}$$

The level of the linac fluctuations can be exactly found using:

$$q = \sqrt{\left(\sigma_p \frac{\mu}{\rho}\right)^2 - \frac{1}{N_0 e^{-\mu t}}} \qquad \text{Eq. 61}$$

Using the parameters specified above, we find $q=0.38\%$.

One can obtain a more realistic formula for the resolution r_z by using Eq. 60 instead of Eq. 55, yielding:

$$r_z = \frac{2.35 \cdot 4\sqrt{2}}{\mu} \frac{\rho}{\Delta\rho} \sqrt{q^2 + \frac{e^{\frac{\mu t}{\cos\theta}}}{N_0}} \sqrt{\frac{\Delta x}{t_l} \frac{\cos^3\theta}{\sin\theta}} \qquad \text{Eq. 62}$$

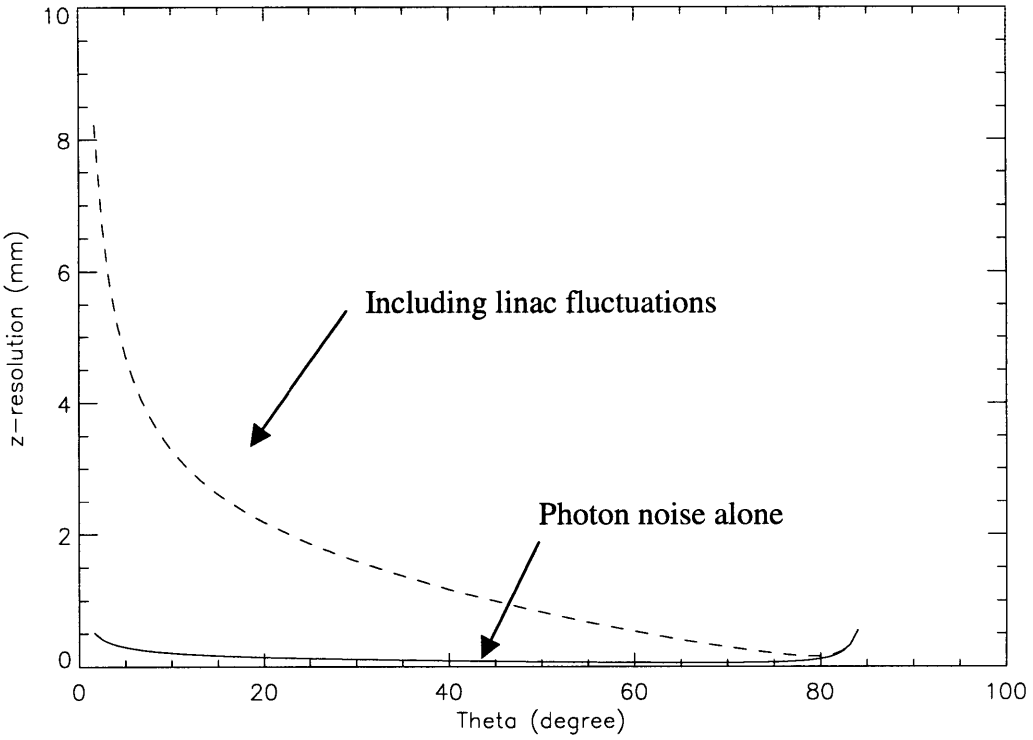

Figure 4.20. z-resolution as a function of the ray angle θ assuming linac fluctuations and photon statistical noise.

The vertical resolution is significantly worse once linac fluctuations are accounted for. This plot illustrates the importance of obtaining more than a single measurement to determine the position of the corners. At angles less than 16°, as is the case in our experiment, the resolution cannot be expected to be better than 2mm. By averaging the coordinate values obtained from each measurement with a weight equal to the inverse of the resolution, an overall value can be obtained, with a resolution given by:

$$r_z = \frac{\sqrt{N_\theta}}{\sum_\theta \frac{1}{r_{z,\theta}}} \qquad \text{Eq. 63}$$

where $r_{z,\theta}$ is given by Eq. 62. Applying this formula to the parameters of our experiment, we obtain an overall resolution of 0.34mm. This value appears to be better than the actual results would suggest. One must take into account the tolerances in the manufacture of the aluminum block to explain this apparent discrepancy.

As Figure 4.15 shows, the resolution is better at large angles than at small ones, provided the angle does not reach the point where photon noise becomes dominant. Therefore, it might be advantageous to slant the axis of the x-ray beams, so that the overall resolution given by Eq. 63 is improved. This situation is illustrated in Figure 4.21.

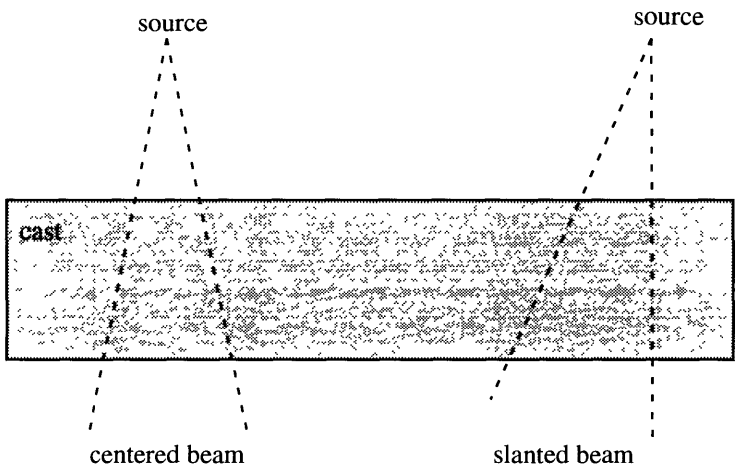

Figure 4.21. Translation experiment performed with a centered beam (left) and with a slanted beam (right).

Using the set of equations presented in this section, one can calculate the step size Δx required to achieve a given vertical resolution Δy. The data acquisition time is equal to the ratio of the total translation distance and the translation speed. The total translation distance can be derived geometrically from the length of the block l, the distance between the source and the back of the cast s, and the maximum ray angle θ_{max}, as shown in Figure 4.22.

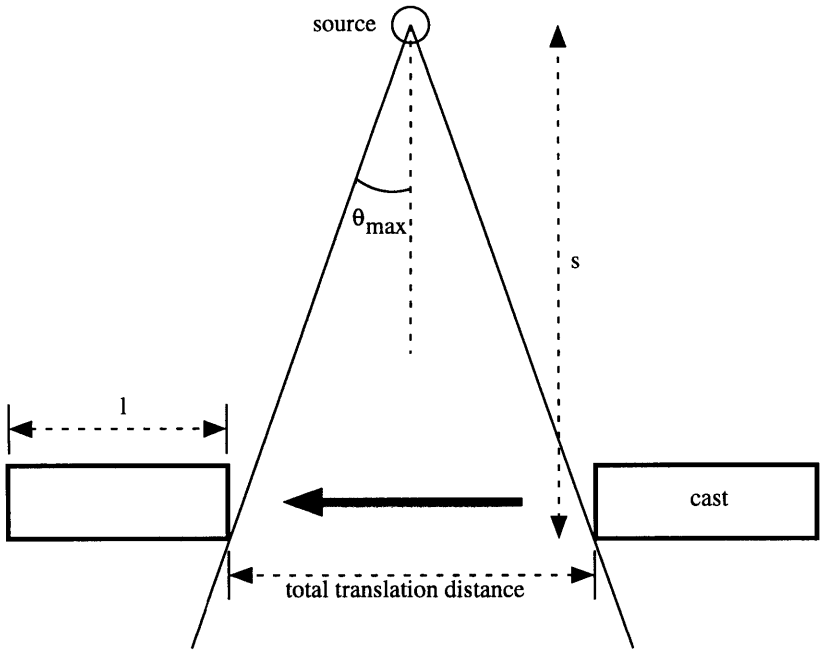

Figure 4.22. Diagram showing the total translation distance required to obtain a complete data set.

The data acquisition time can be calculated using the following formula:

$$time = \frac{l + 2s\tan\theta_{max}}{\Delta x}\frac{1}{f} \qquad \text{Eq. 64}$$

where f is the measurement frequency. Reducing the data acquisition time can be achieved by choosing a small source to object distance, although the effective ray width may increase as a consequence. Maximizing the measurement frequency is also important, although this parameter is mainly a function of the linear accelerator. Finally, the translational step size should be as great as possible. In terms of this last parameter, we see that the data acquisition time follows the following trends:

$$time \propto \sqrt{q^2 + \frac{e^{\mu \cdot t}}{\Phi \cdot d_w \cdot d_h}}\frac{1}{N_\theta}\frac{1}{r_z^{\,2}}\frac{1}{t_l}\frac{1}{(\Delta\rho/\rho)^2} \qquad \text{Eq. 65}$$

where d_w and d_h are the detector width and height respectively, and ϕ is the photon flux at the detector position. If linac fluctuations are not an issue, minimizing acquisition time requires maximizing the photon flux and using a large slice thickness. This may be the case if the block were made of steel and had a thicker cross-section. Photon flux decreases as the square of the distance between the source and the detectors, so placing the detectors close to the source is important. If linac fluctuations are the dominant source of noise, as in this experiment, then reducing them becomes the priority. Clearly, using as many detectors as possible spread over as wide an angle as possible is important. Acquisition time increases as the square of the inverse of the density contrast, so measuring the location of a liquid area with a 2% density contrast takes four times longer than measuring one with a 4% contrast. Finally, imaging time increases linearly with the length of the cast. If the cast were particularly long, it may be possible to reduce acquisition time by focusing on the corners, and speeding up the translation while the beam is scanning the center of the block.

The data acquisition time in this experiment was 68 seconds. This time could be reduced to one third of that value if the linear accelerator output were stabilized, allowing measurements at a sampling frequency of 180 Hz instead of 60Hz. Good results could probably be achieved with a larger step size, further decreasing the imaging time.

4.3.2. Performance with a Realistic Cast

The aluminum block used in the experiment described here was small in order to accommodate conventional CT imaging. One might be more interested in the predicted performance for a more realistic object. Steel is inherently more difficult to image than aluminum due to its high density and the resulting increase in photon statistical noise. We will therefore consider the following experimental parameters:

- steel cast with a length l = 400mm, and a width t = 250 mm
- liquid zone with a density difference of $\Delta\rho/\rho$ = 5% and a width t_l = 230 mm.
- source to object distance s = 500 mm.
- linac operated at f = 180 Hz, with q = 1%.
- 32° fan beam slanted by 16°.

- $\mu = 0.045$ mm^{-1} (steel at 1.1 MeV).
- translation step size $\Delta x = 0.05$ mm.
- $N_0 = 2 \times 10^7$ photons over 1 pulse.

In a slanted beam configuration, the imaging time is given by:

$$time = \frac{l + s\tan\theta_{max}}{\Delta x}\frac{1}{f} \qquad \text{Eq. 66}$$

This equation yields an imaging time of 80 seconds for this object. The predicted resolution, including linac fluctuations, was calculated using Eq. 62 and is shown in the following figure.

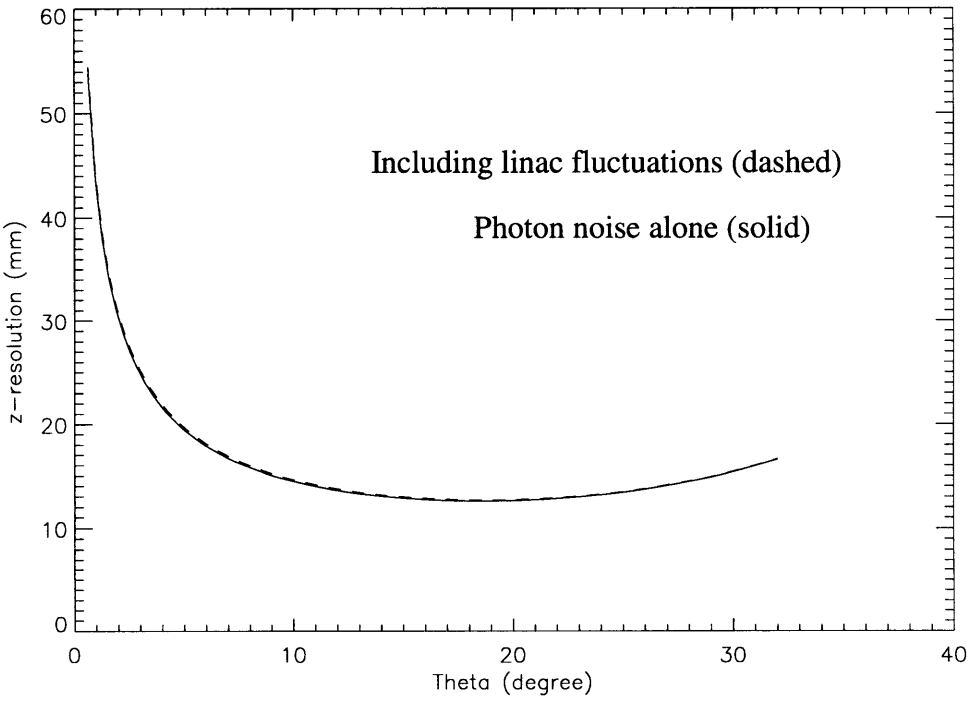

Figure 4.23. Predicted z-resolution for a steel cast as a function of the ray angle θ.

One striking feature of Figure 4.23 is that linac fluctuations of 1% do not affect the resolution. This is due to the high density and thickness of this object resulting in a noise

regime dominated by the photon statistics. For this reason, the 180 Hz pulse rate can be used despite its modulation, resulting in a smaller translation step size.

The aggregate resolution, calculated using Eq. 63, was found to be 1.36 mm, shows that this technique could prove useful on large, dense metal objects.

4.3.3. Improvements and Future Work

The model-based technique can be extended by taking into account the projection data obtained at the angle $\theta = 0°$. The quantity $p_{liquid}(x, \theta=0)$ can be divided by the density difference between the solid and the liquid zone, resulting with the width of liquid zone along the beam axis for all translational positions x. In this experiment, the translational step size was equal to 0.134 mm, which is needlessly small for our purpose. The noise in the measurement of the liquid zone width can be reduced by averaging over consecutive translational samples, while maintaining an adequate resolution.

Real metal casts do not perfectly fit into the rectangle-within-a-rectangle model upon which the algorithm described above relies. One possible deviation from this model would be the inclusion of rounded corners. The effect of this is to smooth the slope change that occurs when a ray reaches a corner, as shown in the following figure.

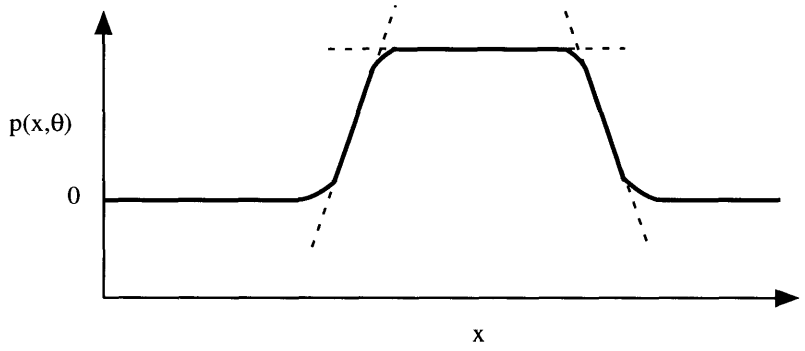

Figure 4.24. Integrated profile p of a rectangular object with rounded corners.

As is shown, one expects the slope change to be smoothed out. A similar effect happens due to the finite beam width. At large angles, a sufficient number of data points would be available to perform a good linear fit. However at small angles, or if the corners were very round, the fit might not be feasible. This once again emphasizes the importance of measurements at large angles.

It may be possible to assign a radius of curvature to the rectangle corners and include such a parameter in the curve fitting process. Other analytical models of real casts could be used, as long the number of degrees of freedom was maintained sufficiently low to allow good fits to be performed, and as long as the features were large enough to ensure a sufficient number data points were available for the fitting process.

As mentioned earlier, the importance of the translate-only model fitting technique is that its implementation at a metal casting facility is more feasible than that of a conventional CT system. Its advantage lies in a simplified motion system, manageable shielding requirements, and possibly shorter scanning times than CT. Although conventional CT holds great promise for the study of the metal solidification process itself, future work may prove that the translate-only approach is valuable in the design of a fast and practical online monitoring sensor for the metal casting industry.

APPENDIX A.
Notes of Experimental Methods

A.1. Center of Rotation Calibration

In CT, it is crucial that the center of rotation of the object being rotated be correctly placed with respect to the detectors. For this experiment, a solid aluminum cylinder 19 mm in diameter was bolted to the rotary stage at a 7.6 cm offset from the center of rotation. The sinogram of the cylinder, shown in Figure A.1, was obtained, and the centroid of the tube was located at each of the 2700 views taken over an angular range of 360°. Taking the average of the centroid values allowed us to obtain a precise measurement of the position of the center of rotation of the system in terms of the detector number. Assuming the detectors were numbered 0 through 127, the center of rotation was translated until an average centroid position of 63.5 was obtained.

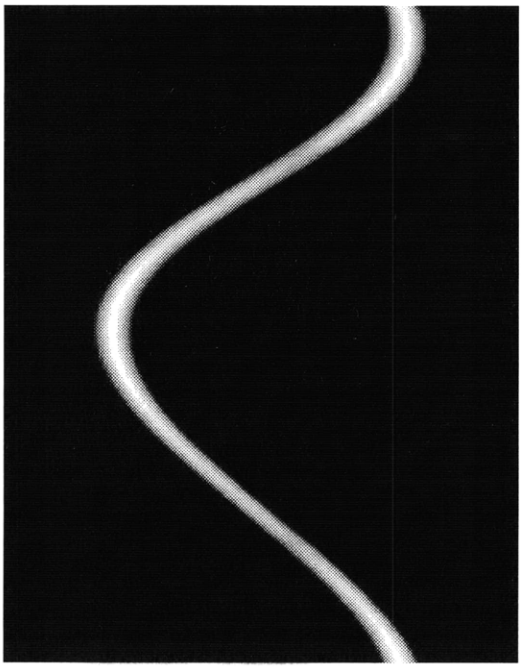

Figure A.1. Rod sinogram used the center of rotation calibration.

A.2. Data Acquisition Methods

Unlike typical medical CT systems, the CastScan experiment uses tungsten anti-scatter plates that are as wide as the detector channels. Consequently, the data acquired corresponds to narrower rays than expected, as shown in Figure A.2.

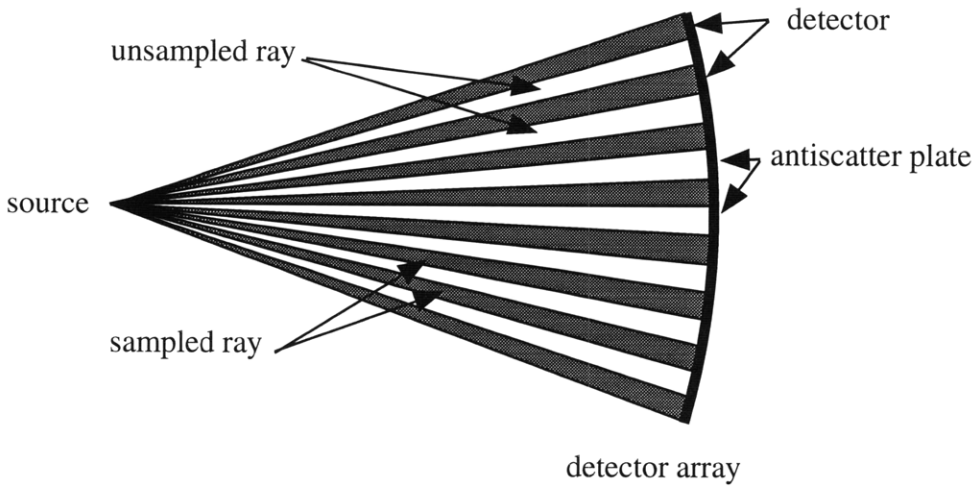

Figure A.2. Sampled and unsampled rays due to the anti-scatter plates.

This situation can lead to the undersampling artifacts presented in section 3.5.3. To prevent this, we implemented a data acquisition method that completes the missing ray measurements by performing a second sinogram acquisition with a center of rotation offset. Transforming from one ray space to the other may seem complicated, but gives a simple result. The geometry of the center of rotation shift can be described in terms of Figure A.3

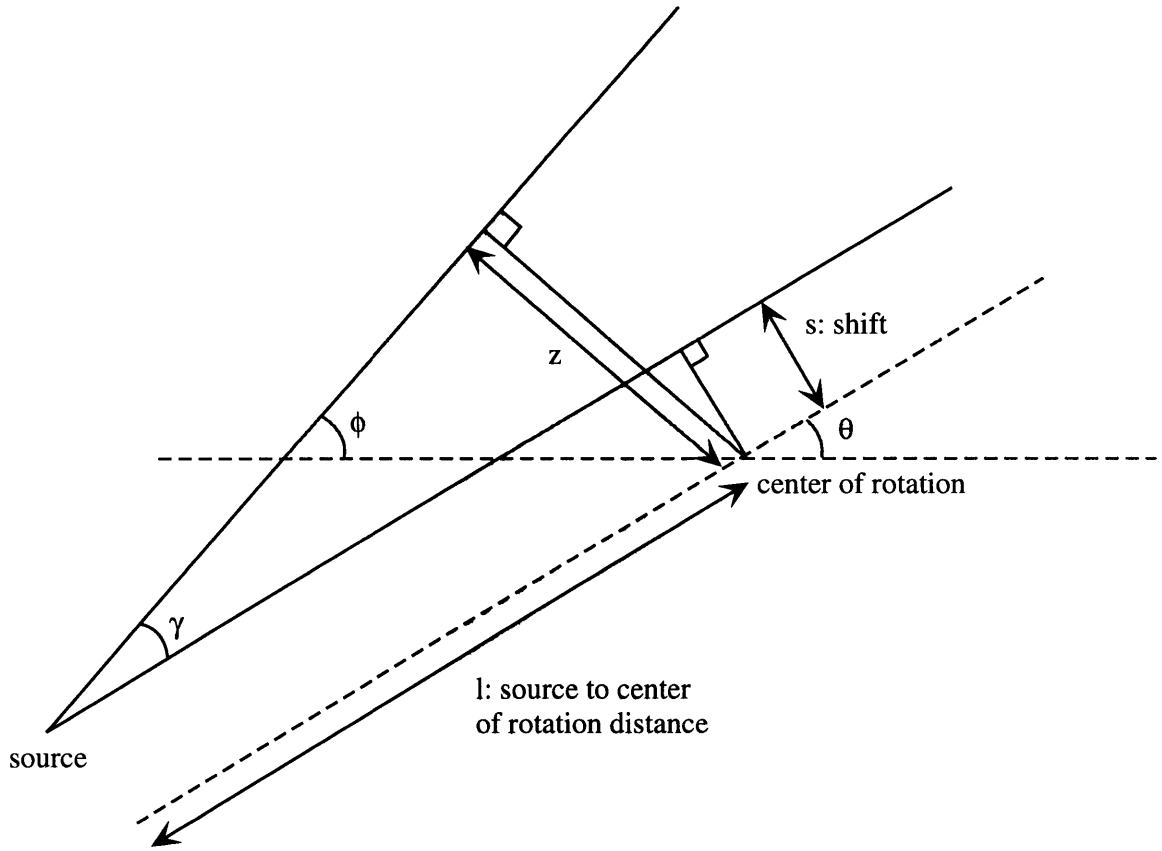

Figure A.3. Geometry of the center of rotation shift.

In this figure, we consider a ray that is acquired at a view angle φ and a detector angle θ, with a center of rotation shifted by a quantity s. The final goal of this operation is to transform from (θ,γ) space as measured with the shift to the (θ',γ') space with a shift equal to 0. First, we transform from (θ,γ) space to (ϕ,z) space, corresponding to a parallel beam geometry. This is accomplished using the following equations:

$$\varphi = \gamma + \theta \qquad \text{Eq. 67}$$

$$z = \frac{s}{\cos\gamma} + l\sin\gamma \qquad \text{Eq. 68}$$

These equations can be used to express ϕ and z in terms of θ' and γ' by equating s to 0. This yields the following equations:

$$\gamma' + \theta' = \gamma + \theta \qquad \text{Eq. 69}$$

$$l \sin \gamma' = \frac{s}{\cos \gamma} + l \sin \gamma \qquad \text{Eq. 70}$$

Let γ_0 correspond to the angle corresponding to a single detector, i.e. 0.125°. Because of the presence of the anti-scatter plates, the rays corresponding the angles $\gamma' = (2n + 1)\gamma_0$ are missing and must be recovered from the (θ,γ) data set. Clearly, it is practical to obtain a new sinogram with a constant center of rotation shift. Assuming the n=0 case, we can find the shift s for which $\gamma = 0$ and $\gamma' = \gamma_0$ from Eq. 70:

$$s = l \sin \gamma_0 \qquad \text{Eq. 71}$$

and from Eq. 69 we find the corresponding θ transformation:

$$\theta = \theta' - \gamma_0 \qquad \text{Eq. 72}$$

For values of $n \neq 0$, the situation is more complicated. The ideal shift is given by:

$$s_n = l \cos 2n\gamma_0 [\sin(2n+1)\gamma_0 - \sin 2n\gamma_0] \qquad \text{Eq. 73}$$

This is not exactly equal to the s value found for n=0, but the difference is small, as can be seen in the following plot of s_n/s versus n.

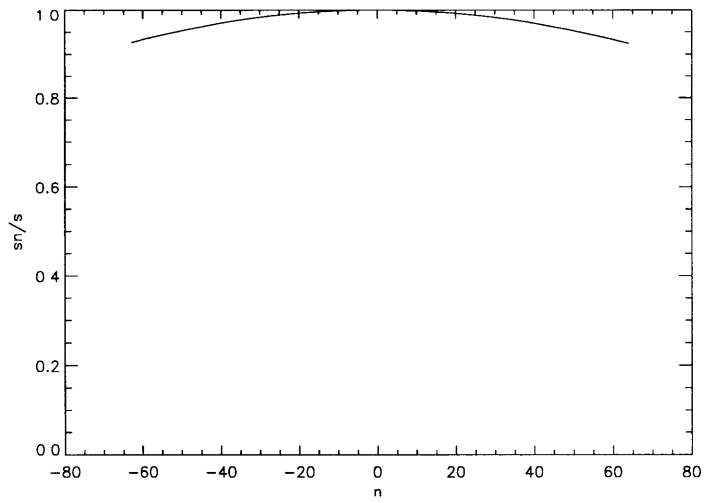

Figure A.4. Ratio of the ideal center of rotation shift s_n to the actual shift s.

The values are close, so that we use the following overall transformation:

$$\theta = \theta' - \gamma_0 \qquad \text{Eq. 74}$$

$$\gamma = \gamma' + \gamma_0 \qquad \text{Eq. 75}$$

using the shift specified in Eq. 71.

In the laboratory, the amount of the offset was measured by performing a center of rotation calibration measurement with an average centroid position equal to 64 rather than 63.5. The two sinograms obtained, one without the shift and the other with the shift, were re-combined together by using Eq. 74 and Eq. 75, with $\gamma_0 = 0.125°$.

APPENDIX B.
Hardware and Software

A single computer was used to perform motor control, data acquisition, data storage, and image reconstruction. In this section, we will review the specifications of the hardware used by the computer to perform these tasks. We will then examine the electronic circuitry used to synchronize the various systems and allow them to communicate. Finally, we will study the software written to allow the user to acquire data and reconstruct images.

B.1. Hardware Specifications.

The computer performs its tasks by controlling the following hardware:

- Nulogic® pcStep 4A 4 axis controller card, used to control motor operations.
- Data Translation DT3157 digital frame grabber card, used to communicate with DAS and acquire data.

Motor Control

The information presented in this section can be found in the pcStep4A motor control card manual [36]. The pcStep 4A card is a 4-axis open and closed loop stepper control board. It is designed for PC Compatible computers, and fits on the ISA bus. The card was linked to a motor amplifier placed in the control room via a 50-pin external connector. In turn, the amplifier was linked to the rotary and translational stages placed inside the shielded room and used to rotate the imaged object. The card is software programmable to instruct the motors to run at specified stepping rates, with user-selected acceleration profiles. These profiles are described in the context of the following diagram:

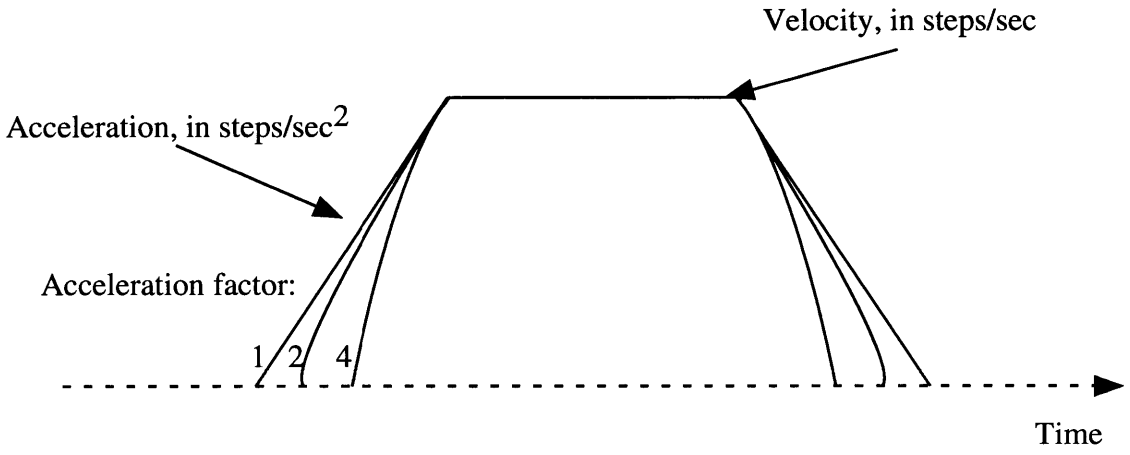

Figure B.1. Trapezoidal velocity profile generated by the motor control card.

The acceleration factor allows the user to minimize the acceleration time at the expense of a linear acceleration profile. In our experiments, the translational axis was moved at a speed of 8,000 steps/sec, an acceleration of 12,000 steps/sec^2, and an acceleration factor of 9. The rotary axis was operated at a speed of 8000 steps/sec, an acceleration of 10,000 steps/sec^2, and an acceleration factor of 1. On the translational axis, the travel distance corresponds to 1000 steps/mm, and on the rotary axis, the angular travel corresponds to 1000 steps/degree.

One important feature of this board is that it can store a sequence of motor operations in a buffer which is executed when an external trigger signal is received. This capability was crucial in the context of the CastScan experiment, as it was necessary to synchronize the beginning of the object rotation with the data acquisition. The board can receive trigger signals on any of 8 I/O bit pins located on the external 50-pin connector, which are set using TTL level signals. A trigger signal was supplied to the board via I/O port 1 (pin 9) from the timing and synchronization circuit described later in this section.

Data Acquisition

Although only 128 channels are used in the CT experiments explained in this document, the data acquisition system is capable of handling 192. As explained in section 2.4.2, a current proportional to the x-ray intensity is produced by each detector. The data acquisition system accumulates the charge generated by this current between each DAS triggering event, at which point the charge is measured. The DAS digitizes this value, and transfers this data along with the appropriate timing signals onto a 50-pin connector. The following table details the pin assignments of this connector:

Pin #	Signal	Pin #	Signal
1	DATA MODE (+)	2	DATA MODE (-)
3	VIEW TRIG (+)	4	VIEW TRIG (-)
5	IFPAG0 (+)	6	IFPAG0 (-)
7	IFPAG1 (+)	8	IFPAG1 (-)
9	ISOGND	10	ISOGND
11	RTN TRIG (+)	12	RTN TRIG (-)
13	ISOGND	14	ISOGND
15	DAS TEST +	16	DAS TEST (-)
17	DATA CLK (+)	18	DATA CLK (-)
19	D0 (+)	20	D0 (-)
21	D1 (+)	22	D1 (-)
23	D2 (+)	24	D2 (-)
25	D3 (+)	26	D3 (-)
27	D4 (+)	28	D4 (-)
29	D5 (+)	30	D5 (-)
31	D6 (+)	32	D6 (-)
33	D7 (+)	34	D7 (-)
35	D8 (+)	36	D8 (-)
37	D9 (+)	38	D9 (-)

39	D10 (+)	40	D10 (-)
41	D11 (+)	42	D11 (-)
43	D12 (+)	44	D12 (-)
45	D13 (+)	46	D13 (-)
47	D14 (+)	48	D14 (-)
49	D15 (+)	50	D15 (-)

Table B.1. Pin assignment table of the DAS connector.

The signals produced by the DAS are differential, and Table B.1 lists the polarity of each pin in parentheses. The digitized data is sent out as a 16-bit signal, covering pins 19 through 50. Data for each channel is emitted in a sequence, starting from channel 0 to channel 191. A clock signal, called DATA CLK, indicates when the data pins switch from one channel to the next. It constantly generates a pulse train with a 1.5 μs period, regardless of whether data is being transmitted. Sending the data is triggered by a pulse to the VIEW TRIG pins, with a maximum triggering frequency of 2000 Hz and a minimum of 250 Hz. The first trigger pulse received by the DAS is ignored. The DAS acknowledges the reception of a trigger signal by emitting a pulse lasting 3 clock cycles (4.5 μs) on the RTN TRIG channel approximately 8 μs later. Data transmission begins 20 cycles (30 μs) after the RTN TRIG pulse drops. The DAS TEST signal remains high during the entire duration of the data transmission. The IFPAG bits must be set to true in order for DAS to automatically adjust the amplifier gain control. Finally, the DATA MODE bit is set high to put the DAS into its test mode, or left low to send real data. In the test mode, the DAS will repeatedly transmit the sequence of 32 16-bit words listed in Table B.2.

Cycle	Test data (binary)	Test data (hex)	Cycle	Test data (binary)	Test data (hex)
1	0000 0000 0000 0000	0000	17	0111 1111 1111 1111	7FFF
2	0000 0000 1111 1111	00FF	18	1101 1111 1111 1111	DFFF
3	1111 1111 0000 0000	FF00	19	1111 0111 1111 1111	F7FF
4	0000 0000 0000 0000	0000	20	1111 1101 1111 1111	FDFF
5	1111 1111 1111 1111	FFFF	21	1111 1111 0111 1111	FF7F
6	1010 1010 1010 1010	AAAA	22	1111 1111 1101 1111	FFDF
7	0101 0101 0101 0101	5555	23	1111 1111 1111 0111	FFF7
8	1111 1111 1111 1111	FFFF	24	1111 1111 1111 1101	FFFD
9	1000 0000 0000 0001	8001	25	1011 1111 1111 1111	BFFF
10	0010 0000 0000 0100	2004	26	1110 1111 1111 1111	EFFF
11	0000 1000 0001 0000	0810	27	1111 1011 1111 1111	FBFF
12	0000 0010 0100 0000	0240	28	1111 1110 1111 1111	FEFF
13	0100 0000 0010 0000	4020	29	1111 1111 1011 1111	FFBF
14	0001 0000 0000 1000	1008	30	1111 1111 1110 1111	FFEF
15	0000 0100 1000 0000	0480	31	1111 1111 1111 1011	FFFB
16	0000 0001 0000 0010	0102	32	1111 1111 1111 1110	FFFE

Table B.2. DAS test sequence.

If the DAS is not in test mode, the 16-bit word transmitted via signal D0 through D15 can be translated into a voltage. The first two bits, D0 and D1 indicate the amplifier gain used, as indicated in Table B.3.

D0 state	D1 state	Gain
0	0	1
0	1	8
1	0	64

Table B.3. DAS gain table.

The remaining 14 data bits correspond to a number *d* between 0 and 16383. The voltage is calculated using the following equation:

$$\text{voltage} = \frac{d}{16383} \cdot \frac{1}{\text{Gain}} \cdot 10[\text{Volts}] \qquad \text{Eq. 76}$$

The DAS data is placed into the computer's memory by the DT3157 digital frame grabber board. Information relating to this board can be found in [37]. The DT3157 is designed to function with digital cameras, which typically send data as frames subdivided into lines. To enable the DAS and the frame grabber to communicate, it is necessary to "fool" the board into thinking it is dealing with a camera. The board is connected to a camera via a 68-pin connector for which the pin signal assignments are shown in Table B.4.

Pin #	Signal	Pin #	Signal	Pin #	Signal	Pin #	Signal
1	Ground	35	Ground	18	DIG IO3	52	DIG IO4
2	AD0 (+)	36	AD0 (-)	19	AD14 (+)	53	AD14 (-)
3	AD1 (+)	37	AD1 (-)	20	AD15 (+)	54	AD15 (-)
4	AD2 (+)	38	AD2 (-)	21	Ext. Trig.	55	Ground
5	AD3 (+)	39	AD3 (-)	22	Reserved	56	Reserved
6	AD4 (+)	40	AD4 (-)	23	Reset Out (+)	57	Reset Out (-)
7	AD5 (+)	41	AD5 (-)	24	FRA OUT (+)	58	FRA OUT (-)
8	AD6 (+)	42	AD6 (-)	25	FRA IN (+)	59	FRA IN (-)
9	AD7 (+)	43	AD7 (-)	26	LIN IN (+)	60	LIN IN (-)
10	AD8 (+)	44	AD8 (-)	27	LIN OUT (+)	61	LIN OUT (-)
11	AD9 (+)	45	AD9 (-)	28	CLK OUT (+)	62	CLK OUT (-)
12	Ground	46	Ground	29	CLK IN (+)	63	CLK IN (-)
13	AD10 (+)	47	AD10 (-)	30	SHUT (+)	64	SHUT (-)
14	AD11 (+)	48	AD11 (-)	31	DIG IO5	65	Ground
15	AD12 (+)	49	AD12 (-)	32	DIG IO6	66	Ground
16	AD13 (+)	50	AD13 (-)	33	DIG IO7	67	DIG IO8
17	DIG IO1	51	DIG IO2	34	Ground	68	Ground

Table B.4. DT3157 connector pin assignment table.

To make the DAS data readable by the frame grabber board, it is formatted into pixels, lines and frames. Because the DAS has 192 channels, each line is organized into 192 pixels. Lines are assembled into groups of 4096 to form a frame. This organization is shown in Figure B.2. Because lines are acquired at a rate of 360 Hz, it takes 11.4 seconds to acquire a frame.

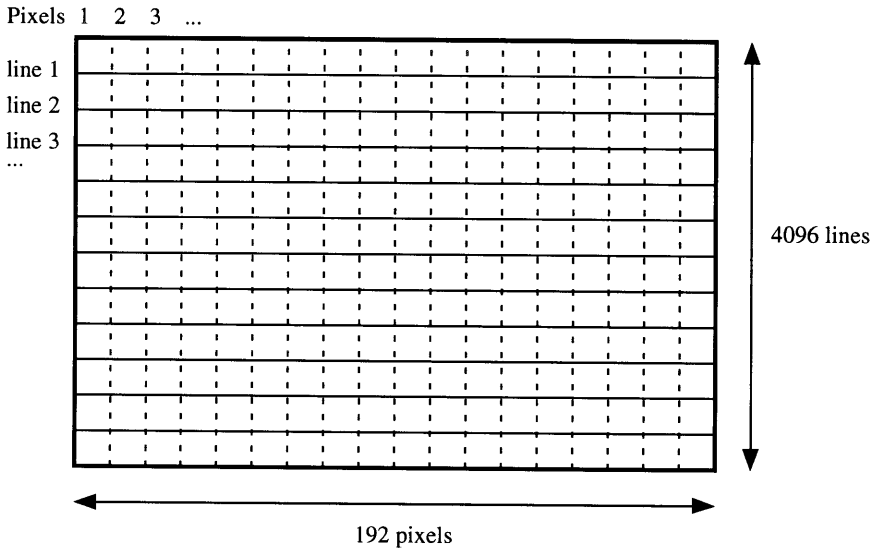

Figure B.2. Organization of a frame.

The DATA CLK clock signal produced by the DAS is used as the DT3157 pixel clock input signal, CLK IN. The data paths of the two systems are also directly connected, with signal D0 on the DAS corresponding to AD0 on the DT3157, etc... The RTN TRIG sent by the DAS prior to the transmission of the 192 channels information is linked to the LIN IN pin of the DT3157, allowing it to acquire each data set as a single line.

There remains to generate a FRA IN signal for the DT3157 board, to generate a trigger signal for the DAS, the motor control card and the linac, and to set up a mechanism for putting the DAS into its test mode. This is achieved by a purpose-built electronic circuit, described next.

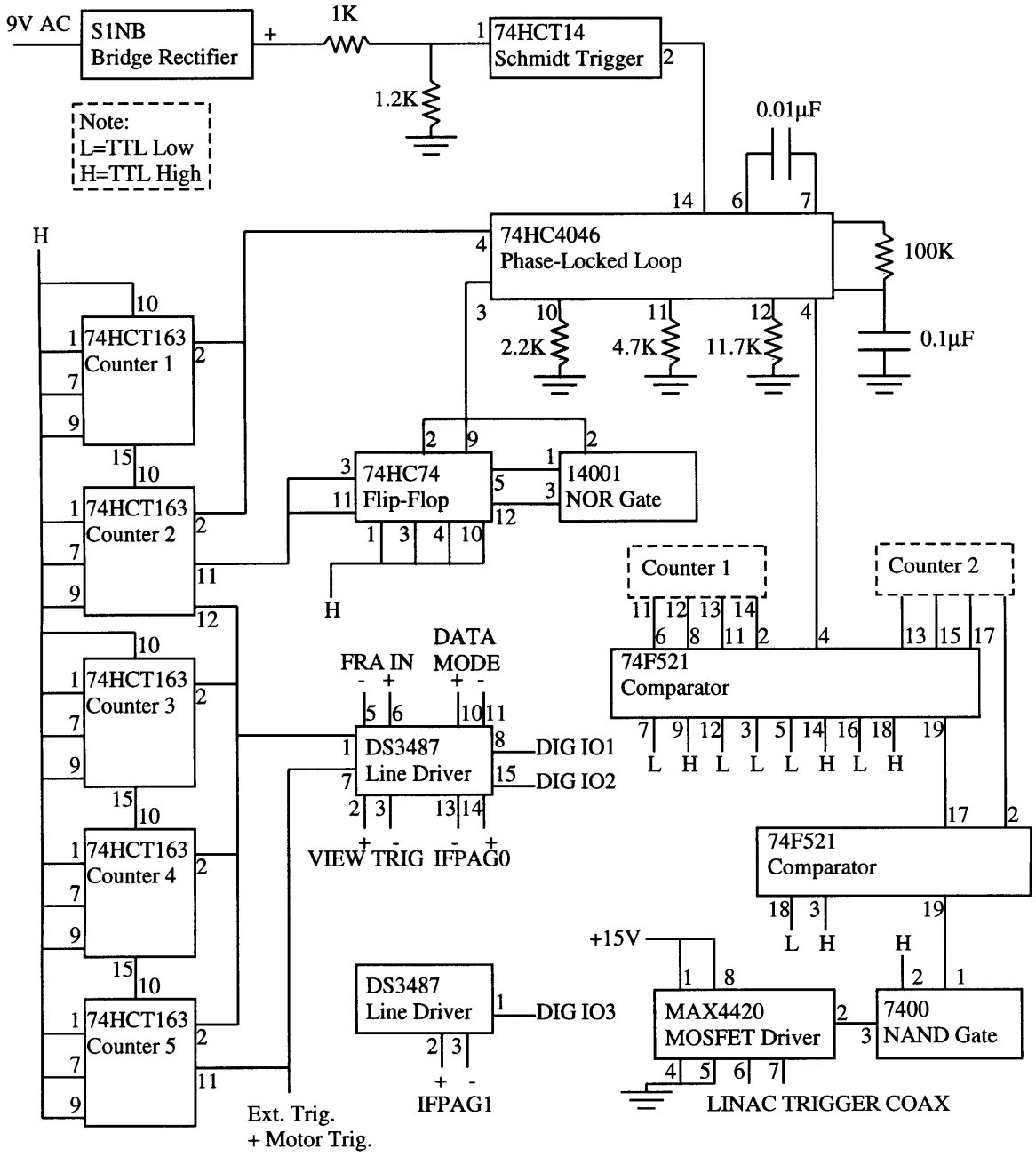

Figure B.3. Synchronization and triggering circuit.

The purpose of this circuit is to coordinate the motor control card, the DAS and the linear accelerator. To reduce the noise caused by the power supply ripple, the linac is fired at 180 Hz and is phase-locked with the grid. The phase locked loop (PLL) setup allows to obtain higher harmonics of the 60 Hz power signal by using a divider. In this case, a divide by 256 circuit is placed in series with a divide by 3 circuit, obtaining a 46 kHz pulse train and all the

half-frequencies down to 180 Hz. The 360 Hz is used to trigger the DAS, while a further divide by 4096 circuit produces a frame pulse every 11 seconds. It is necessary to trigger the DAS 400 μs prior to triggering the linac in order to allow all the channels to integrate over the x-ray pulse and the resulting afterglow. This is done using two 8-bit comparator chips. The overall timing diagram is shown next:

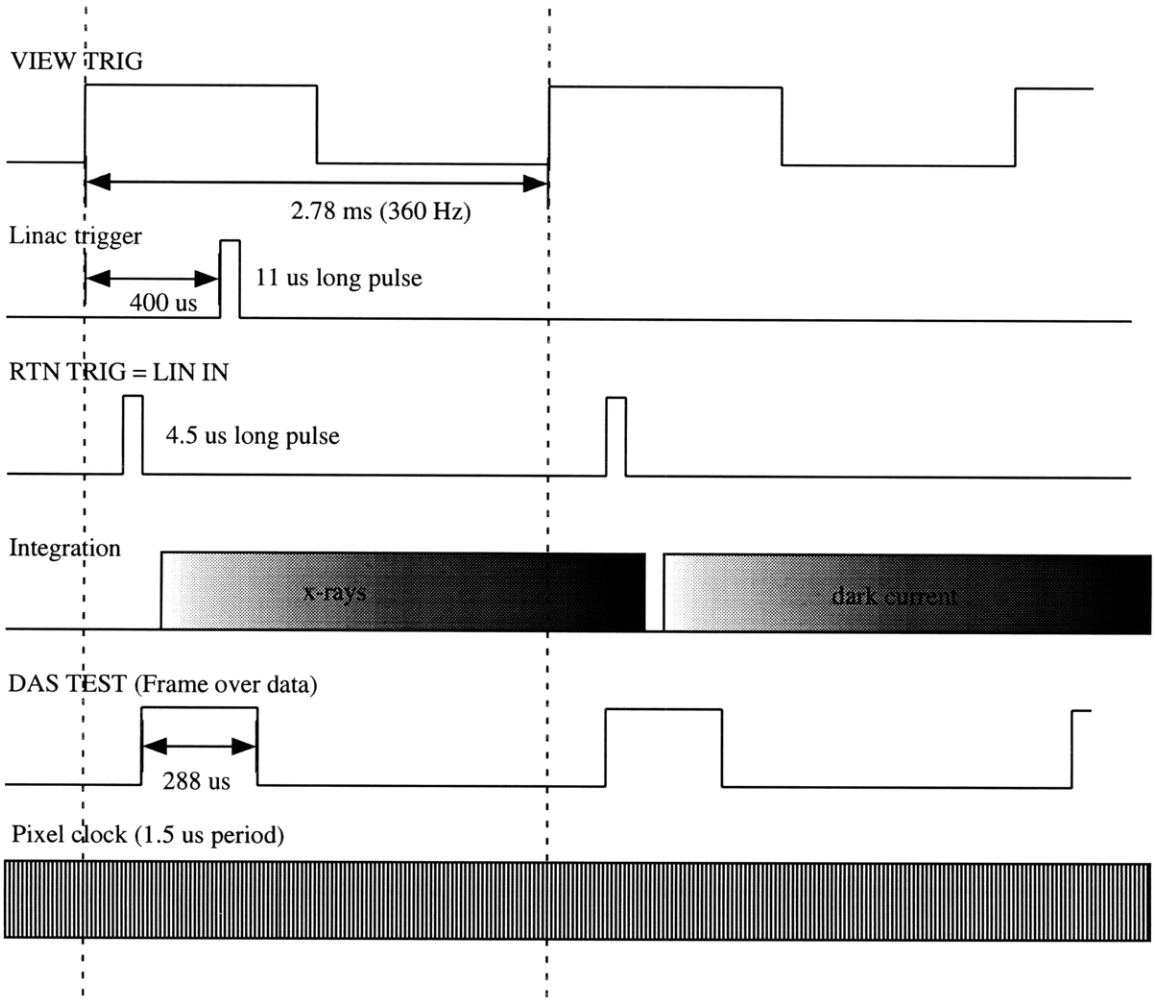

Figure B.4. DAS Timing Diagram.

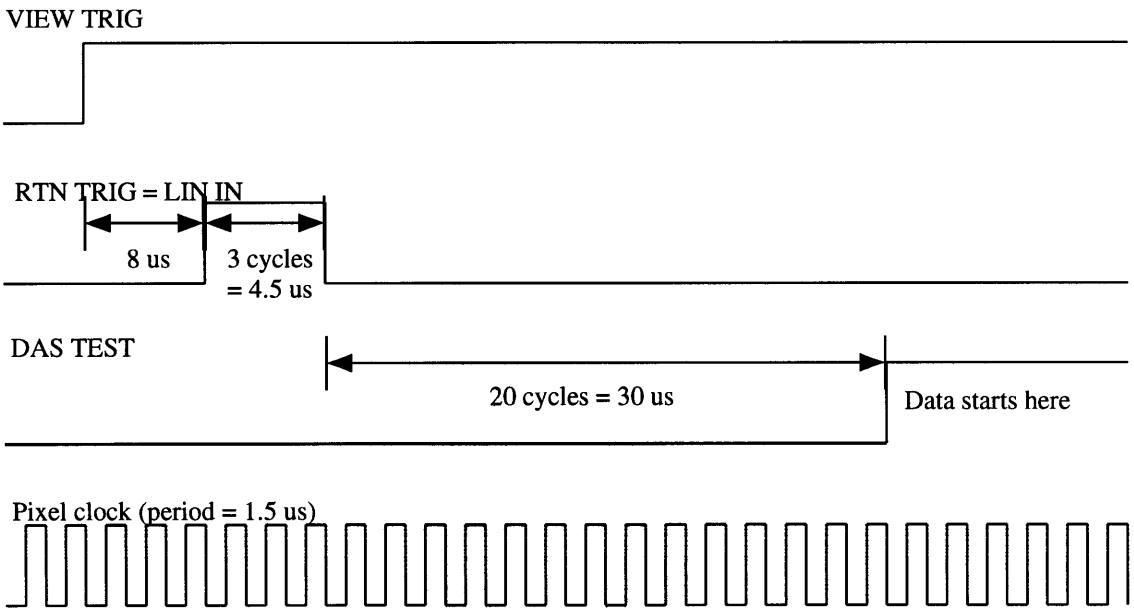

Figure B.5. DAS timing diagram (detail).

It should be noted that the DAS digitizes the accumulated charge for groups of 16 channels at a time. During this process, which lasts 24 μs, those channels are stop integrating. As a result, when the x-ray pulse occurs, the channels with a low index will have been integrating for a longer time than those with a higher index.

B.2. Software

A single program was written to perform motor control, data acquisition, data storage, and image reconstruction. In addition, it could be used to monitor the x-ray intensity measured by all 192 channels available from the DAS. The program provided a real-time intensity display, a time-averaged display as well as the absolute deviation from the mean for all channels. This proved to be a very useful diagnostic tool to analyze the linear accelerator's performance.

Both the motor control card and the frame grabber card were provided with a software development kit (SDK) allowing access to all their capabilities through C-style function calls. These function are available to a user written program via 32-bit dynamically linked libraries (DLL).

The development environment was Microsoft Visual C++ 5.0, and the code was written in C++. To provide the user with a natural interface, the program was based on the Microsoft Foundation Classes (MFC) libraries. These libraries provide a simple C++ interface to the file system, the window management, and the graphical capabilities of the Windows operating system.

Because of the size of the program in question, and because most of it is specific to the operating system, we will not reproduce its source code in this document. Its functionality is described in a separate document, and information can be obtained by contacting the CastScan research group.

REFERENCES

1 A.M. Cormack, *J. Appl. Phys.*, 34 (1963), p.2722.

2 G. Hounsfield, *Br. J. Radiol.*, 46(1973), p.1016.

3 J. Radon, "Uber die Bestimmung von Funktionen durch ihre Integralwertelangs gewisser Magnigfaltigkeiten," *Berichte uber die Verhandlungen,* vol. 69, (Leipzig: Saechsische Akademie der Wissenschaften, 1917), p.262.

4 W.H. Barrett and William Swindell: *Radiological Imaging*, vol. 2 (1981), Academic Press, New York, NY, p. 422.

5 I.M. Jureidini, "A Design for a High Energy X-Ray Computed Tomography Sensor for the Study of Solidification Fronts in Aluminum," SM Thesis, Department of Mechanical Engineering, Massachusetts Institute of Technology, Cambridge, MA (1997).

6 J.F. Moore, *Mater. Evaluation*, vol. 48 (1990), p. 630.

7 E.A. Sivers and M.D. Silver: *Mater. Evaluation*, vol. 48 (1990), p. 706.

8 D.C. Copley, J.W. Eberhard, G.A. Mohr, "Computed Tomography Part I: Introduction and Industrial Applications," *Journal of Metals*, January 1994, p.14.

9 D. Oliver et al., *Rev. Prog. Quan. Nondestructive Evaluation*, 5A (1986), p.817.

10 I. Stambler, *Research & Development*, vol. 28 (1986), p. 47.

11 R.T. Bernardi, H. Martz, "Nuclear Waste Drum Characterization with 2 MeV X-Ray and Gamma-Ray Tomography," *Mater. Evaluation,* (October 1995), p.1121.

12 S. Izumi, S. Kamata, K. Satoh, H. Miyai, "High Energy X-ray Computed Tomography for Industrial Applications," *IEEE Transactions on Nuclear Science,* vol. 40, no.2 (April 1993), p.158.

13 D. W. Fitting, W. P. Dube, T. A. Siewert and J. Paran: *Review of Progress in Quantitative Nondestructive Evaluation*, vol. 15 (1996), p. 2315.

14 R. E. Pool and J. N. Koster: *Int. J. Heat Mass Transfer*, vol. 37 (1994), p. 2583.

15 P. A. Curreri and W. F. Kaukler: *Metall. Trans. A*, 1996, vol. 27 (1996), p. 801.

16 W. Kaukler, F. Rosenberger and P. Curreri: *Metall. Trans. A*, vol. 28 (1997), p. 1705.

17 S. Sen, W. F. Kaukler, P. Curreri and D. M. Stefanescu: *Metall. Trans. A*, vol. 28 (1997), p. 2129.

18 V. V. Nagarkar, J. S. Gordon, K. Daley, G. Entine and M. R. Squillante: *Appl. Radiat. Isot.*, vol. 44 (1993), p. 1301.

19 C. F. Chen and F. Chen: *J. Fluid Mech.*, vol. 227(1991), p. 567.

20 J.-H. Chun, R. Lanza, N. Saka, and M. Hytros: *Annals of the CIRP*, vol. 44 (1995), p. 181.

21 M. Hytros, "A Feasibility Study of Solidification Front Monitoring via Tomographic Imaging," SM Thesis, Department of Mechanical Engineering, Massachusetts Institute of Technology, Cambridge, MA (1996).

22 V. Zinov'ev: *Handbook of Thermophysical Properties of Metals at High Temperatures*, Nova Science Publishers, Inc., New York, NY (1996), p. 139.
23 A.V. Oppenheim, A.S. Willsky: *Signals and System,* 2nd edition (1997), Prentice Hall, Upper Saddle River, New Jersey.
24 M Hytros, "Development of a High Energy X-Ray Computed Tomography Sensor for Detecting the Solidification Front Position in Aluminum Casting," PhD Thesis, Department of Mechanical Engineering, Massachusetts Institute of Technology, Cambridge, MA (1998).
25 J.A. Reeds, L.A. Shepp, "Limited Angle Reconstruction in Tomography via Squashing," *IEEE Transactions on Medical Imaging*, vol. MI-6, no. 2 (June 1997), p.89.
26 J. L. Prince, A.S. Willsky, "Constrained Sinogram Restoration for Limited-Angle Tomography," *Optical Engineering*, vol. 29, no. 5 (May 1990), p.535.
27 S.F. Yau, K.K. Yu, "A Sinogram Restoration Technique for the Limited-Angle Problem in Computer Tomography," *Journal of Imaging Science and Technology*, vol. 40, no. 3 (May/June 1996), p. 254.
28 L.C. Ingesson, V.V. Pickalov, "An Iterative Projection-Space Reconstruction Algorithm for Tomography Systems with Irregular Coverage," *J. Phys. D: Appl. Phys.*, vol. 29 (1196), p.3009.
29 T.A. Siewert, M.W. Austin, "The Contributions of Out-of-Plane Material to a Scanned-Beam Laminography Image," *Mater. Evaluation* (October 1994), p.1194.
30 A.R. Kalukin, V. Sankaran, B. Chartrand, D.L. Millard, R.P. Kraft, M.J. Embrechts, "An Improved Method for Inspection of Solder Joints using X-Ray Laminography and X-Ray Microtomography," *Proc. 1996 IEEE/CPMT Int. Electron. Manufact. Technol. Symp.*, p.438.
31 S.M. Rooks, B. Benhabib, K.C. Smith, "Development of an Inspection Process for Ball-Grid-Array Technology using Scanned-Beam X-Ray Laminography," *IEEE Trans. Comp., Packag., Manufact. Technol.*, vol. 18 (December 1995), p. 851.
32 A.R. Kalukin, V. Sankaran, "Three-Dimensional Visualization of Multilayered Assemblies Using X-Ray Laminography," *IEEE Trans. Comp., Packag., Manufact. Technol.*, vol. 20, no. 3 (September 1997), p. 361.
33 U. Ewert, J. Robbel, C. Bellon, A. Schumm, C. Nockemann, "Digital Laminography," *Materialprufung*, vol. 37, no 6 (1995), p. 218.
34 U. Ewert, V. Baranov, K. Borchardt, "Cross-Sectional Imaging og Building Constructions by new Non-Linear Tomosynthesis Techniques Using Imaging Plates and ^{60}Co-Radiation," *International Symposium Non-Destructive Testing in Civil Engineering*, vol. 26 (1995), p. 1267.
35 S.M.Ross, *Introduction to Probability and Statistics for Engineers and Scientists*, John Wiley & Sons, New York, NY (1987).
36 *pcStep 4A User Manual*, nuLogic Inc., Needham, MA, Revision 2.0 (1995).
37 *DT3157 Hardware User Manual*, Data Translation Inc., Marlboro, MA, first edition (July, 1996).